PolyPublie
Polytechnique Montréal

POLYTECHNIQUE MONTRÉAL
UNIVERSITÉ D'INGÉNIERIE

Titre: Title:	Design and Analysis of Slot Based Transparent Magnet-Less Non-Reciprocal Metasurfaces
Auteur: Author:	Burak Gurlek
Date:	2015
Type:	Mémoire ou thèse / Dissertation or Thesis
Référence: Citation:	Gurlek, B. (2015). Design and Analysis of Slot Based Transparent Magnet-Less Non-Reciprocal Metasurfaces [Master's thesis, École Polytechnique de Montréal]. PolyPublie. https://publications.polymtl.ca/1809/

Document en libre accès dans PolyPublie
Open Access document in PolyPublie

URL de PolyPublie: PolyPublie URL:	https://publications.polymtl.ca/1809/
Directeurs de recherche: Advisors:	Christophe Caloz
Programme: Program:	génie électrique

Ce fichier a été téléchargé à partir de PolyPublie, le dépôt institutionnel de Polytechnique Montréal
This file has been downloaded from PolyPublie, the institutional repository of Polytechnique Montréal

https://publications.polymtl.ca

UNIVERSITÉ DE MONTRÉAL

DESIGN AND ANALYSIS OF SLOT BASED TRANSPARENT MAGNET-LESS NON-RECIPROCAL METASURFACES

BURAK GURLEK
DÉPARTEMENT DE GÉNIE ÉLECTRIQUE
ÉCOLE POLYTECHNIQUE DE MONTRÉAL

MÉMOIRE PRÉSENTÉ EN VUE DE L'OBTENTION
DU DIPLÔME DE MAÎTRISE ÈS SCIENCES APPLIQUÉES
(GÉNIE ÉLECTRIQUE)
AOÛT 2015

© Burak Gurlek, 2015.

UNIVERSITÉ DE MONTRÉAL

ÉCOLE POLYTECHNIQUE DE MONTRÉAL

Ce mémoire intitulé :

DESIGN AND ANALYSIS OF SLOT BASED TRANSPARENT MAGNET-LESS NON-RECIPROCAL METASURFACES

présenté par : GURLEK Burak
en vue de l'obtention du diplôme de : Maîtrise ès sciences appliquées
a été dûment accepté par le jury d'examen constitué de :

M. AKYEL Cevdet, D. Sc. A, président
M. CALOZ Christophe, Ph. D., membre et directeur de recherche
M. SIROIS Frédéric, Ph. D., membre

DEDICATION

To my beloved Ayca

ACKNOWLEDGEMENTS

As the conclusion of my M.Sc study, I want to take this chance to sincerely thank many people for their endless support. I'm very grateful to my advisor, Prof. Christophe Caloz, for his generous acceptance of me as a member of his research group, and I want to thank him for his guidance, support and patience during my study. I learnt a lot of valuable lessons beyond just science from the fruitful research environment provided by him. I was very lucky to be a part of one of the strongest research group in electromagnetic theory.

I would also like to thank all my committee members : Prof. Cevdet Akyel and Prof. Frédéric Sirois for their time and efforts in reviewing my thesis and their attendance to my thesis defense. I want to thank Dr. Salem, Dr. Sounas and Dr. Kodera for their support, encouragement and friendship. My gratitude is extended to Mrs. Desparois and Mrs. Pavlov for their administrative work and to Mr. Décarie for his IT support.

I want to thank all my friends : Mohamed Salem, Amar Al-Bassam, Seyyid M. Dilek, Levent Erdogan, Karim Achouri, Hualin Zhan, Babak Nikfal, Nima Chamanara and Yangping Zhao. Thank you for being my friends, I have remembered and I appreciate every single favor that I have received from any of you during this path.

Last but not least, I would like to thank my parents, who gave me the birth and brought me up. They always support me. I would like to express my deepest gratitude to my source of happiness Ayca Onur, for her endless love, encouragement and support.

RÉSUMÉ

Le but de ce travail de recherche est de concevoir et d'analyser des métasurfaces gyrotropiques non-réciproques ne nécessitant pas de champ de polarisation magnétique. Une réponse non-réciproque peut être obtenue en brisant la symétrie par renversement du temps (symétrie T). Ce qui peut être réalisé en utilisant des quantités qui sont antisymétriques par renversement du temps comme le champ magnétique, le courant électrique, le moment et le moment angulaire orbital. Dans ce travail, un courant électrique de polarisation est utilisé pour briser la symétrie T et ainsi obtenir une réponse gyrotropique non-réciproque.

Un réseau périodique en deux dimensions constitué d'ouvertures annulaires terminées par de grandes ouvertures carrées et chargées par des semi-conducteurs unidirectionnels est suggéré pour réaliser une métasurface non-réciproque sans polarisation magnétique (MNM). Il est montré qu'une terminaison avec de larges ouvertures carrées est nécessaire pour assurer une adaptation d'impédance entre les ouvertures annulaires et les composants unidirectionnels. De ce fait, une structure MNM est conçue pour obtenir une résonance à ondes progressives, i.e. un dipôle magnétique tournant se comportant de la même façon qu'une molécule de ferrite magnétisée. Les coefficients de réflexion et de transmission de la structure sont calculés numériquement pour en démontrer la réponse gyrotropique non-réciproque. Par ailleurs, la réponse asymétrique de la structure, pour des ondes planes incidentes de polarisation en x ou en y, est mise en évidence et il est suggéré qu'une rotation de la structure permettrait une réponse symétrique non-réciproque au prix de perdre l'effet gyrotropique non-réciproque similaire aux structures en ferrite.

Une explication physique de l'effet gyrotropique non-réciproque, obtenu en empêchant la propagation dans le sens inverse de l'un des modes-propres de la structure, est fournie en utilisant la théorie de Sturm-Liouville. Afin de comprendre la réponse électromagnétique d'une métasurface, les paramètres bi-anisotropiques de surface sont analytiquement dérivés en fonction des dyades de réflexion et de transmission basées sur les conditions aux limites. Les paramètres bi-anisotropiques de surface de la structure MNM sont extraits des résultats de simulations numériques. La réponse magnétique dipolaire de la structure MNM apparaît de manière évidente à travers ses paramètres d'impédance de surface. Etant donné que les paramètres d'impédance de surface sont bien plus élevés comparés aux autres paramètres bi-anisotropiques de surface, un simple modèle de ligne de transmission est proposé pour modéliser la structure MNM monocouche. Malgré le fait que le comportement non-réciproque similaire à la ferrite peut être atteint avec une structure MNM, celle-ci possède un coefficient de réflexion important dû à sa taille plus petite que la longueur d'onde. Afin de contourner le

problème de réflexion élevée de ce type de structure, des méthodes d'annulation de réflexion sont discutées et une analyse préliminaire est employée. Premièrement, le théorème de dualité est exploité pour annuler la réflexion de la structure MNM étant donné que la structure conçue peut être caractérisée par un moment magnétique dipolaire. Les conditions pour annuler la réflexion, appelées les conditions de Kerker, sont dérivées et montrent qu'un moment électrique dipolaire tournant est requis pour annuler la réflexion de la structure MNM. Etant donné qu'un moment électrique dipolaire tournant n'a jamais été réalisé à ce jour, une seconde méthode basée sur des résonances de Fabry-Pérot a été envisagée. Afin de réaliser une cavité de Fabry-Pérot, deux surfaces monocouches de type MNM sont mises l'une à la suite de l'autre avec un substrat diélectrique d'épaisseur d les séparant. Un modèle de ligne de transmission, qui est basé sur le modèle pour une seule couche MNM, est utilisé pour calculer de manière analytique les dyades de réflexion de la structure MNM à deux couches. L'épaisseur du substrat diélectrique, permettant d'annuler la réflexion, est alors analytiquement obtenue. Deux exemples de systèmes sont proposés. Dans le premier exemple, deux ouvertures annulaires chargées avec un composant unidirectionnel parfaitement adapté en impédance sont utilisés pour concevoir la cavité de Fabry-Pérot. Il est démontré que l'épaisseur du diélectrique requise pour annuler la réflexion est imaginaire à cause des pertes inhérentes de la structure. Il est également montré que les pertes de la structure sont causées par le fait que l'on empêche la propagation en sens inverse d'un des modes-propres rendant ainsi impossible une parfaite annulation de la réflexion en utilisant le principe de cavité de Fabry-Pérot. Les coefficients de réflexion et de transmission de la structure MNM à deux couches sont calculés de manière semi-analytique en utilisant le modèle décrit ci-dessus ainsi que les paramètres d'impédance de surface obtenus par simulation. Il est déterminé que cette structure MNM à deux couches possède également une réflexion non négligeable. De ce fait, un compromis existe entre les pertes inhérentes de la structure monocouche et son coefficient de transmission. Dans le second exemple, deux ouvertures annulaires chargées avec un composant unidirectionnel qui n'est pas adapté en impédance sont utilisés pour concevoir la cavité de Fabry-Pérot. Etant donné que les pertes de la structure sont réduites du fait de la différence d'impédance, le coefficient de transmission de la structure est nettement amélioré et une importante réponse gyrotropique est obtenue. Cependant, à cause de la non-minimisation du coefficient de réflexion, la résonance à ondes progressives est détériorée menant à un plus faible facteur de non-réciprocité.

Etant donné que la réponse non-réciproque de la structure MNM à deux couches est faible, une méthode est introduite pour contrôler l'effet gyrotropique et la non-réciprocité de cette structure. Il est montré que la réponse non-réciproque et gyrotropique de la structure MNM mono couche peut être contrôlée en ajoutant un délai de phase au composant unidirection-

nel ainsi qu'en effectuant une rotation de la cellule unitaire. La méthode proposée est basée sur une technique d'optimisation de contraintes non-linéaires dont la fonction de coût est minimisée selon les dyades de réflexion et de transmission désirées de la structure MNM à deux couches. Ainsi, les dyades d'impédance de la surface mono couche qui minimisent la fonction de coût peuvent être déterminées. Finalement, la structure MNM mono couche est synthétisée grâce au délai de phase du composant unidirectionnel et de l'angle de rotation de la cellule unitaire. Un exemple de conception est proposé comme preuve de concept et consistant en une métasurface transformant une onde plane polarisée en y et normalement incidente en une onde plane polarisée en x tout en reflétant toutes les autres et présentant un important facteur de non-réciprocité. A cause de la largeur de bande limitée de cette structure, une vérification expérimentale n'a pas pu être menée.

ABSTRACT

The goal of this research is to design and analysis of transparent magnet-less non-reciprocal gyrotropic metasurfaces (MNMs). Non-reciprocal response requires breaking of the time-reversal symmetry and could be realized with quantities that are odd vector under time reversal such as magnetic field, current, momentum and orbital angular momentum. Current biasing is used to break the time-reversal symmetry and to achieve transparent non-reciprocal gyrotropic response.

A 2D periodic array of annular slotted ring structure terminated with big slot patches and loaded with semiconductor-based unidirectional components is suggested to realize a transparent magnet-less non-reciprocal gyrotropy. It is shown that the big slot termination is required for matching of the annular slotted transmission line and the unidirectional component. Thus, a slot MNM is designed to achieve a travelling wave resonance, i.e. the rotating magnetic dipole response as magnetized ferrite molecules. Reflection and transmission coefficients of the designed structure are numerically computed to prove the ferrite-like non-reciprocal gyrotropic response of the structure. Moreover, asymmetrical response of the structure under x- and y-polarized plane wave incidence is highlighted and a rotated design is suggested to have a symmetrical non-reciprocal response in the expense of destroying the ferrite-like non-reciprocal gyrotropy.

A physical explanation of the non-reciprocal gyrotropy, achieved by prohibiting one of the counter-propagating eigenstates of the slot MNM, is provided by utilizing the Sturm-Liouville theory. In order to understand the electromagnetic response of a metasurface, bianisotropic surface parameters of the metasurface is analytically derived in terms of reflection and transmission dyadics from discontinuity of the electromagnetic fields. Bianisotropic surface parameters of the slot MNM is extracted from the numerical simulation results. Magnetic dipole moment response of the slot MNM is evident from its large surface impedance parameters. Since surface impedance parameters of the structure is very large compared to other bianisotropic surface parameters, a simple transmission-line model is suggested to model the single-layer slot MNMs. Although ferrite-like transparent non-reciprocal behaviour could be achieved with slot MNMs, there is a non-negligible reflection from the structure due to its subwavelength nature.

In order to circumvent the reflection issue of slot MNMs, reflection cancellation methods are discussed and a tentative analysis is employed. First, the duality theorem is exploited to cancel the reflection of slot MNMs since the designed structure could be characterized with a magnetic dipole moment. The reflection cancellation conditions, namely Kerker con-

ditions, are derived where a rotating electric dipole moment response is required to cancel the reflection of slot MNMs. Since the rotating electric dipole moment response has not been realized so far, the second method based on Farby-Pérot resonances is introduced. In order to form a Farby-Pérot cavity, two single-layer slot MNMs are cascaded with a dielectric spacer with thickness d. The network model for the double layer slot MNMs based on transmission-line model of the single-layer slot MNM is used to analytically calculate the reflection dyadic of the double layer structure. The thickness of the dielectric spacer which makes the reflection dyadic zero is analytically derived. Two design examples are provided. In the first example, two annular slotted rings loaded with perfectly matched unidirectional components are utilized to design Farby-Pérot cavity. It is shown that the dielectric spacer thickness required to cancel the reflection dyadic is imaginary due to the inherent loss of the structure. It is shown that inherent loss of the structure is caused by prohibiting one of the counter-propagating eigenstates so that the perfect reflection cancellation cannot be achieved with Farby-Pérot cavities. Reflection and transmission coefficients of the double layer slot MNMs are semi-analytically calculated by using the introduced network model and the extracted surface impedance parameters. It is shown that the double layer structure has non-negligible reflections. Thus, the trade-off between inherent loss of the single-layer slot MNM and its transparency is highlighted. Thus, a new design based on low level of inherent loss is suggested to increase the transparency. In the second design, two annular slotted rings loaded with imperfectly matched unidirectional components are utilized to design the Farby-Pérot cavity. Since the inherent loss of the structure is degraded with the imperfect matching, the transparency of the double layer slot MNM is greatly increased and strong gyrotropic response is achieved. However in the expense of reflection minimization, the travelling wave resonance is destroyed so that the non-reciprocal response is reduced.

Since non-reciprocal response of the highly transparent double layer slot MNMs are weak, a method is introduced to control the gyrotropy and non-reciprocity with the double layer slot MNMs. It is shown that non-reciprocal and gyrotropic response of the single-layer slot MNMs can be controlled with phase shift of the unidirectional component and rotation angle of the unit-cell. The proposed method is based on a non-linear constraint optimization technique where the cost function is minimized according to the desired reflection and transmission dyadics of the double layer slot MNM. The required single-layer surface impedance dyadics that minimizes the cost function are found. Lastly, the single-layer slot MNMs are synthesized based on phase shift of the unidirectional component and the rotation angle of the unit-cell. A design example is provided as a proof-of-concept where the designed metasurface transform y-polarized normally incident propagating plane waves into x-polarized ones while reflecting the others and has a huge non-reciprocal response.

TABLE OF CONTENTS

DEDICATION iii

ACKNOWLEDGEMENTS iv

RÉSUMÉ v

ABSTRACT viii

TABLE OF CONTENTS x

LIST OF TABLES xii

LIST OF FIGURES xiii

LIST OF SYMBOLS AND ABBREVIATIONS xix

LIST OF APPENDIXES xxii

CHAPTER 1 INTRODUCTION 1
1.1 Definitions and Basic Concepts 1
1.2 Research Objectives 4
1.3 Thesis Plan 5

CHAPTER 2 GYROTROPY, NON-RECIPROCITY AND MNM TECHNOLOGY 6
2.1 Gyrotropy and Non-Reciprocity 6
2.1.1 Microscopic and Macroscopic Properties of Ferrimagnetic Materials . 7
2.2 MNMs Technology 11
2.2.1 MNMs Based on Current Biasing 13

CHAPTER 3 SINGLE-LAYER SLOT TYPE TRANSPARENT MNMs 15
3.1 Transparent MNMs Design 15
3.2 Physical Explanation of the Non-Reciprocity of Transparent Slot MNMs . . 33
3.3 Characterization of The Transparent Slot MNMs 36
3.3.1 Full Surface Parameter Extraction of the Slot MNM 36
3.3.2 Basic Transmission-Line Model for Transparent Slot MNMs 41

CHAPTER 4 MULTI-LAYER SLOT MNMs STRUCTURE FOR MINIMAL REFLECTION 44
4.1 Reflection Minimization for Non-reciprocal Gyrotropic materials 44
4.2 Reflection Cancellation Methods 45
4.2.1 Exploiting the Duality Theorem 45
4.2.2 Exploiting Farby-Pérot Resonances 47
4.3 Network Model for double-layer Slot MNM Structures 48
4.4 Design Example : Highly Transparent Non-reciprocity via double-layer Slot MNM 51
4.5 Controlling Gyrotropy and Non-reciprocity by using Multi-layer Slot MNMs 64
4.5.1 Design Example : Controlling the Gyrotropy and Non-reciprocity by Using double-layer Slot MNM Structures 68

CHAPTER 5 CONCLUSION 72

REFERENCES 75

APPENDICES 80

LIST OF TABLES

Table 3.1 Design parameters of the slot MNM resonating at 5.3 GHz. 20
Table 4.1 Design parameters of the slot MNM resonating at 8.4 GHz. 57

LIST OF FIGURES

Figure 1.1 (a) Illustration of atomic structure of a natural material. (b) Illustration of a metamaterial with its subwavelength artificial atoms [1]. . . 2

Figure 2.1 Electromagnetic response of a gyrotropic media [2]. 6

Figure 2.2 (a) Illustration of a reciprocal gyrotropy. (b) Illustration of a non-reciprocal gyrotropy (time-reversal case) [2]. 8

Figure 2.3 Illustration of a spinning electron around the direction of biasing static magnetic field [3]. 9

Figure 2.4 (a) Illustration of interaction of the RCP plane wave with a magnetized ferrite electron biased with $+\mathbf{e_z}$ directed biasing magnetic field. (b) Illustration of interaction of the LCP plane wave with magnetized ferrite electron biased with $+\mathbf{e_z}$ directed biasing magnetic field [3]. . . 10

Figure 2.5 (a) Band structure of spatiotemporally modulated silicon waveguide [4]. (b) Illustration of I-MNMs based on current biasing and electron spin of magnetized ferrites [5]. (c) Illustration of L-MNMs based on azimuthal spatiotemporal modulation of the refraction index along conductive ring pair structure and its counter-propagating eigenstates [6]. 12

Figure 2.6 (a) Illustration of even mode operation of the microstrip I-MNM. (b) Illustration of odd mode operation of the microstrip I-MNM. (c) Illustration of the induced magnetic dipole moment by odd mode of the microstrip I-MNM [7]. (d) Fabricated microstrip I-MNM, top and bottom of the substrate [8]. 13

Figure 3.1 (a) Slot MNM design based on the Babinet principle. (b) The transmission line model of the designed Slot MNM with electrical length $\beta\ell$. 16

Figure 3.2 (a) Modified slot MNM design based on the Babinet principle. (b) Annular slotted ring structure with its design parameters. (c) Transmission line model of the modified slot MNM. 17

Figure 3.3 (a) Characteristic impedance of a slot transmission line for different slot widths. (b) Effective permittivity of a slot transmission line for different slot widths. Thickness of the substrate is 0.8 mm, relative permittivity of the substrate is 2.6. 17

Figure 3.4 (a) Transverse current and field distribution of the modified annular slotted ring structure. (b) Cross section view of magnetic field distribution of the modified annular slotted ring structure. 19

Figure 3.5 Transverse current and field distribution of the designed slot MNM at different time instances. (a) $t = t_0$. (b) $t = t_0 + T/4$. (c) $t = t_0 + T/2$. (d) $t = t_0 + 3T/4$ where T is period of the incident plane wave. . 20

Figure 3.6 S-parameters of the ports A and B, shown in Fig. 3.2(c). (a) Magnitude of S_{11} and S_{21} computed by ADS. (b) Phase of S_{21} computed by ADS. (c) Magnitude of S_{11} and S_{21} computed by HFSS (d) Phase of S_{21} computed by HFSS. 22

Figure 3.7 Reflection and transmission coefficients of the designed slot MNM based on the parameters given in Table 3.1 under plane wave illumination from $z > 0$.(a) x-polarized plane wave incidence. (b) y-polarized plane wave incidence. The comparison of reflection and transmission coefficients of the unidirectional component loaded (w superscript) and the unloaded structure (wo superscript) under plane wave illumination. (c) x-polarized plane wave incidence. (d) y-polarized plane wave incidence. 24

Figure 3.8 Non-reciprocity of the designed slot MNM : Comparison of the transmission coefficients when the structure is excited from $z > 0$ and $z < 0$ in time-reversal schema. (a) Magnitude. (b) Phase. 25

Figure 3.9 Time evaluation of the transverse electric current along unit-cell of the slot MNM computed by using HFSS and Ansoft Designer. (a) $t = t_0$. (b) $t = t_0 + T/8$. (c) $t = t_0 + T/4$. (d) $t = t_0 + 3T/8$. 26

Figure 3.10 Time evaluation of the magnetic fields transverse to $\mathbf{e_z}$ direction along unit-cell of the slot MNM computed by using HFSS and Ansoft Designer. (a) $t = t_0$. (b) $t = t_0 + T/8$. (c) $t = t_0 + T/4$. (d) $t = t_0 + 3T/8$. . 27

Figure 3.11 (a) Ellipticity of the designed slot MNM. (b) Faraday rotation angle of the designed slot MNM. 29

Figure 3.12 (a) Transmission coefficients of the slot MNM under the RCP and the LCP plane wave illumination from $z > 0$. (b) An ideal symmetric slot MNM. 29

Figure 3.13 (a) Reflection and transmission coefficients of the 45° rotated slot MNM under x-polarized plane wave illumination from $z > 0$. (b) Comparison of reflection and transmission coefficients of the unidirectional component loaded (w superscript) and the unloaded structure (wo superscript) under plane wave illumination. Non-reciprocity of the 45° rotated slot MNM : Comparison of the transmission coefficients when the structure is excited from $z > 0$ and $z < 0$ in time-reversal schema. (c) Magnitude. (d) Phase. 31

Figure 3.14 (a) Ellipticity of the 45° rotated slot MNM. (b) Faraday rotation angle of the 45° slot MNM. 32

Figure 3.15 (a) Counter-propagating eigenstates of the unloaded slot MNM. (b) Transverse current distribution over PEC plane of the slot MNM with the observation vector $\mathbf{r}$. 33

Figure 3.16 Surface parameters of the slot MNM resonant at 5.3 GHz. (a) Real part of the surface admittance. (b) Imaginary part of the surface admittance. (c) Real part of the electro-magnetic surface parameter. (d) Imaginary part of the electro-magnetic surface parameter. (e) Real part of the magneto-electric surface parameters. (f) Imaginary part of the magneto-electric surface parameters. (g) Real part of the surface impedance. (h) Imaginary part of the surface impedance. 40

Figure 3.17 Network model for a Slot MNM. 42

Figure 3.18 Extracted surface impedance parameters of the slot MNM resonant at 5.3 GHz (a) Real part. (b) Imaginary part. Extracted surface impedance parameters of the 45° rotated slot MNM (c) Real part. (d) Imaginary part. 43

Figure 4.1 (a) Right-handed circularly rotating magnetic dipole moment model for slot MNMs. (b) Dual particle of a slot MNM, left-handed circularly rotating electric dipole moment, for the reflection cancellation. 46

Figure 4.2 Schematic representation of the reflection from a multi-layered surface consisting of anisotropic single-layers. 48

Figure 4.3 Double-layer slot MNM unit cell with a dielectric slab spacer whose permittivity ε_d and thickness d. The double-layer slot MNMs are made up from (a) Non-rotated single-layer slot MNMs. (b) 45° rotated single-layer slot MNMs. 49

Figure 4.4 Comparison of the transmission coefficient T_{yx} obtained from numerical and analytical methods for different dielectric slab spacer thicknesses. (a) Amplitude (b) Phase. Reflection and transmission coefficients of the double-layer slot MNM for $d = 12\,\text{mm}$. (c) x-polarized plane wave incidence. (d)y-polarized plane wave incidence. Solid lines represents the simulation results obtained from HFSS, dashed lines refer to the results obtained from the analytical network model result (4.7). The single-layer slot MNM designed with parameters given in Table 3.1 and $\varphi_{is} = 127°$. 52

Figure 4.5 Zeros and poles of reflection coefficients of the double-layer slot MNM calculated from (4.9) for each co- and cross-polarized terms at 5.33 GHz. The double-layer slot MNM obtained from : (a) Non-rotated single-layer slot MNMs as in Fig. 4.3(a). (b) 45° counterclockwise rotated single-layer slot MNMs as in Fig. 4.3(b). Circles represents the zeros and crosses refers to the poles of (4.9). Insets shows the zoomed version of the plots around $Re\{d\} = 27\,\text{mm}$. 53

Figure 4.6 Reflection and transmission coefficients of the double-layered slot MNMs. Results obtained from : (a) The analytical solution (4.10) when $d = 0.027130\,\text{mm}$. (b) The optimization method when $d = 0.049430\,\text{mm}$. Non-reciprocity of the designed double-layer slot MNM : Comparison of the transmission coefficients when it is excited from $z > 0$ and $z < 0$ in time-reversal schema. (c) Magnitude. (d) Phase. (e) Total scattered powers of the single-layer slot MNM under normally propagating RCP and LCP plane waves incidence where $P_{RCP} = |R_{++}|^2 + |R_{-+}|^2 + |T_{++}|^2 + |T_{-+}|^2$ and $P_{LCP} = |R_{--}|^2 + |R_{+-}|^2 + |T_{--}|^2 + |T_{+-}|^2$. . . . 55

Figure 4.7 (a) S-parameters of the ports A and B, shown in Fig. 3.2(c). (a) Magnitude of S_{11} and S_{21} computed by HFSS. (d) Phase of S_{21} computed by HFSS. 58

Figure 4.8 Reflection and transmission coefficients of the designed single-layer slot MNM based on parameters given in Table 4.1 under plane wave illumination from $z > 0$.(a) x-polarized plane wave incidence. (b) y-polarized plane wave incidence. Non-reciprocity of the designed single-layer slot MNM : Comparison of the transmission coefficients when it is excited from $z > 0$ and $z < 0$ in time-reversal schema. (c) Magnitude. (d) Phase. 59

Figure 4.9 (a) Reflection and transmission coefficients of the 45° rotated single-layer slot MNM under x-polarized plane wave illumination from $z > 0$. (b) Transmission coefficients of the 45° rotated single-layer slot MNM under RCP and LCP plane wave illumination from $z > 0$. Non-reciprocity of the 45° rotated single-layer slot MNM : Comparison of the transmission coefficients when it is excited from $z > 0$ and $z < 0$ in time-reversal schema. (c) Magnitude. (d) Phase. (e) Total scattered powers of 45° rotated single-layer slot MNM under normally propagating RCP and LCP plane wave incidence where $P_{RCP} = |R_{++}|^2 + |R_{-+}|^2 + |T_{++}|^2 + |T_{-+}|^2$ and $P_{LCP} = |R_{--}|^2 + |R_{+-}|^2 + |T_{--}|^2 + |T_{+-}|^2$. . . . 60

Figure 4.10 Reflection and transmission coefficients of the double-layered slot MNM made up from unmatched single-layer slot MNMs when $d = 36.66$ mm. (a) The reflection coefficients. (b) The transmission coefficients. Non-reciprocity of the double-layer slot MNM : Comparison of the transmission coefficients when it is excited from $z > 0$ and $z < 0$ in time-reversal schema.(c) Magnitude.(d) Phase. 61

Figure 4.11 (a) Ellipticity of the double-layer slot MNM. (b) Faraday rotation angle of the double-layer slot MNM. 63

Figure 4.12 Rotation of a slot MNM around z axis 64

Figure 4.13 Surface impedance parameters of the imperfectly matched slot MNM for different phase shifts φ_{is} and rotation angles θ. (a) Real part of Z_{xx}. (b) Imaginary part of Z_{xx}. (c) Real part of Z_{xy}. (d) Imaginary part of Z_{xy}. (e) Real part of Z_{yx}. (f) Imaginary part of Z_{yx}. (g) Real part of Z_{yy}. (h) Imaginary part of Z_{yy}. 66

Figure 4.14 Double-layer slot MNM design formed by using different single-layer slot MNMs with rotation angles θ_1, θ_2 and phase shifts $\varphi_{is}^{(1)}$, $\varphi_{is}^{(2)}$ in order to control gyrotropy and non-reciprocity. 67

Figure 4.15 (a) Reflection and transmission coefficients of the designed double-layer slot MNM under plane wave incidence from $z > 0$: (a) x-polarized plane wave incidence. (b) y-polarized plane wave incidence. Non-reciprocity of the double-layer slot MNM : Comparison of the transmission coefficients when it is excited from $z > 0$ and $z < 0$ in time-reversal schema. (c) Magnitude. (d) Phase. 69

Figure A.1 Circuit representation of the slot MNM where full-wave solution of the annular slotted ring structure is loaded with an unidirectional component through S-parameters. **a** and **b** are incident and reflected power waves from the structure under TM^z and TE^z illuminations. $[\mathbf{S}]_{6\times6}$ is the S matrix of the annular slotted ring and $[\mathbf{S^{is}}]_{2\times2}$ S matrix of the isolator. 80

Figure B.1 (a) Slot MNM design with FET connection points.(b) Common-source FET implementation as an unidirectional component of a slot MNM. (c) Fabricated structure by Toshiro et al. [9] 82

LIST OF SYMBOLS AND ABBREVIATIONS

Abbreviations

MNM	Magnet-less Non-reciprocal Metasurface
I-MNM	MNM achieved with current biasing
L-MNM	MNM achieved with orbital angular momentum modulation
RCP	Right-handed Circularly Polarization
LCP	Left-handed Circularly Polarization
MMIC	Monolithic Microwave Integrated Circuit
PEC	Perfect Electric Conductor
PEMC	Perfectly Electromagnetic Conductor
FET	Field Effect Transistor
TE	Transverse Electric
TM	Transverse Magnetic
HFSS	High Frequency Structural Simulator
ADS	Advanced Design System

Symbols

c	Speed of light
f	Frequency
p	Periodicity
λ	Wavelength
λ_g	Guided Wavelength
t	Time
ε	Permittivity
ε_r	Permittivity of the substrate
ε_{eff}	Effective permittivity of the substrate
μ	Permeability
n_+	Refraction index under RCP plane wave incidence
n_-	Refraction index under LCP plane wave incidence
Z	Characteristic impedance of transmission-line
β	Propagation constant
ℓ	Electrical length
R	Radius of the annular slotted ring
h	Thickness of the substrate
H	Width of the big slot patch
L	Length of the big slot patch
W	Thickness of the slot line
ψ	Opening angle of the annular slotted ring
φ_{is}	Phase shift of the unidirectional component
δ	Ellipticity
θ_F	Faraday rotation angle
I	Current
V	Voltage
ω	Angular frequency
d	Thickness of the dielectric slab spacer
k_d	Wavenumber inside the dielectric slab spacer
k_0	Wavenumber inside air
θ	Rotation angle of the single-layer slot MNM unit-cell
$\mathcal{M}$	Time-varying magnetic dipole moment
$\mathbf{E}$	Electric field vector
$\mathbf{H}$	Magnetic field vector

$\mathbf{B}$	Magnetic flux density
$\mathbf{J}$	Current density vector
$\mathbf{e_x}$	x directed unit vector
$\mathbf{e_y}$	y directed unit vector
$\mathbf{e_z}$	z directed unit vector
$\mathbf{e}_\rho$	ρ directed unit vector
$\mathbf{m}$	Magnetic dipole moment vector
$\mathbf{p}$	Electric dipole moment vector
$\mathbf{r}$	Observation vector
$\mathbf{n}$	Unit vector in the direction of observation point $\mathbf{r}$
$\bar{\bar{I}}$	Unit dyadic
$\bar{\bar{R}}$	Reflection dyadic
$\bar{\bar{T}}$	Transmission dyadic
$\bar{\bar{\chi}}$	Susceptibility tensor
$\bar{\bar{\mu}}$	Permeability tensor
$\bar{\bar{\zeta}}$	Electric-magnetic coupling tensor
$\bar{\bar{\xi}}$	Magnetic-electric coupling tensor
$\bar{\bar{Z}}_s$	Surface impedance tensor
$\bar{\bar{Y}}_s$	Surface admittance tensor
$\bar{\bar{\Psi}}_s$	Magneto-electric coupling tensor
$\bar{\bar{\Theta}}_s$	Electro-magnetic coupling tensor
$\bar{\bar{\eta}}$	Characteristic impedance of a medium
$\bar{\bar{R}}(\theta)$	Rotation dyadic

LIST OF APPENDIXES

Appendix A CALCULATION OF ELECTROMAGNETIC RESPONSE OF A UNIDIRECTIONAL COMPONENT LOADED ANNULAR SLOTTED RING BASED ON SIGNAL FLOW GRAPH TECHNIQUE 80

Appendix B IMPLEMENTATION OF A COMMON-SOURCE FET AS A UNIDIRECTIONAL COMPONENT IN SLOT MNM DESIGN 82

Appendix C REFLECTION DYADIC OF THE DOUBLE-LAYER SLOT MNMs . 84

CHAPTER 1 INTRODUCTION

1.1 Definitions and Basic Concepts

From beginning of the mankind, humans have tried to mimic, replicate or synthesize the properties of nature which provides consistent resources for living beings. The need for certain materials drive human's motivation to replicate or synthesize them. These incentives led humans to initiate research on chemistry which can be traced to the ancient practice known as alchemy, the art of synthesizing noble metals from base metals. Therefore, there is always a need for a material so that it preserves certain properties that are found in its natural state but being lighter, thinner or vice-versa.

One of the most important and complicated property that nature poses is periodicity. Periodicity is inherent to many structures that can be found in the nature such as crystals and plays very critical role in the ecosystem. For example, butterfly wings have beautiful colors and patterns provided by periodic arrangement of the molecules on their wing. These periodic arrangements create filtering effect in spatial and frequency domain so that the amazing pattern and colors are diffracted from the butterfly wings which actually protect them from predators. In addition, as recently discovered by Teyssier et al. [10], chameleons can change their skin colors rapidly by active tuning of a lattice of guanine nanocyrstals within their skin layers. However scientists could not start to exploit this property of the nature until the discovery of quantum nature of atoms by Niels Bohr. With the establishment of the quantum theory of light and matter, scientists was able to understand why materials respond to external stimulations such as electromagnetic force in a certain way. This was the knowledge and motivation that led Sir Jagadish Bose to invent first known *Artificial Material*, Bose's polarizers, by exploiting the periodicity. He designed polarizers and polarization rotators for his microwave radio receiver by creating planar and twisted tinfoil gratings. In order to design such an artificial media, he used twisting tinfoil fibers [11] so that he mimicked a sugar molecule, which rotates the polarization of electromagnetic wave due to its chiral structure. Following Bose's first attempt to mimic natural materials, in 1948, Winston Kock suggested a metal-lens antenna design, consist of parallel-wires and wire meshes, as an artificial dielectric media in order to replace bulky and heavy lenses made by actual dielectric materials [12]. In addition, Kock for the first time characterized the artificial media by its equivalent refraction index and did analytical studies on homogenization of artificial dielectrics [13]. Kock's idea of replacing natural materials with lightweight and non-bulky artificial ones inspired a lot of scientists such as Walter Rotman, who designed a grid of three-dimensional wires to mimic

plasmas with dielectric constants less than one. Thus, Rotman expanded the idea of artificial dielectrics to the artificial materials.

Until 2000, although the area of artificial dielectrics witnessed a lot of progress in theoretical and experimental research [13], the artificial dielectrics could not be used for industrial applications. However, in 2000, Smith et al. [14] proposed experimental design, a composite medium that poses a negative refraction index by inspiring from the theoretical work done by Victor Veselago [15] where he did research on electrodynamics of a media with a negative refraction index. In addition, Smith et al. experimentally realized the media with negative refraction index by combining a negative permittivity media with a negative permeability media. The resulting media provides *Left-handed* propagation of electromagnetic waves where the direction of the phase progression and energy propagation are out-of phase (backward wave propagation). The results of this research ignited a lot of new ideas related to artificial media and later this breakthrough created an emerging research field called *Electromagnetic Metamaterials*.

In their designs, Smith et al. used periodic arrangement of thin wires in order to realize artificial negative permittivity at low frequencies. This structure is first suggested by Sir John Pendry [16] based on the work of Rotman. In addition, that kind of media is also available in nature such as ferroelectric. However the media with a negative permeability cannot be found in nature due to the large plasma frequencies of magnetic materials. In 1999, Pendry et al.[17] came up with an idea of decreasing the plasma frequency of magnetic response based on periodic arrangement of conductive split-ring resonators. Smith et al. utilized this split-ring resonators to achieve negative permeability and in sum, they realized the negative refraction index media.

Electromagnetic metamaterials constitutes a lot of resonant or non-resonant scatters in

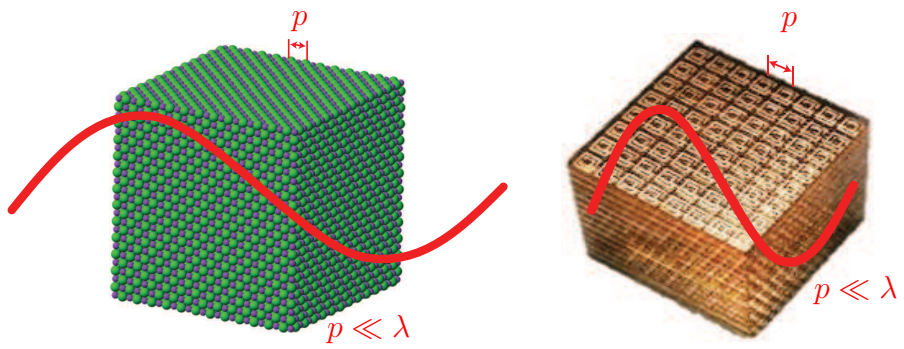

(a) (b)

Figure 1.1 (a) Illustration of atomic structure of a natural material. (b) Illustration of a metamaterial with its subwavelength artificial atoms [1].

a volume or over a surface in periodic arrangement with a period much smaller than guided wavelength, λ_g, so the scatters mimic the behaviours of atoms in natural materials as can be summarized in Fig. 1.1. Metamaterials can be designed to have some electromagnetic properties such as negative index of refraction or near zero-index that is impossible to obtain with natural materials and these properties can be controlled for specific application by varying the periodicity, the size or shape of the scatters as opposed to natural materials. Therefore, electromagnetic metamaterials provides great flexibility to design unprecedented materials and to design light-weight, non-bulky replacement for natural materials.

The first phase of metamaterials research focused on homogenization [18, 19], different realization methods [20], realization of artificial materials with a negative refraction index in optical frequencies [21] and theoretical analysis of wave propagation in left-handed a media [22]. These also led to a lot of practical ideas for industrial applications and to many revolutionary concepts such as full space scan leaky wave antennas [23, 20], cloaking by using plasmonic shells [24], shaping the light propagation and cloaking with transformation optics [25], creating anisotropic and chiral metamaterials [26, 27], and superlenses [28]. However it was seen by many scientists that volumetric metamaterials were not practical and difficult to realize since the electromagnetic response of a metamaterial is originating from its resonant unit-cell particles so that they are lossy, dispersive and have very narrow bandwidth [20].

In order to overcome the issue regarding the loss, many scientist suggested two-dimensional metamaterials, called *Metasurfaces*, which constitute the $2D$ periodic arrangement of scatters and has sub-wavelength thickness [29, 30]. Although metasurfaces can be characterized with their refraction index, it cannot be uniquely determined since its electromagnetic thickness is ambiguous [31]. Therefore, in the second phase of metamaterial research, the focus is shifted to the functionality of the 2D dimensional device from mimicking the exact electromagnetic properties of certain materials. This phase of metamaterial research is still evolving and resulted in many exciting and practical ideas such as wave-front engineering [32], ultra-thin broadband polarizers [33], solar spectrum management [34], achieving large non-linear responses [35] and realizing bi-anisotropic responses [36].

One of the most important and practical research achievement done in the second phase of the metamaterial research, also the main topic of this thesis, is realization of the magnet-less non-reciprocal gyrotropic response which is naturally provided by magnetized ferrites or magneto-optical materials. Although the artificial magnet-less non-reciprocal response was realized for the first time by Yu et al.[37] by breaking the time reversal symmetry with spatial-temporal refractive index modulation, this design does not provides a non-reciprocal gyrotropic response, i.e. magnet-less artificial Faraday rotation. Toshiro et. al [8] for the first time designed a magnet-less non-reciprocal gyrotropic metasurface which consists of a

conductive ring loaded with a semiconductor-based unidirectional component. The designed unit-cell mimics spinning of the ferrite electrons under static magnetic biasing field to provide magnet-less artificial Faraday rotation. This novel concept has led to many practical applications such as integrable and lightweight magnet-less isolators and circulators [38]. Later, Sounas et. al [6] suggested a magnet-less non-reciprocal metamaterial by breaking the time reversal symmetry with azimuthal spatiotemporal permittivity modulation. Although the metamaterial unit-cell theoretically can be used to form a magnet-less non-reciprocal gyrotropic metasurface, the structure is not feasible for real life applications. However, this design is successfully utilized to design isolators and circulators for optical and acoustics applications [39, 40, 41]. Therefore, the concept of magnet-less gyrotropic non-reciprocity is wide and open to new applications.

1.2 Research Objectives

The first magnet-less non-reciprocal gyrotropic metasurface is suggested based on the periodic arrangements of microstrip circular ring structure loaded with semiconductor-based unidirectional components [8]. Realization of the unidirectional component has been done by employing a common-source Field Effect Transistor (FET). Although, in theory the Magnet-less Non-reciprocal Metasurface (MNMs) can be designed by employing a unit-cell of horizontally stacked two conductive ring differentially loaded with a common-source FET, in practice the need for a biasing network of FET necessitate the use of a ground plane. Thus, only one conductive ring loaded with a common-source FET and a ground plane at the bottom of the substrate can be realized[5]. Therefore, the design suggested in [8] cannot allow the propagation of the electromagnetic waves, i.e. restricted to the non-reciprocal gyrotropic response in reflection.

The objective of the research is to design transparent magnet-less non-reciprocal gyrotropic metasurfaces in order to realize cheap, non-bulky and integrable non-reciprocal components for microwave applications. Electromagnetic properties of the designed transparent MNMs such as current distribution, reflection, transmission properties is investigated in order to understand the underlying physics of the structure. Due to subwavelength thickness of the structure, non-negligible reflectance, not wanted for real life applications, appears. After designing and analyzing a single-layer transparent MNMs, a new design based on multi-layer MNMs is proposed in order to achieve highly transparent non-reciprocal gyrotropic response. Lastly, the non-reciprocal gyrotropic response of single-layer MNMs structure is utilized to control the gyrotropy and non-reciprocity of multi-layer MNMs.

1.3 Thesis Plan

The thesis is divided into four main parts, chapter 2, 3 and 4. In chapter 2, The physics of gyrotropy and non-reciprocity is discussed and its applications in microwave and optics applications is provided. Next, non-reciprocal gyrotropic response of magnetized ferrimagnetic materials is investigated and the physical picture is presented. This chapter continues with the discussion on how the artificial non-reciprocity can be realized. Then, this chapter finalizes with the discussion on current biased MNMs, its applications and its drawbacks.

In chapter 3, a single-layer transparent MNM design based on slot line structure is provided. The details of the design procedure is discussed and its characterization based on surface parameters such as electric and magnetic susceptibility is done. The non-reciprocal gyrotropic response of the structure is shown from the simulation results and its underlying physics is explained. This chapter finalizes with the transmission line model for transparent MNMs.

In chapter 4, the issue of non-negligible reflection from a transparent slot MNMs is discussed and the reflection cancellation methods for transparent slot MNM is presented. Later, the multi-layer MNM design is employed to minimize reflection of the transparent slot MNMs, and theoretical modeling of the multi-layer structure based on transfer matrix method is introduced. However due to inherent loss of the structure, it is shown that perfect non-reciprocal gyrotropic response cannot be achieved with the multi-layer slot MNMs. It is shown that by sacrificing from the non-reciprocal response of the structure, it is possible to realize a multi-layered MNMs which minimize reflections. Lastly, a discussion on the trade off between non-reciprocity and transparency of multi-layered MNMs is provided. In order to better exploit this issue, a new design method based on parameter manipulation of single-layer transparent slot MNMs is proposed. It is shown that by engineering the phase shift of the unidirectional component and rotation of the unit-cell of single-layer transparent slot MNMs, it is possible to control the gyrotropic and non-reciprocal response of the structure.

CHAPTER 2 GYROTROPY, NON-RECIPROCITY AND MNM TECHNOLOGY

The main goal of this chapter is to give a fundamental background regarding gyrotropy and non-reciprocity and a brief history of artificial non-reciprocal gyrotropic materials. The first section focuses on the definition of gyrotropic and non-reciprocal responses and their industrial applications. Then in the second section, the electromagnetic properties of gyrotropic and non-reciprocal media is introduced in details. In the next section, the drawbacks of using gyrotropic and non-reciprocal natural media is discussed and how to physically realize magnet-less non-reciprocity is introduced. The final section focuses on the I-MNMs, based on breaking time-reversal symmetry with current biasing.

2.1 Gyrotropy and Non-Reciprocity

The word gyrotropy comes from the Greek word *gyro* meaning round so that the polarization plane of the electromagnetic wave rotates as it propagates. Specifically, any electromagnetic wave can be generally decomposed into the summation of right- and left-handed elliptically (or circularly) polarized waves. If a media or a system interacts differently with right- and left-handed elliptically polarized waves, the polarization plane of the electromagnetic wave is affected. The difference in the interaction takes place since certain media poses different refraction indexes for right- and left-handed elliptically polarized waves, i.e. n_+ and n_- thus, there is a phase difference between these two waves as they propagates in such a media. This results in the rotation of polarization plane of electromagnetic wave [42] as shown in Fig. 2.1. Such a media is also called *optically active* or *chiral media* and can be found in nature like sugar molecules. The reason that the medium behaves differently for right- and

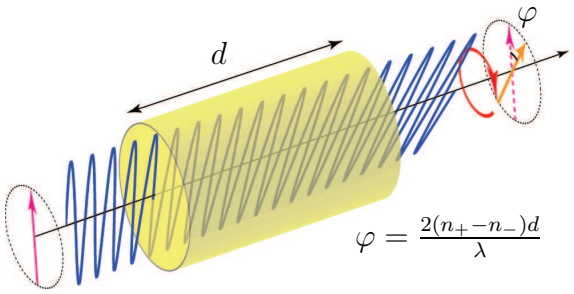

Figure 2.1 Electromagnetic response of a gyrotropic media [2].

left-elliptically polarized wave is the handedness of the structure so that the mirror images of the structure does not overlap with itself. The gyrotropy is excessively used in spectroscopic applications such as the detection of the amount of chiral molecules in solvents.

Apart from the gyrotropy, non-reciprocity is another exciting and important property that a medium can have under certain conditions. Non-reciprocity can be described as a system or a media which cannot return back to its original state when the time is reversed. Thus, non-reciprocal systems does not pose the time-reversal symmetry. In microwave engineering this statement translates to

$$S_{21} \neq S_{12}, \tag{2.1}$$

where the received power from port 2, when port 1 is excited is different than the received power from port 1 when port 2 is excited with the same power. Non-reciprocal media can be realized with natural materials such as magnetized ferrites, plasmas, or magneto-optic materials.

Although gyrotropy and non-reciprocity are different concepts as summarized above[1], there is also phenomena called *non-reciprocal gyrotropy*, used to build many non-reciprocal components such as isolator, circulators and variable phase shifters for the state-of-the-art telecommunications and radar applications. Non-reciprocal gyrotropy is a response of certain materials such that the medium rotates the polarization plane of an electromagnetic wave by a different amount other than negative of the rotation angle when the medium excited from the receiving port with same transmitted field pattern (time reversed case), as can be seen in Fig. 2.2. The rotation angle is named *Faraday rotation angle* after the discovery of phenomenon by Michael Faraday. Non-reciprocal gyrotropy can be seen in natural materials such as ferrites, plasmas, graphene [44] or magneto-optic materials when they are biased with a static magnetic field.

2.1.1 Microscopic and Macroscopic Properties of Ferrimagnetic Materials

Ferrimagnetic materials (ferrites) exhibit non-reciprocal gyrotropic response when they are biased with a static magnetic field. Ferrite materials are one of the most widely used non-reciprocal materials in industrial applications so that it is important to understand their microscopic and macroscopic properties. In natural solids, electron spins that creates magnetic dipole moment occurs randomly so that the overall magnetic response of the materials

1. Note that in optics community gyrotropy refers to a non-reciprocal response so that each gyrotropic media is also a non-reciprocal [43]. However, during this thesis we will treat non-reciprocity and gyrotropy separately.

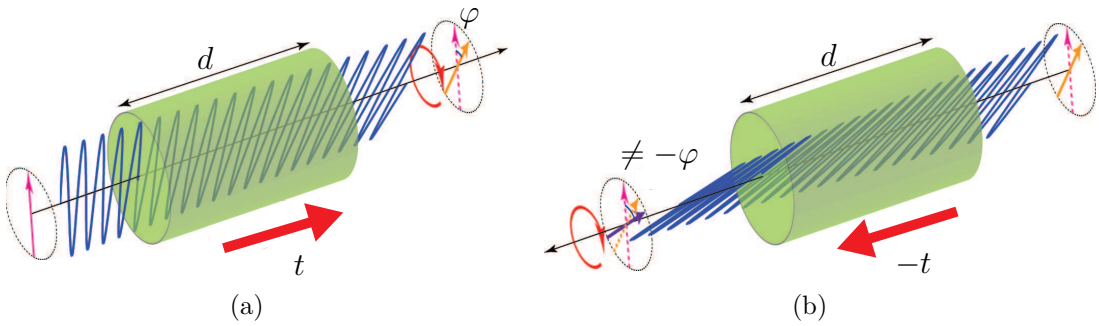

Figure 2.2 (a) Illustration of a reciprocal gyrotropy. (b) Illustration of a non-reciprocal gyrotropy (time-reversal case) [2].

is zero. However when magnetic materials are biased with a static magnetic field, electron spins are not random due to the torque excreted on electrons, so that electrons spin around a fixed axis aligned with the direction of the biasing static magnetic field, as can be seen in Fig. 2.3. Thus, such a media produce a large overall magnetic response.

Macroscopic response of the ferrites can be derived from their microscopic picture by considering magnetization as a superposition of magnetic dipole moments. This analysis rigorously done in [3], and magnetic response of the ferrites characterized by their permeability tensor when they are biased with a $+\mathbf{e_z}$ directed static magnetic field under time convention $e^{j\omega t}$ [2] as

$$\bar{\bar{\mu}} = \begin{bmatrix} \mu & j\kappa & 0 \\ -j\kappa & \mu & 0 \\ 0 & 0 & \mu_0 \end{bmatrix} \tag{2.2}$$

where $\mu = \mu_0(1+\chi_{xx}) = \mu_0(1+\chi_{yy})$, $\kappa = -j\mu_0\chi_{xy} = j\mu_0\chi_{yx}$ and χ_{xx}, χ_{xy}, χ_{yx}, χ_{yy} are the components of susceptibility tensor of a ferrite. The first observation from (2.2) is that the permeability tensor of the ferrite has non-diagonal components hence, gyrotropic response of the magnetized ferrites is evident. This can be easily understood by considering the constitutive relation $\mathbf{B} = \bar{\bar{\mu}} \cdot \mathbf{H}$ where the x component of magnetic induction vector has contribution both from x and y component of the magnetic field. In addition, as known from the reciprocity theorem [45, 46], the reciprocal bi-anisotropic media that electric and

2. This time convention will be used throughout this thesis.

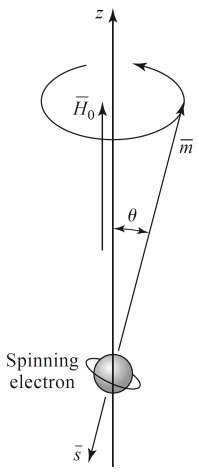

Figure 2.3 Illustration of a spinning electron around the direction of biasing static magnetic field [3].

magnetic current sources radiate has to satisfy the following equations

$$\begin{aligned} \bar{\bar{\varepsilon}} &= \bar{\bar{\varepsilon}}^T, \\ \bar{\bar{\mu}} &= \bar{\bar{\mu}}^T, \\ \bar{\bar{\zeta}} &= -\bar{\bar{\xi}}^T, \end{aligned} \tag{2.3}$$

where $(.)^T$ is the Hermitian operator, $\bar{\bar{\zeta}}$ and $\bar{\bar{\xi}}$ are electric-magnetic and magnetic-electric coupling tensors, respectively. According to (2.2), it can be clearly seen that the ferrite media is non-reciprocal hence, ferrites has a non-reciprocal gyrotropic response.

The underlying physics of non-reciprocal and gyrotropic responses of a magnetized ferrite can be better understood by considering interaction of electromagnetic waves with ferrite molecules. Since the spinning electrons follow a circular trajectory, the propagating eigenstates that will fundamentally interact with ferrite molecules are circularly polarized waves. The interaction of magnetized ferrites with Right-handed Circularly Polarized (RCP) and Left-handed Circularly Polarized (LCP) waves are illustrated in Fig. 2.4, so that due to the forced right-handed rotation of an electron spin under the $+\mathbf{e_z}$ directed biasing field, the RCP wave will amplify the rotation radius of the electron spin and provide larger rotating magnetic dipole moment in transverse plane, however the LCP wave will damp the rotation radius and decrease the overall magnetic dipole moment. Since magnetized ferrite interact differently with RCP and LCP wave, the medium shows a gyrotropic property. Thus, the magnetized ferrites provides different refraction index for RCP and LCP waves, i.e. $n_+ = \sqrt{\mu + \kappa}$,

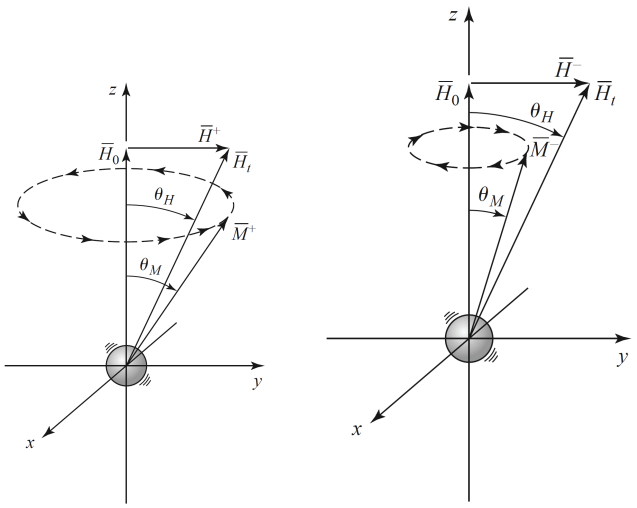

Figure 2.4 (a) Illustration of interaction of the RCP plane wave with a magnetized ferrite electron biased with $+\mathbf{e_z}$ directed biasing magnetic field. (b) Illustration of interaction of the LCP plane wave with magnetized ferrite electron biased with $+\mathbf{e_z}$ directed biasing magnetic field [3].

$n_- = \sqrt{\mu - \kappa}$, respectively. In addition, due to the pre-determined direction of the forced rotation, RCP propagating wave from the left side of the media will interact with that media similarly as in the case of the LCP propagating wave from the right hand side of the media. Therefore, if the rotation of linearly polarized wave from the left to the right side of the structure is characterized with angle θ, once the time is reversed the linear polarized wave will experience an additional θ rotation so that the system cannot return to its original state. Therefore, the biased ferrites has non-reciprocal gyrotropic response.

So far, the natural materials that provide non-reciprocal gyrotropy are ferrites and plasmas. Both of them is extensively used in many applications ranging from microwave to optical frequencies, however they exhibit their non-reciprocal gyrotropic responses when they are biased with a static magnetic field. The static magnetic fields is generally provided by permanent magnets which are bulky, non-integrable, opaque and expensive. Therefore, the need for light, integrable, transparent and cheap way of achieving non-reciprocal gyrotropy provides impetus for scientist to seek an artificial media that can replaces the magnetized ferrites and plasmas.

2.2 MNMs Technology

As discussed in the previous section, non-reciprocal response requires time-reversal asymmetry of the system and is only achieved with magnetized ferrites or plasmas. The requirement of the time-reversal asymmetry is firstly suggested in the scope of Onsager's principle of microscopic reversibility [47] where Casmir showed that in the presence of magnetic field, the conduction of electricity is an odd vector under time-reversal. The principle of microscopic reversibility can also be applied to explain the non-reciprocity of magnetized ferrites since the magnetic induction vector is also odd vector under time-reversal.

Scientists showed a great interest to replace the ferrites and ferrite based devices with lightweight, cheap, transparent and integrable artificial materials, in order to overcome the drawbacks of using permanent magnets to bias ferrites. Thus, they look for the quantities that are odd vector under time-reversal, such as magnetic field, current density, linear momentum and angular momentum [48], to realize artificial magnet-less non-reciprocity.

The first magnet-less non-reciprocity was realized by Yu et. al [37, 4] and they utilized the linear momentum vector to break the time reversal symmetry. The idea behind their design was to excite indirect photonic transitions by using spatiotemporal modulation of the refraction index along a silicon photonic waveguide. Modulation of the refraction index also spatially modulate the momentum vector in time since the wavenumber along the waveguide changes, like modulation of a wave vector with gratings. The forward propagating eigenstate makes a transition to another mode while the backward eigenstate stays in the same mode, as can be seen in Fig. 2.5(a). Thus, the isolation and non-reciprocity is achieved. The design was verified experimentally [49] and paved the way for achieving magnet-less non-reciprocity, despite its drawbacks such as non-gyrotropy, fabrication difficulties and large foot print.

Apart from the first demonstration of non-reciprocity, Toshiro et. al [8] for the first time suggested a non-reciprocal gyrotropic metasurface based on odd symmetry of the current under time reversal. Their design is exactly mimicking the spinning electron behaviour of magnetized ferrites, i.e. rotating magnetic dipole moment in plane transverse to biasing direction, by forcing current via transistor to flow in right- or left-handed along circular conducting ring pair as can be seen from Fig. 2.5(b). This results in different interaction mechanisms for RCP and LCP waves so that the non-reciprocal gyrotropy is achieved. Although the design has found a lot of novel applications in microwave such as isolators [38, 50], circulators [38], leaky-wave antennas [51] and PEMC boundaries [52], it cannot be implemented for an application requiring transparency due to presence of the biasing network.

Lastly, Sounas et. al [6] used the orbital angular momentum which has odd vector symmetry under time-reversal to achieve magnet-less non-reciprocity (L-MNM). The design is

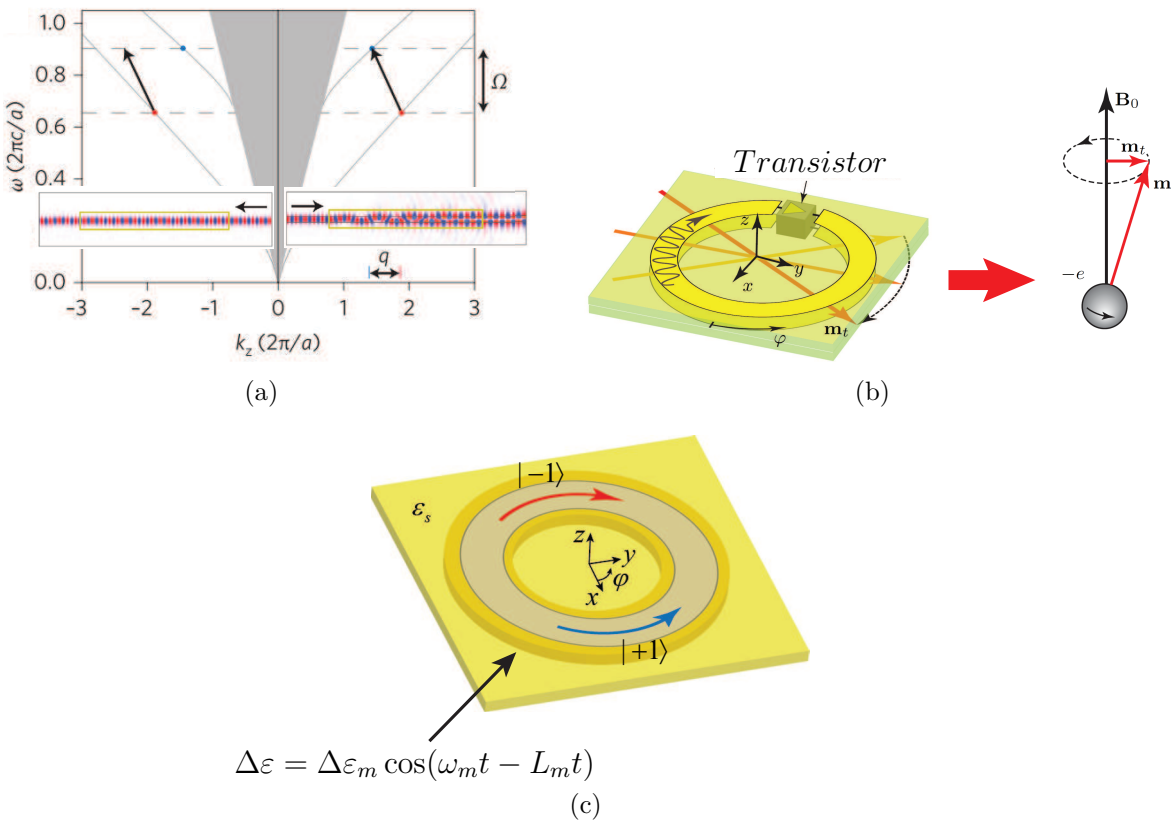

Figure 2.5 (a) Band structure of spatiotemporally modulated silicon waveguide [4]. (b) Illustration of I-MNMs based on current biasing and electron spin of magnetized ferrites [5]. (c) Illustration of L-MNMs based on azimuthal spatiotemporal modulation of the refraction index along conductive ring pair structure and its counter-propagating eigenstates [6].

realized with azimuthal spatiotemporal permittivity modulation of a ring resonator via varactors, such that the eigenstates of the structure, RCP and LCP propagating wave inside the ring cavity, is not degenerate anymore. Therefore, the structure interacts mainly with RCP and LCP waves at different frequencies and the non-reciprocal gyrotropy is achieved. Although the design led the way of realizing on-chip optical magnet-less non-reciprocal components such as isolators [39] and circulators [40], it could not be implemented as a metasurface due to its complicated permittivity modulation circuitry. All presented methods to achieve magnet-less gyrotropy has some advantages and disadvantages. However with the advent of nanotechnology and fabrication methods such as MMIC, there is a huge potential to implement smaller, non-bulky and integrable unprecedented non-reciprocal components.

2.2.1 MNMs Based on Current Biasing

The rest of the thesis focuses on solving the issues related to the MNMs based on time-reversal asymmetry of the current (I-MNM). Thus, the details of their physical mechanism should be discussed. As stated in the previous section, the design mimics the behaviour of an electron spinning of magnetized ferrites. Therefore, the 2D periodic array of conducting ring pairs loaded with a semiconductor-based unidirectional component is considered to simulate the behaviour of the rotating magnetic dipole moment. The designed structure has two modes of operation under plane wave illumination, even mode and odd mode as can be seen in Fig. 2.6(a) and 2.6(b), respectively. Due to sub-wavelength thickness of the substrate, electric field across the substrate can have both even and odd character if Taylor expansion of the field is considered. Therefore, the even mode operation corresponds to the case where the induced current at the top and bottom ring has even symmetry according to $z = 0$ plane, odd mode operation corresponds to odd symmetry of currents. Since the electric current loop creates a electric quadrupole and magnetic dipole moment, the odd mode operation yields magnetic dipole and electric quadrupole moment as can be seen in Fig. 2.6(c). In addition, the even mode only induces reciprocal gyrotropic electric dipole moment.

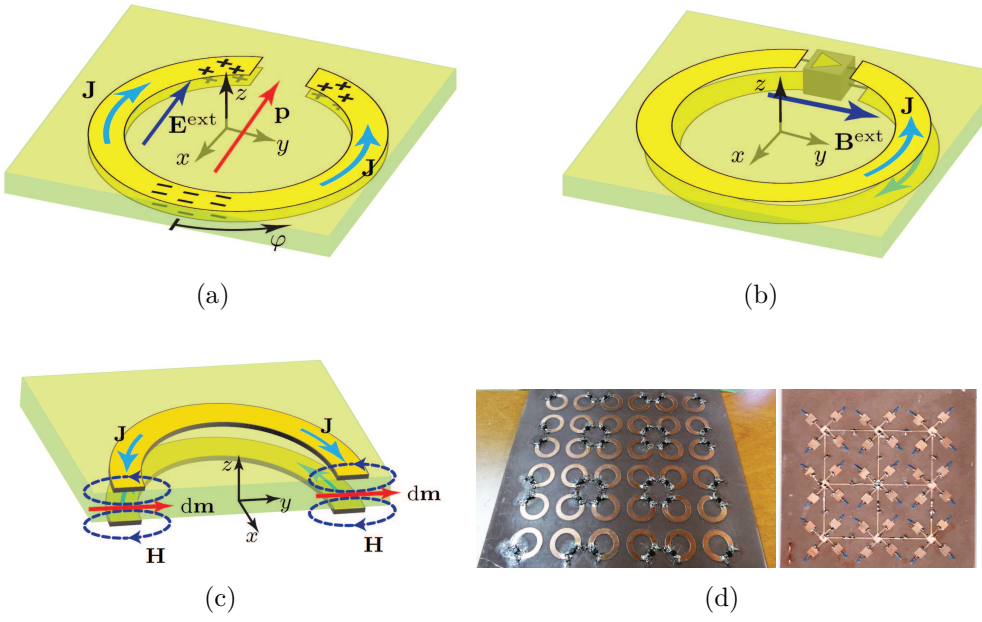

Figure 2.6 (a) Illustration of even mode operation of the microstrip I-MNM. (b) Illustration of odd mode operation of the microstrip I-MNM. (c) Illustration of the induced magnetic dipole moment by odd mode of the microstrip I-MNM [7]. (d) Fabricated microstrip I-MNM, top and bottom of the substrate [8].

The unloaded conducting ring pair has two counter-propagating eigenstates, namely right- and left-handed. When the semiconductor-based unidirectional component is connected to the end of conductive ring pair as in Fig. 2.6(b), propagation of one of the eigenstates is prohibited so that time-reversal symmetry is broken. This is called travelling wave resonance such that the current wave is azimuthally rotating along the conductive ring pair since accumulated phase of the propagating states and phase shift of the unidirectional component adds up to 2π. This resonance creates a rotating magnetic dipole moment as in the case of magnetized ferrite. The analytical modelling of the microstrip I-MNM is rigorously done in [7] so that its microscopic and macroscopic properties are derived. However, practical implementation of such a conducting ring pair is not effective due to the need for a ground plane in order to bias the semiconductor-based unidirectional component. Therefore, unit-cell of the microstrip I-MNM is fabricated, as presented in Fig. 2.6(d) and magnet-less non-reciprocal gyrotropic response experimentally achieved only for reflected waves. Thus, the microstrip I-MNMs has reflective-type (non-transparent) magnet-less non-reciprocal response. However most of the industrial applications require a transparent non-reciprocal devices with minimal reflection such as waveguide isolators, polarizers, etc. Therefore, the need for the transparent magnet-less non-reciprocal gyrotropic devices is inevitable. The rest of the thesis is focused on solving this issue.

CHAPTER 3 SINGLE-LAYER SLOT TYPE TRANSPARENT MNMs

In this chapter, a transparent MNM [1] based on a slot line structure is designed and analyzed. In the first section, the design details is explained and non-reciprocity and gyrotropy of the designed transparent MNM is shown based on reflection and transmission coefficients of the structure. In the second section, the physical explanation of non-reciprocity and gyrotropy of the transparent MNM is given based on the unilateral current distribution of the structure. Later, the third chapter focuses on the electromagnetic characterization of the transparent MNM. Then, based on the bi-anisotropic surface parameters of the structure, transmission line model of the transparent slot MNM is suggested for modeling the multi-layer structures.

3.1 Transparent MNMs Design

The microstrip MNMs has an important limitation where they can only be used for applications requiring only the reflected fields due to the ground plane in biasing network of the FET. In order to cope with this problem, the straightforward idea is to think of a complementary structure based on Babinet principle, where the PEC parts are replaced by a gap and vice-versa. In this complementary structure, the odd symmetry of magnetic currents form a magnetic current loop and create rotating electric fields according to Amperé law, i.e. the rotating electric dipole moment response. Thus, the complementary structure will be non-reciprocal gyrotropic based on its rotating electric dipole moment response instead of the magnetic one as in the case of microstrip MNMs. However, such a complementary structure has not been realized yet due to the need for an unidirectional component that works for magnetic charges. Therefore, the Babinet principle cannot directly be applied for the design of transparent MNMs. However, the Babinet principle could still be exploited as a starting point of the transparent MNMs design.

Response of the microstrip MNMs are based on traveling wave resonance as they mimic the behaviour of magnetized ferrite molecules. This resonance is achieved by using a unidirectional component whose biasing requires a ground plane. Thus, it can be reasonable to think of a structure which provides a co-planar ground plane for the biasing of the FET. The simplest structure which has a co-planar ground plane would be a slot line, a complementary of a microstrip line structure.

In Fig. 3.1(a), a slot line is utilized to design a transparent MNM where the terminations

1. Since the thesis focuses on I-MNMs, the *I* prefix is dropped for the rest of the thesis.

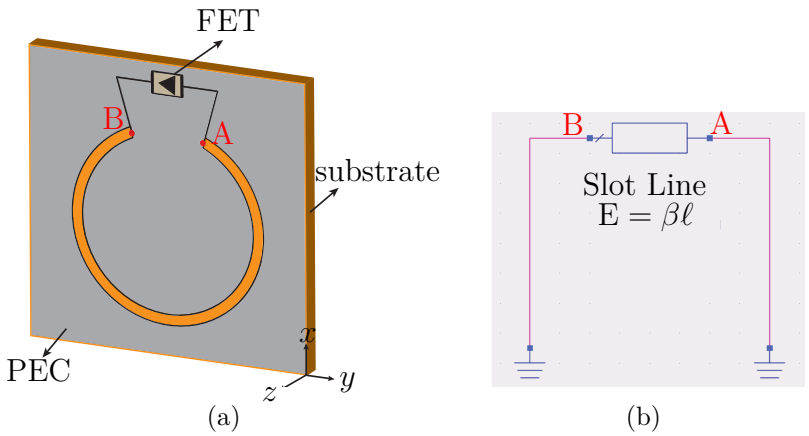

Figure 3.1 (a) Slot MNM design based on the Babinet principle. (b) The transmission line model of the designed Slot MNM with electrical length $\beta\ell$.

of the slot line are connected through a FET in order to achieve a travelling wave resonance. However as can be seen from the transmission line model of the structure in Fig. 3.1(b), the terminations of the slot line are short-circuited, as the open-circuit termination of microstrip line, so that the current along the slot line cannot be coupled to the FET. As a result, this simple design based on Babinet principle cannot be used directly.

The structure shown in Fig. 3.1(a) can be modified by using an impedance matching technique to couple the power along the slot line into the FET. The basic matching can be done by connecting a very high impedance termination at the points A and B in Fig. 3.1(a). The high impedance termination could be implemented by using a bigger slot line as done in Fig. 3.2(a). Transmission line model of the structure shown in Fig. 3.2(a) can be seen in Fig. 3.2(c) where Z represents the input and output impedance of the FET circuit [2], slot line 1 corresponds to the annular slotted ring and slot line 2 and 3 corresponds to the matching terminations. Ideally, the infinite impedance termination should make the impedance at the points A and B open-circuit since it is enough to satisfy the equality of the annular slot line impedance Z_1 and the FET input and output impedance Z. However, due to the highly dispersive, non-linear behaviour of the slot line impedance, as can be seen in Fig. 3.3(a) and 3.3(b), even very high values of slot line impedance cannot be realized for the microwave applications. There are closed-form expressions for calculating the impedance and the effective permittivity analytically, however they are only valid under certain parameter ranges. These formulas are given in [53] and used throughout this thesis for designing

2. The input and output impedances of FET can generally be different, here the proof of concept is shown where the impedances are same.

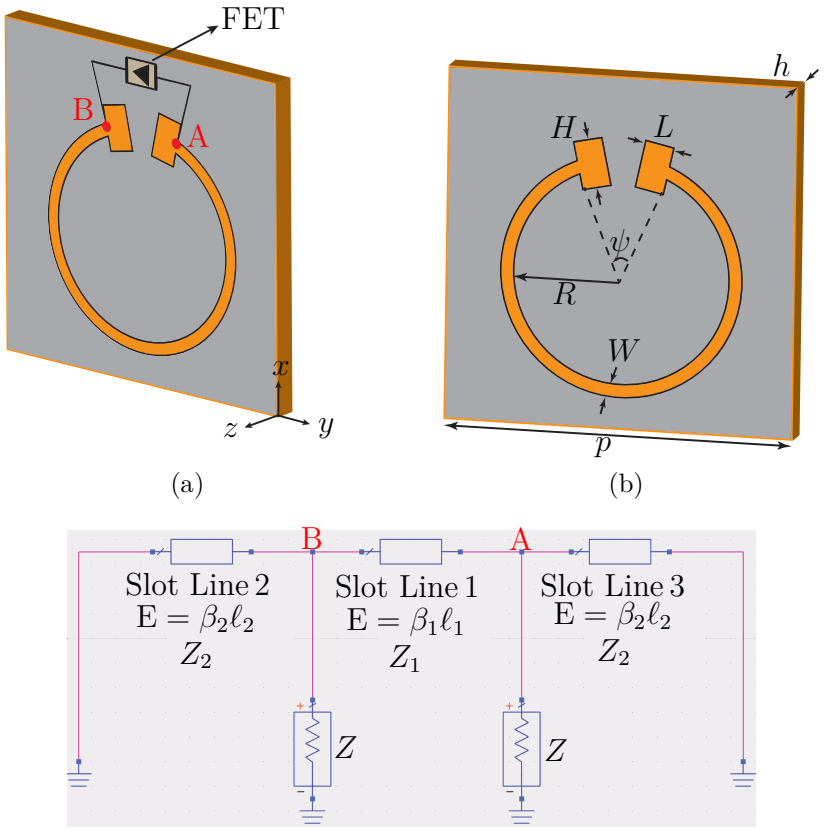

Figure 3.2 (a) Modified slot MNM design based on the Babinet principle. (b) Annular slotted ring structure with its design parameters. (c) Transmission line model of the modified slot MNM.

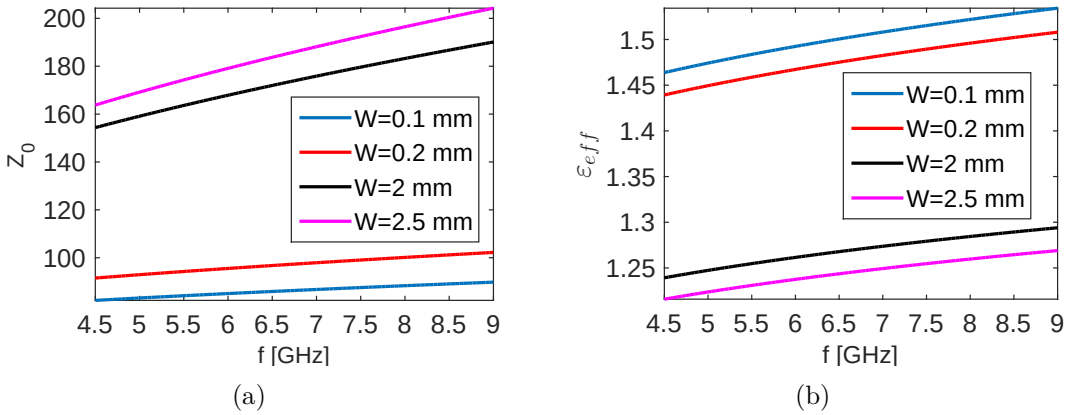

Figure 3.3 (a) Characteristic impedance of a slot transmission line for different slot widths. (b) Effective permittivity of a slot transmission line for different slot widths. Thickness of the substrate is 0.8 mm, relative permittivity of the substrate is 2.6.

transparent MNMs. The closed-form expressions are only valid when $0.0015 \leq W/\lambda_0 \leq 1.9$, $0.006 \leq h/\lambda_0 \leq 0.06$ and $2.22 \leq \varepsilon_r \leq 9.8$, where W is the width of the slot line, h is the thickness of the substrate and ε_r is the permittivity of the substrate [53]. The difficulty of determining the electromagnetic response of a slot line is originated from its inherent field distribution such that the field lines are not concentrated into substrate as opposed microstrip line. As it will be seen later, these properties impose some restrictions on the transparent MNM design.

In order to have a rotating magnetic dipole moment response in a transverse plane, the unloaded structure shown in Fig. 3.1(a) should have a magnetic dipole moment response. Indeed as it can be seen from the sketched current and field distributions of the unloaded structure in Fig. 3.4(a) under plane wave illumination, the unloaded structure has a magnetic dipole response, characterized with the magnetic field lines, in the plane transverse to $\mathbf{e_z}$ direction. Since the incident electrical field is directed into $-\mathbf{e_x}$ direction, there will be charge a accumulation across the slot at the top and the bottom of the ring. This charge accumulation will create out-of phase counter-propagating currents around the slot. As can be seen in Fig. 3.4(b), the magnetic field lines are perpendicular to the PEC plane along slot since the counter-propagating currents forms a loop due to the subwavelength thickness of the slot and produce magnetic fields perpendicular to $x-y$ plane. In addition, direction of the magnetic field lines along the slot depends on whether the counter-propagating currents forms a clockwise or a counter-clockwise loop. Therefore, the magnetic field lines are in the direction of $+\mathbf{e_z}$ and $-\mathbf{e_z}$ as can be seen in Fig. 3.4(a). These two out-of phase perpendicular magnetic field lines have to form a loop because of the non-existence of the magnetic charges (solenoidal nature of magnetic field lines) as in Fig. 3.4(b). The additional magnetic field lines drawn in Fig. 3.4(b) depicts the interaction of the neighboring unit-cells since the magnetic field lines around the slot should close on themselves. Thus, the unloaded annular slotted ring structure can be characterized with a magnetic dipole moment which has a transverse component in $x-y$ plane and perpendicular components in $+\mathbf{e_z}$ and $-\mathbf{e_z}$ directions.

The unloaded annular slotted ring structure as shown in Fig. 3.4(a) shows a standing wave pattern in time domain such that the magnetic field lines are in the direction of either $+\mathbf{e_y}$ or $-\mathbf{e_y}$. In order to achieve a magnetized ferrite-like non-reciprocal gyrotropic response one needs a rotating magnetic moment, which can be achieved by loading the annular slotted ring structure with an unidirectional component to break the time-reversal symmetry. If the unidirectional component is perfectly matched to the annular slotted ring structure at points

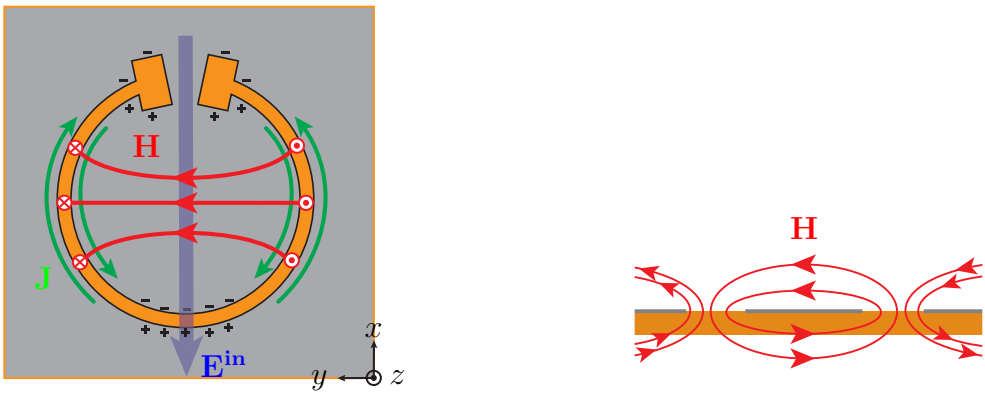

(a) (b)

Figure 3.4 (a) Transverse current and field distribution of the modified annular slotted ring structure. (b) Cross section view of magnetic field distribution of the modified annular slotted ring structure.

A and B of Fig. 3.2(a), the structure shows a travelling wave resonance under the condition

$$\beta\ell + \varphi_{is} = 2\pi m, \tag{3.1}$$

where β is the propagation constant of the right- or left-handed propagating eigenstates, ℓ is the physical length of the slotted transmission line defined as $\ell = (2\pi - \theta)R$, φ_{is} is the phase shift of the unidirectional component and m is an integer. Since the right- or left-handed propagating current wave is absorbed by the unidirectional component based on the direction of the isolation, only the propagating eigenstate can accumulate the phase of $\beta\ell$ from point A to B in Fig. 3.2(a), and after passing through the unidirectional component, an additional phase shift of φ_{is} is added up. Thus, if the total accumulated and added phase are equal to integer multiples of 2π, the travelling wave resonance can be achieved so that the current wave along annular slotted ring in Fig. 3.4(b) starts to rotate. The expected time evaluation of the current wave and magnetic field lines, namely the magnetic dipole moment, at the travelling wave resonance[3] can be seen in Fig. 3.5, such that the rotation of the magnetic dipole moment is clearly observed. Thus, a magnetized ferrite-like transparent artificial non-reciprocal gyrotropic response can be realized.

The physical working mechanism of the slot MNMs is summarized above. In order to understand the electromagnetic response of the structure, the actual design should be implemented and its numerical or the theoretical results should be computed. The first step in

3. Under ideal conditions.

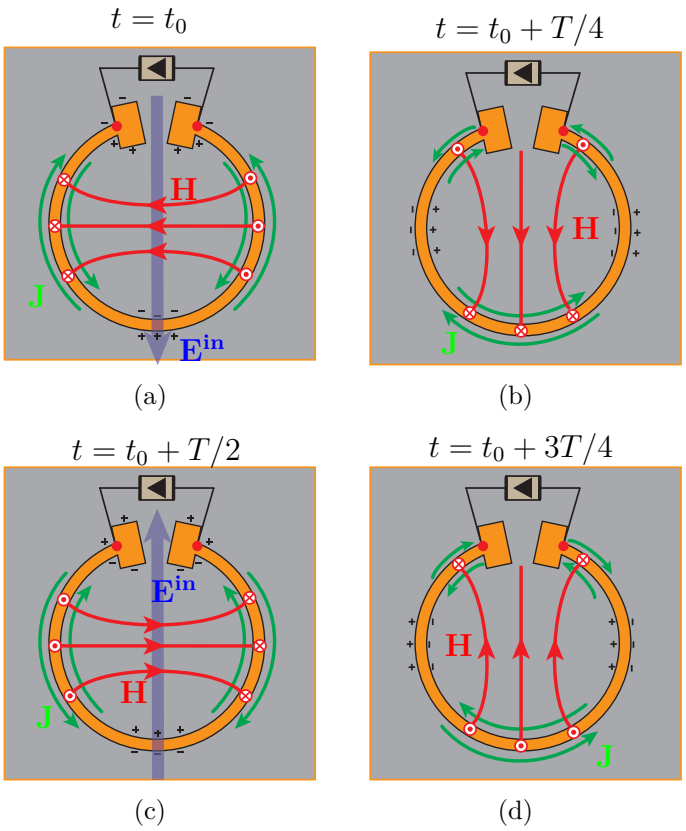

Figure 3.5 Transverse current and field distribution of the designed slot MNM at different time instances. (a) $t = t_0$. (b) $t = t_0 + T/4$. (c) $t = t_0 + T/2$. (d) $t = t_0 + 3T/4$ where T is period of the incident plane wave.

design phase is the determination of the resonance frequency where non-reciprocal gyrotropic response will appear. Thus, radius of the annular slotted ring R, the permittivity of the substrate ε_r, the thickness of the substrate t and the width of the slot W, shown in Fig. 3.2(b), should be determined. The design frequency is set to 5.3 GHz and the determined design parameters are given in Table 3.1. The annular slotted ring has a physical length of $\lambda_g/2$ at 5.3 GHz.

Table 3.1 Design parameters of the slot MNM resonating at 5.3 GHz.

Parameter	Value	Parameter	Value
ψ	20°	R	3.75 mm
ε_r	2.6	h	0.8 mm
W	0.1 mm	p	11 mm
L	2.5 mm	H	0.6 mm

The most important part of the design is the determination of the parameters H and L since these two parameters are controlling the matching between the unidirectional component and the annular slotted ring. In order to design the big slot termination shown in Fig. 3.2(a), the circuit representation of the slot MNM given by Fig. 3.2(c) should be considered so that impedance of the input and output port of the unidirectional component Z are determined to minimize the reflections at those ports. At 5.3 GHz, the electrical length of the annular slotted ring and big slot are calculated as $\beta_1\ell_1 = 180°$, $\beta_2\ell_2 = 4.2°$ where the impedance and the effective permittivity of slot transmission lines determined from Fig. 3.3(a) and 3.3(b) as $Z_1 = 84\,\Omega$, $Z_2 = 172\,\Omega$ and $\varepsilon_{eff} = 1.48$, $\varepsilon_{eff} = 1.22$, respectively. Circuit model of the structure seen in Fig. 3.2(c) simulated by using tuning tool of Advanced Design Software (ADS) where the input and output port impedances of the unidirectional component Z is changed until the best matching condition is achieved. The design process should be modified by changing the dimensions of the big slot in order to achieve the matching in the validity range of the slot line impedance formulas. In Fig. 3.6(a), the magnitude of S-parameters at ports A and B in the Fig. 3.2(a) is calculated by using ADS. It is clearly seen that the matching at 5.3 GHz is achieved when the input and the output impedances of the unidirectional component equals to one ohm, however the matching achieved for a small bandwidth. In addition, in Fig. 3.6(b), the phase of S-parameters from point A to B of Fig. 3.2(a) is plotted, and at the resonance the phase change is 180° since the electrical length of annular slotted ring is also $\lambda_g/2$. In addition, the designed $2D$ periodic array of the annular slotted ring is simulated in High Frequency Structural Simulator (HFSS), where the full wave electromagnetic response of the structure is calculated. In HFSS, two lumped ports are added to the annular slotted ring structure in order to make the connection of the unidirectional elements. The lumped ports are basically rectangles in $x-y$ plane and fits into the slot at the proximity of the connection of big slot and the annular slot line. Due to the validity range of the slot line impedance formulas and the periodicity when $Z = 1\,\Omega$ the S_{11} of points A and B are close to -1 dB in HFSS simulation at 5.3 GHz. Since the circuit simulator does not take into account the electromagnetic effects such as periodicity or curvature of the transmission line limits the usage of the circuit simulators in the design process. Therefore, the parametric sweep of different impedance values is done for the matching and at $Z = 30\,\Omega$, reflection coefficients at ports A and B are smaller as it can be seen from Fig. 3.6(d). However, as opposed to what is expected, the phase change from point A to B is computed as $-127°$ instead of 180°. The deviation of the electrical length of the structure from its designed value is unwanted since it directly effects the design parameters and resonance frequency as it can be seen from (3.1). Thus, it is clear that ADS design procedure based on the transmission line model of the

structure cannot be utilized to design a slot MNM, but can be used as a priori information. The right method is to design such a structure requires a full-wave electromagnetic simulator where there is no issue with the validity range of the slot line impedance formula and the periodicity effects. However for an each design a fine tuning of the structure parameters is required for the intended design frequency. Therefore, it would be a very difficult task to provide a systematic way of designing slot MNM.

After designing the big slot termination for matching of the annular slotted ring and the unidirectional component, the unidirectional component can safely be connected between points A and B as seen in Fig. 3.2(a) in order to complete the design. Since HFSS can only calculate the full-wave electromagnetic response of the structure, the loading of the structure cannot be realized in HFSS. The loading of the annular slotted ring structure can be done by using the S-parameters of the periodic structure. The details of loading the annular slotted ring with an unidirectional component and calculating its electromagnetic response is given

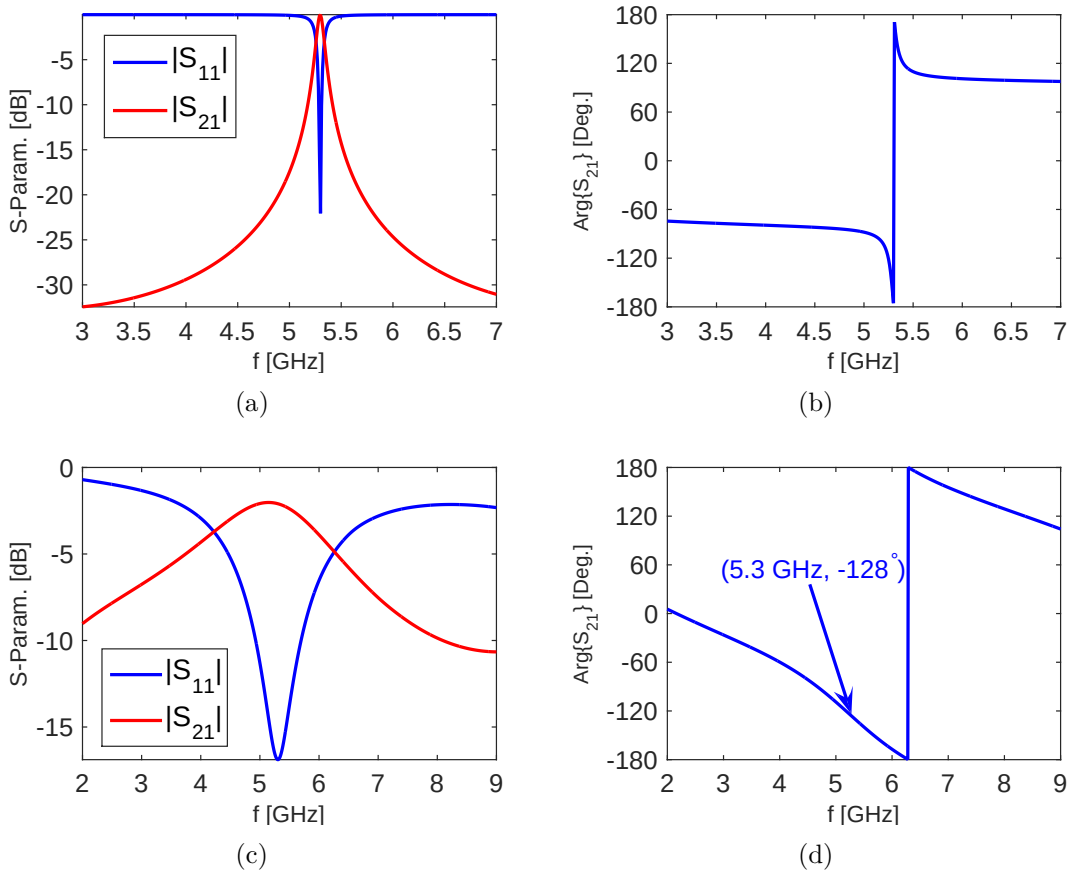

Figure 3.6 S-parameters of the ports A and B, shown in Fig. 3.2(c). (a) Magnitude of S_{11} and S_{21} computed by ADS. (b) Phase of S_{21} computed by ADS. (c) Magnitude of S_{11} and S_{21} computed by HFSS (d) Phase of S_{21} computed by HFSS.

in Appendix A where the signal flow graph of the cascaded structure is used. [4] The periodicity of the slot MNM, p, is selected such that only the zeroth order Floquet modes namely TM^z and TE^z plane waves can propagate. In addition, in the simulation, an ideal microwave isolator is used as an unidirectional component whose S-parameters are given by

$$[\mathbf{S_{is}}] = \begin{bmatrix} 0 & 0 \\ e^{j\varphi_{is}} & 0 \end{bmatrix}, \tag{3.2}$$

where φ_{is} is the phase shift of the ideal isolator such that the only RCP propagating eigenstate is allowed. The details of unidirectional component implementation by using common source FET can be found in Appendix B.

In Fig. 3.7(a) and 3.7(b) [5], reflection and transmission dyadics of the slot MNM with parameters given in Table 3.1 are plotted for TM^z (x-polarized) and TE^z (y-polarized) illumination, respectively. The phase shift of the isolator, φ_{is}, is selected as 128° in order to satisfy the resonance condition (3.1). It can be clearly seen that at 5.3 GHz, the travelling wave resonance occurs so that the gyrotropic response is evident form T_{xy}^{21} and T_{yx}^{21} as expected from an artificial ferrite. The resonances as seen from the figures have a large bandwidth which shows that the quality factor of the structure is not very high. Moreover, the gyrotropic response of the structure can be well understood by comparing reflection and transmission coefficients of the microwave isolator loaded and unloaded annular slotted ring structure as done in 3.7(c) and 3.7(d). It is clear that the unloaded structure does not show any gyrotropic response so that the cross-polarized transmission coefficient for x- and y- polarized illumination (T_{yx} and T_{xy}) close to zero. However, when the isolator is connected to achieve the travelling wave resonance, the rotating magnetic dipole moment response appears, i.e. the strong gyrotropy. The transverse magnetic dipole moment response is also evident since the coefficients R_{yx} and T_{yx} are same, as seen in Fig. 3.7(a), because the magnetic dipole moment equally radiates to the both side of the structure due to the subwavelength thickness of the substrate. In addition, the co-polarized transmission and reflection coefficients under x- and y-polarized plane wave illuminations are quite different in Fig. 3.7 since the designed structure, Fig. 3.2(a) is asymmetric with respect to y-axis. This asymmetry can be clearly seen from reflection coefficients of the unloaded annular slotted ring in 3.7(c) and 3.7(d) where the structure has lower reflection level under x-polarized illumination than the y-polarized

4. The S-parameters of the loaded annular slotted ring structure can also be calculated by using any circuit simulator such as Ansoft Designer or ADS.

5. In this figure and the later ones, the superscripts 21 corresponds to transmission of TM^z, TE^z polarized electromagnetic plane waves from $+\mathbf{e_z}$ direction to $-\mathbf{e_z}$ direction and for 12 from $-\mathbf{e_z}$ to $+\mathbf{e_z}$ direction.

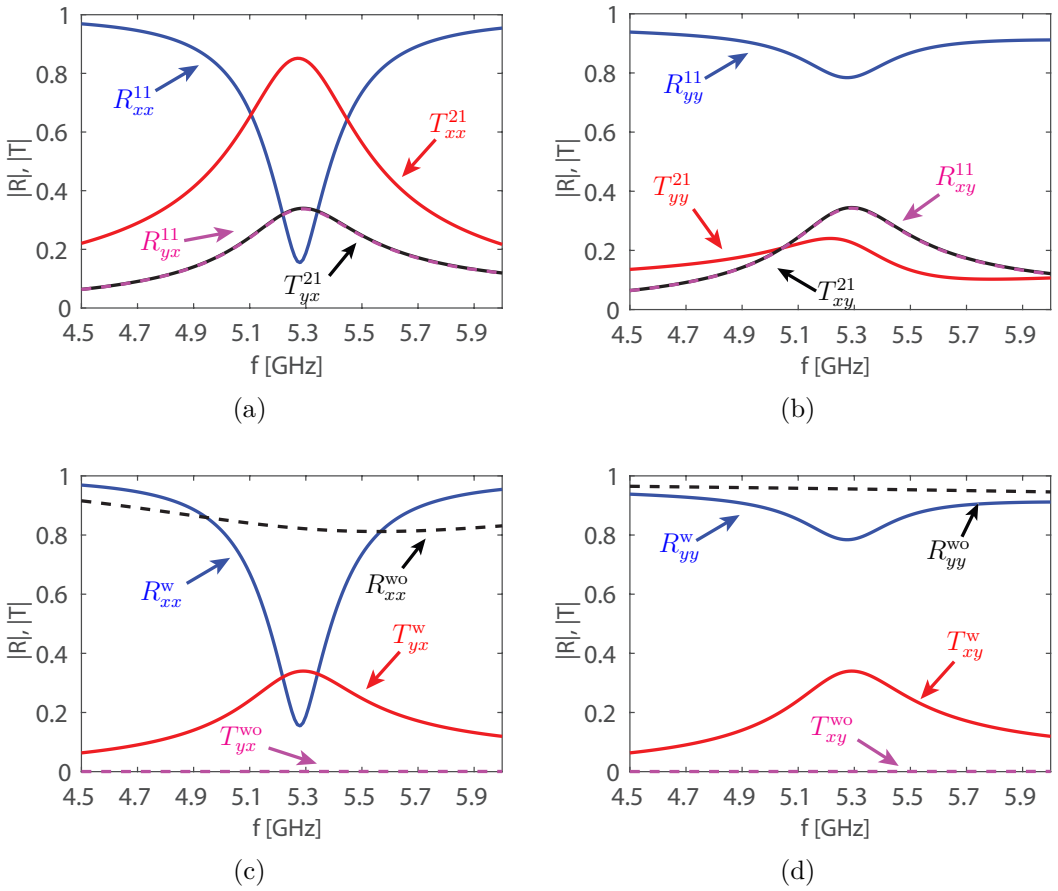

Figure 3.7 Reflection and transmission coefficients of the designed slot MNM based on the parameters given in Table 3.1 under plane wave illumination from $z > 0$.(a) x-polarized plane wave incidence. (b) y-polarized plane wave incidence. The comparison of reflection and transmission coefficients of the unidirectional component loaded (w superscript) and the unloaded structure (wo superscript) under plane wave illumination. (c) x-polarized plane wave incidence. (d) y-polarized plane wave incidence.

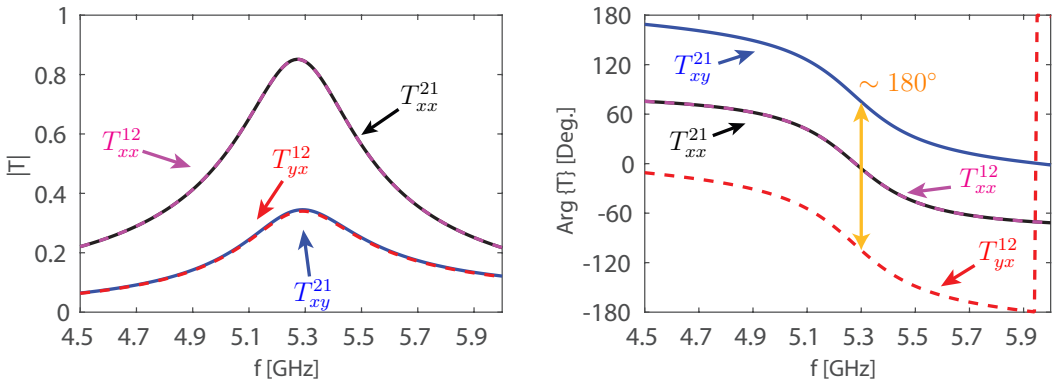

(a) (b)

Figure 3.8 Non-reciprocity of the designed slot MNM : Comparison of the transmission coefficients when the structure is excited from $z > 0$ and $z < 0$ in time-reversal schema. (a) Magnitude. (b) Phase.

one.

Lastly, in order to fulfill the requirement of being an artificial ferrite structure, the slot MNM should have a non-reciprocal response. In Fig. 3.8(a) and 3.8(b), the amplitude and phase of the transmission coefficient is plotted in time-reversal schema such that from port 1 to port 2, the x-polarized wave is transmitted and y-polarized probe pick the signal at region 1 and if the time is reversed, from port 2 to port 1, the y-polarized wave is transmitted and x-polarized probe pick the signal at port 2. For x-polarized illumination and x-polarized probing, amplitude and phase of the transmission coefficients are same when the time is reversed. Thus, as magnetized ferrites, the co-polarized component does not show any change in their magnitude and phase when the time is reversed, however the cross-polarized components shows 180° phase difference at the resonance frequency so that the designed slot MNM behaves like a magnetized ferrite where the permeability tensor has cross-components and they are out-of phase such that non-reciprocal gyrotropic response is evident from (2.3).

Although the non-reciprocal gyrotropic response of the slot MNM is clearly shown in Fig. 3.7 and 3.8(b), whether this response occurs due the rotating magnetic dipole moment has not been shown. Thus, in Fig. 3.9 and 3.10, time evaluation of the current and the transverse magnetic field distributions over PEC plane of the slot MNM is plotted by using the *Push Excitation* feature of the Ansoft Designer software where the computed S-parameters of the loaded structure under TE^z or TM^z excitation is pushed backed to the HFSS simulation. The ideal current and magnetic field distributions schematically shown in Fig. 3.5, however the simulation results somehow shows a distinct behaviour by comparing with the

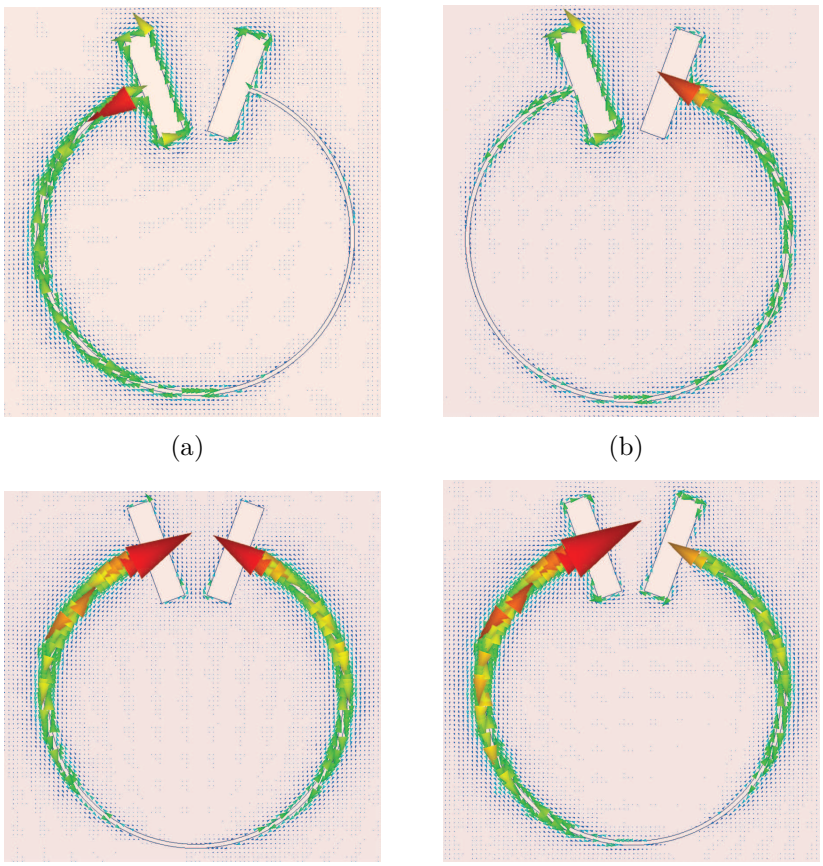

Figure 3.9 Time evaluation of the transverse electric current along unit-cell of the slot MNM computed by using HFSS and Ansoft Designer. (a) $t = t_0$. (b) $t = t_0 + T/8$. (c) $t = t_0 + T/4$. (d) $t = t_0 + 3T/8$.

ideal ones [6]. Although rotation of the current distribution is clear, the rotation is non-uniform where from $t = t_0$ to $t = t_0 + t/8$ and from $t = t_0 + T/4$ to $t = t_0 + 3t/8$, the current distribution shows a different change since the electrical length of the annular slotted ring is not the multiple of π. The clearer picture of the travelling wave resonance can be seen from the transverse magnetic field distribution of the slot MNM as shown in Fig. 3.10, where magnetic field lines rotate in right-handed direction so that the slot MNM shows a rotating magnetic dipole response. However, as also seen from the current distribution, rotation of the magnetic field lines are non-uniform (they do not have same amplitude along $x = 0$ and $y = 0$ at $t = t_0$ and $t = t_0 + T/4$, respectively). The first reason can be attributed to electrical length of the annular slotted ring, but more importantly effect of big slot and the neighbor cells cause this

6. Note that the ideal response is drawn for annular slotted ring whose electrical length is 360°, however the designed slot MNM's is −128°

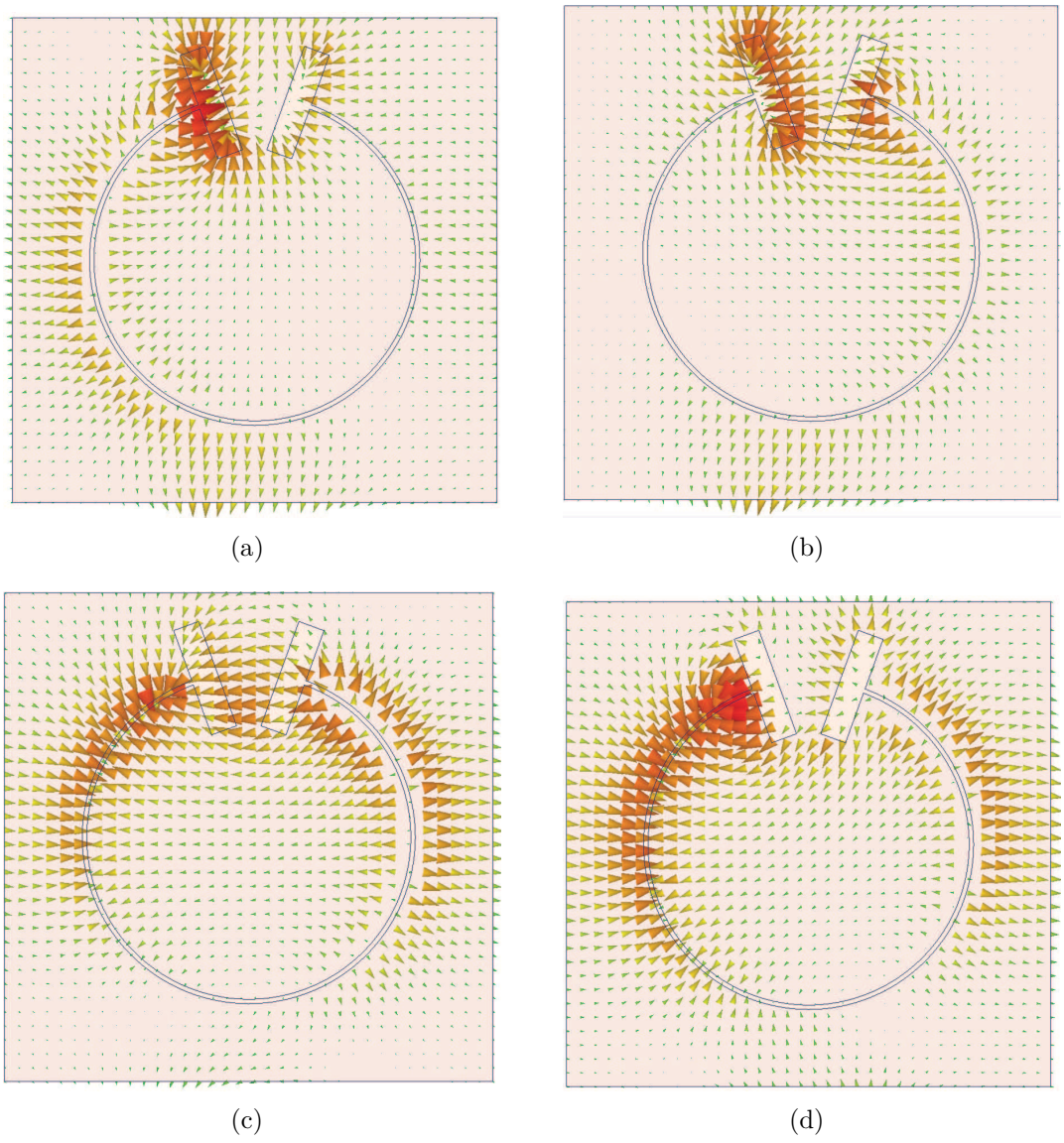

(a) (b)

(c) (d)

Figure 3.10 Time evaluation of the magnetic fields transverse to $\mathbf{e_z}$ direction along unit-cell of the slot MNM computed by using HFSS and Ansoft Designer. (a) $t = t_0$. (b) $t = t_0 + T/8$. (c) $t = t_0 + T/4$. (d) $t = t_0 + 3T/8$.

non-uniformity. It is clear that around annular slotted ring the magnetic field lines are cancelling each other so that effect of the rotating magnetic dipole moment response is restricted to the field lines at the center of the slot MNM and they are so small compared to the one around annular slotted ring. As it can be seen from Fig. 3.4(b), the effect of neighbor cells in $2D$ periodic array of slot MNM is strong. The perpendicular magnetic field lines created by the current loop around annular slotted ring encloses itself with the magnetic fields of the same unit cell and of the neighboring unit-cells. Therefore, even if the periodicity of the

structure is increased, the strong coupling between neighboring unit-cells, so the cancelling effect around annular slotted ring, is unavoidable. In addition, since impedance of the big slot patch is not very high, the current is flowing around the big slot and it strongly affects the distribution of magnetic field lines although this current is small compared to current flowing around annular slotted ring. The strong coupling between neighboring unit-cells and the cancellation of magnetic fields are specific to the introduced slot MNM design and they are unavoidable. In the microstrip MNM design, the enclosing of the magnetic field lines do not occur since the magnetic field lines created by the current loops can only be found in the transverse plane so that they do not have any longitudinal components. Therefore, the rotating magnetic field response is not cancelled.

Moreover, since the slot MNM shows a distinct non-reciprocal gyrotropic response, it is important to characterize its properties such as the ellipticity and the Faraday rotation. The ellipticity, δ_F, is a measure of the polarization state of an electromagnetic wave and changes between -1 and 1. Basically, if $\delta_F = 1$, the wave is RCP, if it is $\delta_F = -1$ the wave is LCP and lastly, if $\delta_F = 0$, the wave is linearly polarized. The ellipticity and Faraday rotation are defined from [54] as

$$\delta_F = \frac{|T_{RCP}| - |T_{LCP}|}{|T_{RCP}| - |T_{LCP}|} \tag{3.3}$$

and

$$\theta_F = \frac{1}{2} \arctan\left(\frac{T_{LCP}}{T_{RCP}}\right), \tag{3.4}$$

respectively where T_{RCP} and T_{LCP} are transmission coefficients of RCP and LCP plane waves. T_{RCP} and T_{LCP} can be easily calculated from transmission coefficients of the linearly polarized plane waves as

$$\begin{bmatrix} T_{++} & T_{+-} \\ T_{-+} & T_{--} \end{bmatrix} = \frac{1}{2} \begin{bmatrix} T_{xx} + T_{yy} + i(T_{xy} - T_{yx}) & T_{xx} - T_{yy} - i(T_{xy} + T_{yx}) \\ T_{xx} - T_{yy} + i(T_{xy} + T_{yx}) & T_{xx} + T_{yy} - i(T_{xy} - T_{yx}). \end{bmatrix} \tag{3.5}$$

Thus, the ellipticity and the Faraday rotation angle of slot MNM are calculated and plotted in Fig. 3.11(a) and 3.11(b) based on (3.3) and (3.4), respectively. It is clear that for both x- and y-polarized plane wave incidence, the transmitted waves are elliptically polarized as opposed to magnetized ferrites where the transmitted waves are always linearly polarized since both RCP and LCP waves are transmitted with the same amplitude but with a different phase. This result is logical since the slot MNM prohibits the propagation of the LCP eigenstate so

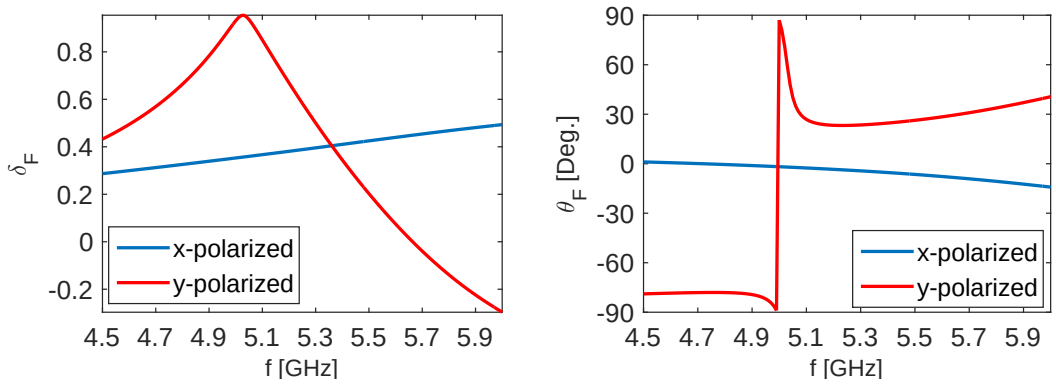

(a) (b)

Figure 3.11 (a) Ellipticity of the designed slot MNM. (b) Faraday rotation angle of the designed slot MNM.

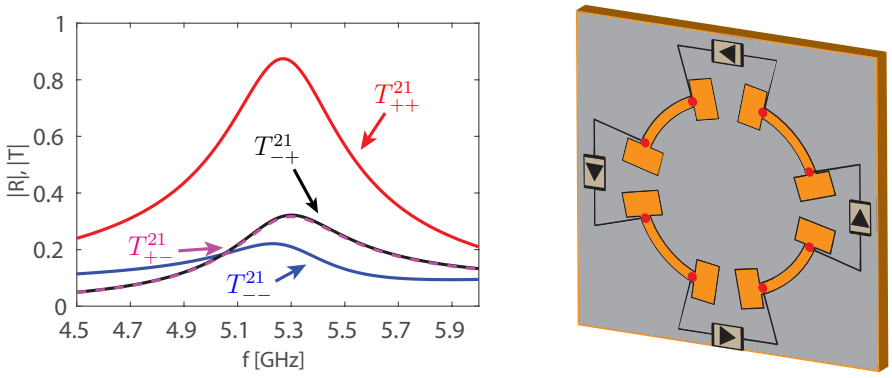

(a) (b)

Figure 3.12 (a) Transmission coefficients of the slot MNM under the RCP and the LCP plane wave illumination from $z > 0$. (b) An ideal symmetric slot MNM.

that the LCP wave should not pass through. However, as it can be seen from Fig. 3.11(a), the ellipticity is far from being one. This can be a clue for imperfectly matched unidirectional component or an effect that destroys the resonance. This statement can be validated by computing transmission coefficients of the slot MNM under RCP and LCP plane waves incidence. The results are shown in Fig. 3.12(a) where the RCP plane wave transmit through slot MNM and the LCP plane wave is reflected back since the unidirectional component prohibits the left-handed propagating eigenstate. Co-polarized transmission coefficients of the RCP plane wave are not one because of the imperfect matching and periodicity. In addition, there is a gyrotropic response in Fig. 3.12(a) where some part of the RCP plane wave transform to the LCP plane wave, because the structure does not have circular symmetry. Therefore, the cross-coupling between RCP and LCP plane wave occurs so that the transmitted field neither

pure RCP nor pure LCP plane waves. The problem can only be circumvented by designing a symmetric slot MNM as shown in Fig. 3.12(b) so that there will be no coupling between RCP and LCP plane waves and minimal transmission of LCP plane wave will be achieved. However, design of such a structure is extremely difficult due to the matching between the annular slotted ring and the big slot patch since length of the slot transmission lines is very short so that the matching can be achieved at the very high frequencies. In addition, the required impedance of the big slot patch for the matching is always out-of validity range of the slot line impedance formula. Lastly, the Faraday rotation angle in Fig. 3.11(b) is small for x-polarized plane wave incidence since the co-polarized transmission coefficient T_{xx}^{21} is very high comparing to the cross-polarized transmission coefficient T_{yx}^{21}. However, the Faraday rotation angle for y-polarized plane wave incidence reaches to 30° at the resonance.

Although a slot MNM design shown in Fig. 3.12(b) has not been realized, the symmetric non-reciprocal response under x- and y-polarized plane wave incidence could be realized by rotating unit-cell of the slot MNM by 45° as shown in Fig 3.2(a). It is important to note that the rotated slot MNM does still not have a circular symmetry for the RCP and the LCP plane waves. The reflection and transmission coefficients of $2D$ periodic array of the 45° rotated slot MNM is shown in Fig. 3.13(a). It is clear that the co-polarized reflection and transmission coefficients are same since both incident plane waves see exactly the same structure. In addition, unloaded case of the rotated slot MNM design poses already a gyrotropic response as can be seen in Fig.3.13(b) as opposed to the non-rotated case in Fig. 3.7(c) and 3.7(d). Although the rotated slot MNM shows a non-reciprocal response under x- and y-polarized plane wave incidence as can be seen from Fig. 3.13(c) and 3.13(d),there is a 90° phase difference between cross-polarized components of transmission matrix T_{xy}^{21} and T_{yx}^{12} as opposed to artificial ferrite response. Thus, the rotated slot MNM has also a non-reciprocal gyrotropic response but it is not the same as magnetized ferrites. It is very straightforward to see why the artificial ferrite behaviour of the slot MNM structure is destroyed by the rotation because when the structure is rotated by angle θ the transmission coefficients of the rotated structure can be written in terms of non-rotated coefficients as

$$\bar{\bar{T}}^{rot} = \bar{\bar{R}}(\theta) \cdot \bar{\bar{T}}^{nrot} \cdot \bar{\bar{R}}^{-1}(\theta), \tag{3.6}$$

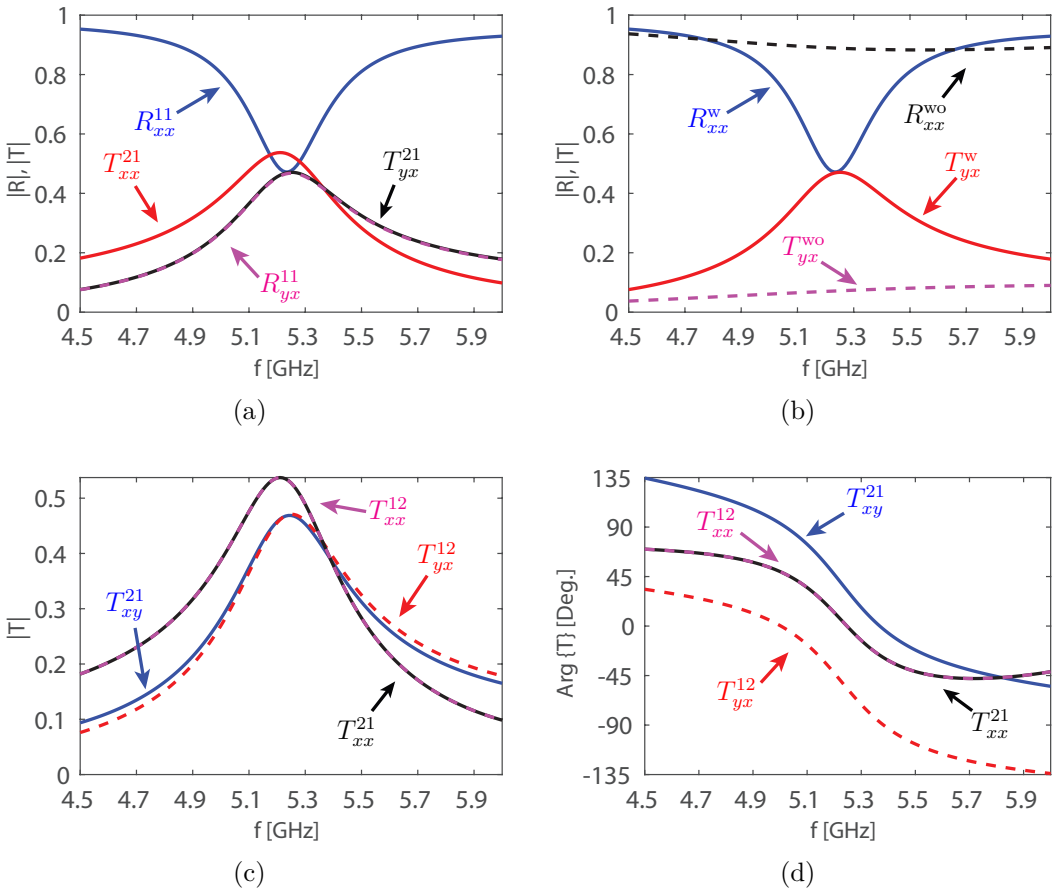

Figure 3.13 (a) Reflection and transmission coefficients of the 45° rotated slot MNM under x-polarized plane wave illumination from $z > 0$. (b) Comparison of reflection and transmission coefficients of the unidirectional component loaded (w superscript) and the unloaded structure (wo superscript) under plane wave illumination. Non-reciprocity of the 45° rotated slot MNM : Comparison of the transmission coefficients when the structure is excited from $z > 0$ and $z < 0$ in time-reversal schema. (c) Magnitude. (d) Phase.

where $\bar{\bar{T}}^{rot}$ is transmission dyadic of the 45° rotated slot MNM, $\bar{\bar{T}}^{nrot}$ is transmission dyadic of non-rotated slot MNM and $\bar{\bar{R}}(\theta)$ is the rotation dyadic is defined as

$$\bar{\bar{R}}(\theta) = \begin{bmatrix} \cos\theta & \sin\theta \\ -\sin\theta & \cos\theta \end{bmatrix} \tag{3.7}$$

Thus, transmission coefficients of the rotated slot MNM have components both from co-and cross-polarized transmission coefficients of non-rotated slot MNM. Since the co-polarized transmission coefficients are reciprocal, the summation of it with the cross-polarized transmission coefficients destroy the ferrite-like non-reciprocal response of the non-rotated slot MNM. Therefore, when the unit-cell is rotated, according to nature of co-polarized transmis-

sion coefficients of the non-rotated slot MNM, the non-reciprocity of the rotated slot MNM changes, but it is always non-reciprocal. Lastly, in Fig. 3.14(a) and 3.14(b), the ellipticity and the Faraday rotation of the rotated slot MNM is plotted. Since the rotated slot MNM does not pose symmetry for RCP and LCP waves, it is clear that the transmitted and reflected fields cannot be purely circularly polarized as seen in Fig. 3.14(a).

In conclusion, a transparent slot based MNM is designed by modifying the Babinet complementary of the microstrip MNM. The structure has a non-reciprocal gyrotropic response under x- and y-polarized plane wave incidence like magnetized ferrites but, this structure is not the exact replica of magnetized ferrites since the structure has asymmetry for circularly polarized waves. Moreover, the gyrotropic response of the structure is identified from its reflection and transmission coefficients. As it can be seen from the time evolution of the magnetic field lines, the coupling of neighboring unit-cells and the big slot patch is negatively affecting the rotating magnetic dipole moment response. Therefore, the resonance has a low quality factor compared to microstrip MNMs. Due to the aforementioned difficulties, the introduced transparent MNM is not the most effective design to replace ferrites, however it still has non-reciprocal gyrotropic response and could be utilized for many applications that requires gyrotropy. Lastly, even if the ideal transparent MNM can be designed, it always poses a non-negligible reflectance, not wanted for industrial applications, due to the subwavelength thickness of the structure. Thus, it would be a very important step to design a reflection-less transparent MNMs for practical applications which will be the topic of the next chapter.

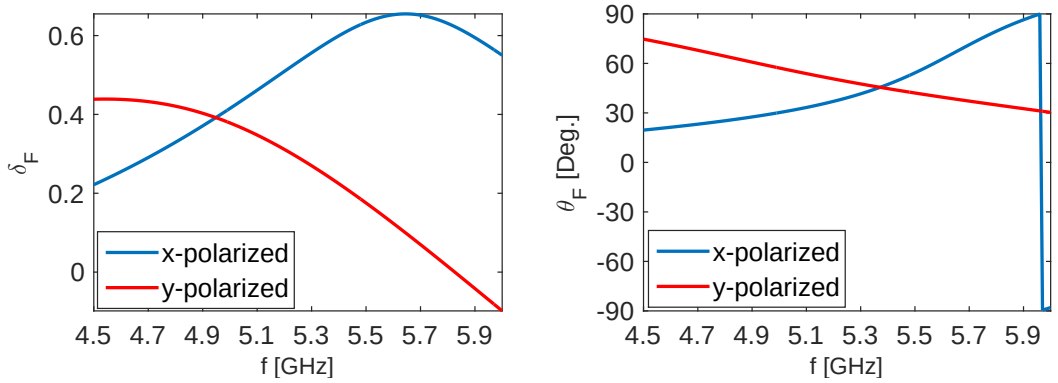

(a) (b)

Figure 3.14 (a) Ellipticity of the 45° rotated slot MNM. (b) Faraday rotation angle of the 45° slot MNM.

3.2 Physical Explanation of the Non-Reciprocity of Transparent Slot MNMs

Non-reciprocal gyrotropic response of the slot MNMs is shown in the previous section. However, the reasons why the non-reciprocity occurs from theoretical point of view has not been discussed, yet. Thus, first the unloaded annular slotted ring structure shown in Fig. 3.15(a) where it is assumed that $\psi \simeq 0$, the origin is located at $z = h/2$ is considered. Since the following explanations of the non-reciprocity will be based on a simple physical picture, the matching is assumed to be satisfied without big slots. When there is no external excitation, the annular slotted ring structure poses two counter-propagating eigenstates, namely right-handed and left-handed as seen in Fig. 3.15(a). These counter-propagating eigenstates can be either in the form of current or voltage wave around the slot. Thus, any excitation that induce a current wave around annular slotted ring can be expanded into the summation of those two eigenstates as

$$I(\phi) = a^{+} e^{-j\beta R\phi} + a^{-} e^{j\beta R\phi}, \tag{3.8}$$

where R is the average radius of annular slotted ring, a^{+} and a^{-} are the expansion coefficients of the right-handed and the left-handed eigenstates, respectively. Simply, induced current distribution can be written in terms of the incident field as $I^{ind} \sim \frac{1}{Z_0} E_{\rho}^{inc}|_{z=h/2}$, where Z_0 is characteristic impedance of the annular slotted ring. Therefore, the induced current around annular slotted ring under x- and y-polarized plane wave illumination can be expanded into

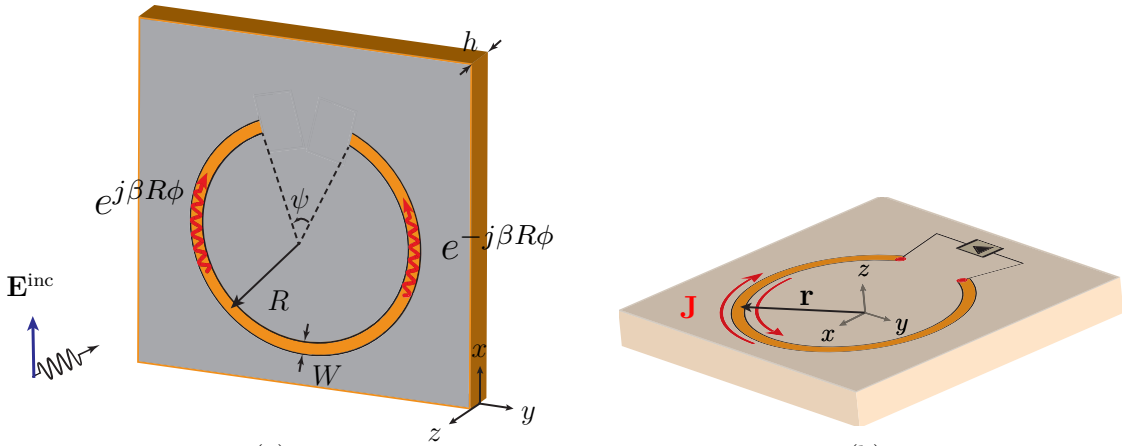

Figure 3.15 (a) Counter-propagating eigenstates of the unloaded slot MNM. (b) Transverse current distribution over PEC plane of the slot MNM with the observation vector $\mathbf{r}$.

the propagating eigenstates as

$$\frac{1}{Z_0}\cos\phi\, e^{jk\frac{h}{2}} = a_x^+ e^{-j\beta R\phi} + a_x^- e^{j\beta R\phi}, \tag{3.9}$$

$$\frac{1}{Z_0}\sin\phi\, e^{jk\frac{h}{2}} = a_y^+ e^{-j\beta R\phi} + a_y^- e^{j\beta R\phi}, \tag{3.10}$$

, respectively. In (3.9) and (3.10), a_x and a_y is used to identify the coupling coefficient belonging to either x- or y-polarized plane wave incidence. The expansion coefficients a_x and a_y can be easily found by exploiting orthogonality of the eigenfunctions so that both sides of (3.9) and (3.10) multiplied with their conjugates and integrated from 0 to 2π since $\theta \simeq 0$. Thus, the expansion coefficients can simply be calculated as

$$\begin{aligned} a_x^+ &= -j\frac{\beta}{Z_0} R \frac{e^{j2\pi\beta R}-1}{\beta^2R^2-1}\, e^{jk\frac{h}{2}}, \qquad & a_x^+ &= -a_x^-, \\ a_y^+ &= \frac{1}{Z_0}\frac{e^{j2\pi\beta R-1}}{\beta^2R^2-1}\, e^{jk\frac{h}{2}}, & a_y^+ &= a_y^-. \end{aligned} \tag{3.11}$$

In order to break the time-reversal symmetry, an unidirectional component is used to block the propagation of the left-handed eigenstates so that when the unidirectional component is loaded into the annular slotted ring structure, all the expansion coefficients belong to the left-handed propagating states, a^- in (3.11), will be zero.

Since the slot MNM shows a rotating magnetic dipole response, it should be characterized with a magnetic dipole moment. Magnetic moment of the slot MNM can be easily calculated based on the multipole expansion of electromagnetic fields [48] as

$$\mathbf{m} = \frac{1}{2}\int_V \mathbf{r}\times\mathbf{J}dV, \tag{3.12}$$

where $\mathbf{r} = R\mathbf{e}_\rho + \frac{t}{2}\mathbf{e_z}$ as shown in Fig. 3.15(b). Thus, for the current distribution $\mathbf{J} = [I(\phi)\delta(z+\frac{t}{2})\delta(\rho-R+\frac{W}{2}) - I(\phi)\delta(z+\frac{h}{2})\delta(\rho-R-\frac{W}{2})]\mathbf{e}_\phi$ around slot MNM as in Fig. 3.15(b), the magnetic dipole moment of the slot MNM can be found as

$$\mathbf{m}_t = -\frac{Wt}{4}\int_0^{2\pi} I(\phi)\mathbf{e}_\rho d\phi, \tag{3.13}$$

$$m_z = 2WR\int_0^{2\pi} I(\phi)d\phi. \tag{3.14}$$

In (3.14), the longitudinal component of the magnetic dipole moment m_z is evident due to the current loop around the annular slotted ring in Fig. 3.4(a). However, the effect of the longitudinal component of the magnetic dipole moment will be negligible at the far-field

due to radiation pattern of the dipole. Since throughout the rest of the thesis only far-field response of slot MNMs is considered, effect of longitudinal component of the magnetic dipole moment is neglected. However, for any design that utilizes near-filed response of the slot MNMs, the longitudinal magnetic dipole moment contribution have to be considered.

Magnetic dipole moment of the ideal slot MNM under x- and y-polarized plane wave incidence can be calculated by inserting (3.11) into (3.13) when a^- is zero as

$$\begin{aligned} m_x &= -\frac{Wt}{8Z_0}|a_x^+|^2\, e^{jk\frac{t}{2}}, & m_y &= \frac{Wt}{8Z_0}a_x^+(a_y^+)^*\, e^{jk\frac{h}{2}}, \\ m_x &= -\frac{Wt}{8Z_0}a_y^+(a_x^+)^*\, e^{jk\frac{t}{2}}, & m_y &= \frac{Wt}{8Z_0}|a_y^+|^2\, e^{jk\frac{h}{2}}, \end{aligned} \tag{3.15}$$

respectively where $(.)^*$ is the conjugate operator. Thus, at the traveling wave resonance magnetic dipole moment of the slot MNM under either x- or y-polarized plane wave illumination shows a right-handed nature so that from (3.11), $a_x^+ = -j\beta R a_y^+$ yields

$$\mathbf{m} = \frac{Wt}{8Z_0}e^{jk\frac{h}{2}}(\mathbf{e_x} - j\mathbf{e_y}), \tag{3.16}$$

since close to the resonance frequency $\beta R \simeq 1$. Thus, time domain expression of magnetic dipole moment of the slot MNM can be written as

$$\mathcal{M}(t) = \frac{Wt}{8Z_0}(\cos(\omega t)\mathbf{e_x} + \sin(\omega t)\mathbf{e_y}), \tag{3.17}$$

where the right-handed rotation of the magnetic dipole moment of the slot MNM is evident. In addition, the calculated magnetic dipole moments of the ideal slot MNM can be related with its surface susceptibility tensor by using the relations $\mathbf{m} = \bar{\bar{\chi}} \cdot \mathbf{H}^{inc}$ and $\mathbf{H} = \frac{1}{\eta}\mathbf{n} \times \mathbf{E}$ as

$$\begin{aligned} \chi_{xx} &= -\eta\frac{Wt}{8Z_0}|a_x^+|^2\, e^{jk\frac{t}{2}}, & \chi_{xy} &= \eta\frac{Wt}{8Z_0}a_x^+(a_y^+)^*\, e^{jk\frac{t}{2}}, \\ \chi_{xy} &= \eta\frac{Wt}{8Z_0}a_y^+(a_x^+)^*\, e^{jk\frac{t}{2}}, & \chi_{yy} &= -\eta\frac{Wt}{8Z_0}|a_y^+|^2\, e^{jk\frac{t}{2}}, \end{aligned} \tag{3.18}$$

where η is characteristic impedance of the medium that the ideal slot MNM is placed. Thus, the ideal slot MNM is homogenized in terms of its plane wave coupling coefficients. Such a characterization can also be done for magnetized ferrites as in (2.2) where the gyrotropy and non-reciprocity is evident. The microscopic picture of the slot MNM provides that the slot MNM has a gyrotropic response due to the cross-components in (3.18). In addition, since $a_y^+(a_x^+)^* = -a_x^+(a_y^+)^*$ from (3.11), surface susceptibility tensor of the ideal slot MNM is not Hermitian so that $\bar{\bar{\chi}} \neq \bar{\bar{\chi}}^T$. This observation shows that the ideal slot MNM has non-

reciprocal response. In addition, since $\chi_{xy} = -\chi_{yx}$ from (3.18) according to relation between expansion coefficients (3.11), the ideal slot MNM shows a magnetized ferrite behaviour. Further observations on (3.18) show that the diagonal components of the susceptibility tensor is symmetric when only the coupling coefficients under x- and y-polarized plane wave incidence, a_x^+ and a_y^+, are equal. This supports the observation done in the previous chapter so that the eigenstates of the designed slot MNM are elliptically polarized due to the asymmetry of the structure.

3.3 Characterization of The Transparent Slot MNMs

Metamaterials can always be characterized with its homogenized parameters if periodicity of the metamaterial array is less than $\lambda_g/2$. Although the $\lambda_g/2$ limit is the necessary condition, it may not be sufficient to truly characterize the metamaterials, since spatial dispersion effects may appear. Although the homogenization of metamaterials in mesoscopic regime is well developed in [55], the parameters could not characterize the physical properties correctly. Thus, as discussed in previous chapters, it is important to design a functional metamaterials rather than exact replicas of natural materials. Metasurfaces could also be characterized with its surface parameters such as its electric and magnetic susceptibilities or electric-magnetic and magnetic-electric coupling coefficients. Since the characterization of metasurfaces is based on boundary conditions as it will be seen later in this section, it may not provide correct microscopic picture of the metasurface. However, it is a reliable physical tool to understand electromagnetic response of a metasurfaces.

3.3.1 Full Surface Parameter Extraction of the Slot MNM

Any media that has a thickness $h \ll \lambda$ could be electromagnetically classified as a surface and can be characterized through the boundary conditions. In general, such a surface could be bi-anisotropic where electric and magnetic currents present due to either incident electric or magnetic fields or both. Thus, the boundary conditions on a bi-anisotropic surface located at $z = 0$ and embedded between two different media with characteristic impedances η_1 and η_2 can be written as

$$-\mathbf{n} \times (\mathbf{E}_2 - \mathbf{E}_1) = \bar{\bar{\mathbf{\Theta}}}_s \cdot \mathbf{E}|_{z=0} + \bar{\bar{\mathbf{Z}}}_s \cdot \mathbf{H}|_{z=0} \tag{3.19}$$

$$\mathbf{n} \times (\mathbf{H}_2 - \mathbf{H}_1) = \bar{\bar{\mathbf{Y}}}_s \cdot \mathbf{E}|_{z=0} + \bar{\bar{\mathbf{\Psi}}}_s \cdot \mathbf{H}|_{z=0}, \tag{3.20}$$

where $\mathbf{n}$ unit normal vector of the surface, 1 and 2 sub-indexes corresponds to the $z = 0^-$ and $z = 0^+$, respectively. In (3.19), $\bar{\bar{\mathbf{\Psi}}}_s$ and $\bar{\bar{\mathbf{Z}}}_s$ corresponds to magneto-electric surface parameters

and surface impedance. In addition in (3.20), $\bar{\bar{\mathbf{\Theta}}}_s$ and $\bar{\bar{\mathbf{Y}}}_s$ corresponds to magneto-electric surface parameter and surface admittance, respectively. Due to discontinuity of the boundary conditions, the right hand side of the (3.19) is called surface magnetic current density $\mathbf{M}_s$ and the right hand side of the 3.20 is called surface electric current density $\mathbf{J}_s$. The tensors $\bar{\bar{\mathbf{\Psi}}}_s$, $\bar{\bar{\mathbf{Z}}}_s$, $\bar{\bar{\mathbf{\Theta}}}_s$ and $\bar{\bar{\mathbf{Y}}}_s$ are the macroscopic parameters that electromagnetically characterize any bi-anisotropic surface and related to the microscopic surface parameters, polarizabilities, as $\bar{\bar{\mathbf{Y}}}_s = j\omega\alpha_{ee}$, $\bar{\bar{\mathbf{\Theta}}}_s = j\omega\alpha_{me}$, $\bar{\bar{\mathbf{\Psi}}}_s = j\omega\alpha_{em}$, $\bar{\bar{\mathbf{Z}}}_s = j\omega\alpha_{mm}$ [36]. Thus, for any surface there are 16 unknown parameters that should be found by solving 16 linearly independent equations. These 16 equations can be derived by using the reflection and transmission dyadics of the surface under x- and y-polarized normally propagating plane wave incidence from region 1 or 2, namely $\bar{\bar{R}}^{11}$, $\bar{\bar{R}}^{22}$, $\bar{\bar{T}}^{21}$ and $\bar{\bar{T}}^{12}$.

For the derivation of 16 sets of equations, (3.19) can be written as

$$-(\mathbf{E}_2 - \mathbf{E}_1) = \mathbf{n} \times \bar{\bar{\mathbf{\Theta}}}_s \cdot \mathbf{E}_{z=0} + \mathbf{n} \times \bar{\bar{\mathbf{Z}}}_s \cdot \mathbf{H}_{z=0} \tag{3.21}$$

$$\tag{3.22}$$

by multiplying both sides with $\mathbf{n}$. The equations (3.19) and (3.20) can be arranged by using the dyadic identity $\bar{\bar{\mathbf{a}}} \cdot (\mathbf{b} \times \mathbf{c}) = -(\bar{\bar{\mathbf{a}}} \times \mathbf{c}) \cdot \mathbf{b}$ as

$$-(\mathbf{E}_2 - \mathbf{E}_1) = \mathbf{n} \times \bar{\bar{\mathbf{\Theta}}}_s \cdot \mathbf{E}_{z=0} - (\mathbf{n} \times \bar{\bar{\mathbf{Z}}}_s \times \mathbf{n}) \cdot (\mathbf{n} \times \mathbf{H}_{z=0}) \tag{3.23}$$

$$\mathbf{n} \times (\mathbf{H}_2 - \mathbf{H}_1) = \bar{\bar{\mathbf{Y}}}_s \cdot \mathbf{E}|_{z=0} - (\bar{\bar{\mathbf{\Psi}}}_s \times \mathbf{n}) \cdot \mathbf{H}_{z=0}. \tag{3.24}$$

Thus, (3.19) and (3.20) written in terms of $\mathbf{E}$ and $\mathbf{n} \times \mathbf{H}$. In addition, electric and magnetic fields at $z = 0$ can be written as

$$\begin{aligned} \mathbf{H}|_{z=0} &= \frac{1}{2}\left(\mathbf{H}_1 + \mathbf{H}_2\right), \\ \mathbf{E}|_{z=0} &= \frac{1}{2}\left(\mathbf{E}_1 + \mathbf{E}_2\right) \end{aligned} \tag{3.25}$$

by averaging the fields at both sides of the surface due to its subwavelength thickness. By using the transmission line analogy, the electric field $\mathbf{E}$ can be replaced with the voltage $\mathbf{V}$ and the cross product of the magnetic field $\mathbf{n} \times \mathbf{H}$ can be replaced with $\mathbf{I}$. Thus, by using (3.25), (3.23) and (3.24) can be written as

$$\begin{aligned} \mathbf{V}_1 - \mathbf{V}_2 &= \frac{\mathbf{n} \times \bar{\bar{\mathbf{\Theta}}}_s}{2} \cdot (\mathbf{V}_1 + \mathbf{V}_2) - \frac{(\mathbf{n} \times \bar{\bar{\mathbf{Z}}}_s \times \mathbf{n})}{2} \cdot (\mathbf{I}_1 + \mathbf{I}_2) \\ \mathbf{I}_2 - \mathbf{I}_1 &= \frac{\bar{\bar{\mathbf{Y}}}_s}{2} \cdot (\mathbf{V}_1 + \mathbf{V}_2) - \frac{\bar{\bar{\mathbf{\Psi}}}_s \times \mathbf{n}}{2} \cdot (\mathbf{I}_1 + \mathbf{I}_2). \end{aligned} \tag{3.26}$$

The voltages $\mathbf{V}_1$, $\mathbf{V}_2$ and current $\mathbf{I}_1$, $\mathbf{I}_2$ vectors can be related to the reflection and transmission dyadics of the surface by using the identity $\mathbf{E} = \eta \mathbf{n} \times \mathbf{H}$ as

$$\begin{aligned} \mathbf{V}_1 = \bar{\bar{I}} + \bar{\bar{R}}^{11} \quad \mathbf{I}_1 = \frac{\bar{\bar{I}} - \bar{\bar{R}}^{11}}{\eta_1} \cdot {\mathbf{E_1}}^{inc}, \\ \mathbf{V}_2 = \bar{\bar{T}}^{21} \quad \mathbf{I}_2 = \frac{\bar{\bar{T}}^{21}}{\eta_2} \cdot {\mathbf{E_1}}^{inc}, \end{aligned} \tag{3.27}$$

for plane waves incident from region 1, and

$$\begin{aligned} \mathbf{V}_1 = \bar{\bar{T}}^{12} \quad \mathbf{I}_1 = \frac{\bar{\bar{T}}^{12}}{\eta_1}, \cdot {\mathbf{E_2}}^{inc} \\ \mathbf{V}_2 = \bar{\bar{I}} + \bar{\bar{R}}^{22} \quad \mathbf{I}_2 = \frac{-\bar{\bar{I}} + \bar{\bar{R}}^{22}}{\eta_2} \cdot {\mathbf{E_2}}^{inc}, \end{aligned} \tag{3.28}$$

for plane waves incident from region 2. In the above equations, ${\mathbf{E_m}}^{inc}$ is electric field vector of the normally propagating plane wave incident from region m, $\bar{\bar{R}}^{mm}$ is the reflection dyadic for plane waves excited from region m and $\bar{\bar{T}}^{mn}$ is the transmission dyadic for plane waves excited from region n and propagating through region m. In general, the reflection and transmission dyadic is written under x- and y-polarized normally propagating plane wave incidence as

$$\bar{\bar{S}}^{mn} = \begin{bmatrix} S_{xx}^{mn} & S_{xy}^{mn} \\ S_{yx}^{mn} & S_{yy}^{mn} \end{bmatrix}, \tag{3.29}$$

where S represent either R or T. Since each dyadic component has 4 known quantity, they constitute total of 16 quantity which can be used to find the 16 unknown surface parameter. Thus, by substituting (3.27) and (3.28) in (3.26) yields

$$\begin{bmatrix} \dfrac{\bar{\bar{T}}^{21}}{\eta_2} - \dfrac{\bar{\bar{I}} - \bar{\bar{R}}^{11}}{\eta_1} \\ \bar{\bar{I}} + \bar{\bar{R}}^{11} - \bar{\bar{T}}^{21} \end{bmatrix} = \frac{1}{2} \begin{bmatrix} \bar{\bar{\mathbf{Y}}}_s & \bar{\bar{\mathbf{\Psi}}}_s \times \mathbf{n} \\ \mathbf{n} \times \bar{\bar{\mathbf{\Theta}}}_s & \mathbf{n} \times \bar{\bar{\mathbf{Z}}}_s \times \mathbf{n} \end{bmatrix} \begin{bmatrix} \bar{\bar{T}}^{21} + \bar{\bar{I}} + \bar{\bar{R}}^{11} \\ \dfrac{\bar{\bar{R}}^{11} - \bar{\bar{I}}}{\eta_1} - \dfrac{\bar{\bar{T}}^{21}}{\eta_2} \end{bmatrix}, \tag{3.30}$$

$$\begin{bmatrix} \dfrac{\bar{\bar{R}}^{22} - \bar{\bar{I}}}{\eta_2} - \dfrac{\bar{\bar{T}}^{12}}{\eta_1} \\ \bar{\bar{T}}^{12} - \bar{\bar{I}} - \bar{\bar{R}}^{22} \end{bmatrix} = \frac{1}{2} \begin{bmatrix} \bar{\bar{\mathbf{Y}}}_s & \bar{\bar{\mathbf{\Psi}}}_s \times \mathbf{n} \\ \mathbf{n} \times \bar{\bar{\mathbf{\Theta}}}_s \times & \mathbf{n} \times \bar{\bar{\mathbf{Z}}}_s \times \mathbf{n} \end{bmatrix} \begin{bmatrix} \bar{\bar{T}}^{12} + \bar{\bar{I}} + \bar{\bar{R}}^{22} \\ \dfrac{\bar{\bar{I}} - \bar{\bar{R}}^{22}}{\eta_2} - \dfrac{\bar{\bar{T}}^{12}}{\eta_1} \end{bmatrix}, \tag{3.31}$$

respectively. Thus, the two matrix system given in (3.30) and (3.31) can be combined to form 16 equation for 16 surface parameters and solved for surface parameters as

$$\begin{bmatrix} \bar{\bar{\mathbf{Y}}}_s & -\bar{\bar{\mathbf{\Psi}}}_s \times \mathbf{n} \\ -\bar{\bar{\mathbf{\Psi}}}_s \times \mathbf{n} & \mathbf{n} \times \bar{\bar{\mathbf{Z}}}_s \times \mathbf{n} \end{bmatrix} = 2 \begin{bmatrix} \dfrac{\bar{\bar{T}}^{21}}{\eta_2} - \dfrac{\bar{\bar{I}} - \bar{\bar{R}}^{11}}{\eta_1} & \dfrac{\bar{\bar{R}}^{22} - \bar{\bar{I}}}{\eta_2} - \dfrac{\bar{\bar{T}}^{12}}{\eta_1} \\ \bar{\bar{I}} + \bar{\bar{R}}^{11} - \bar{\bar{T}}^{21} & \bar{\bar{T}}^{12} - \bar{\bar{I}} - \bar{\bar{R}}^{22} \end{bmatrix} \cdot \begin{bmatrix} \bar{\bar{T}}^{21} + \bar{\bar{I}} + \bar{\bar{R}}^{11} & \bar{\bar{T}}^{12} + \bar{\bar{I}} + \bar{\bar{R}}^{22} \\ \dfrac{\bar{\bar{R}}^{11} - \bar{\bar{I}}}{\eta_1} - \dfrac{\bar{\bar{T}}^{21}}{\eta_2} & \dfrac{\bar{\bar{I}} - \bar{\bar{R}}^{22}}{\eta_2} - \dfrac{\bar{\bar{T}}^{12}}{\eta_1} \end{bmatrix}^{-1} . \tag{3.32}$$

The reflection and transmission dyadics of a surface can be determined experimentally, analytically or numerically so that by using (3.32), the electromagnetic characterization of a surface can be done. In this thesis, the numerical solutions of slot MNM are employed by using HFSS in order to characterize the single-layer structure since any attempt to analytically model the slot MNM structure based on the analysis method developed in [7] did not give any accurate results. By employing HFSS solution of the slot MNM with the design parameters given in Table 3.1, its surface parameters are computed and presented in Fig. 3.16. As can be seen from the figures, there is no resonance behaviour at 5.3 GHz although there is a non-reciprocal gyrotropic response. This can be attributed to the effect of neighboring unit-cells, the big slot termination, or elliptical nature of the rotating dipole moments. It is clear that these effects are destroying the resonance behaviour, moreover as seen from the magnetic field distribution of the slot MNM in Fig. 3.10, the rotating magnetic dipole moment is non-uniform. Thus, the travelling wave resonance may fade away. In addition, the whole surface parameters have a real part which should be zero for ideal lossless materials [36], however since the unidirectional component blocks the propagation of the left-handed eigenstates, the power that pass through the slot MNM decreases. Thus, slot MNMs has inherent loss which is evident from the non-zero real part of the surface parameters in Fig. 3.16.

As seen from Fig. 3.16, the strongest surface parameter that characterizes the slot MNM is the surface impedance tensor. Indeed rest of the parameters are so small compared to surface impedance tensor and can be neglected. This behaviour is expected since the slot MNM shows a rotating magnetic dipole moment response, i.e. a magnetic current. In addition, according to the non-reciprocity condition (2.3), all the surface parameters shown in Fig. 3.16 shows non-reciprocal behaviour, evident from rotating magnetic dipole moment of the slot MNM, since $Z_{xy} \neq Z_{yx}$. Note that as magnetized ferrites, the surface impedance of the slot MNM satisfies the relation $Z_{xy} = -Z_{yx}$ where this justifies that the designed slot MNM is an artificial ferrite.

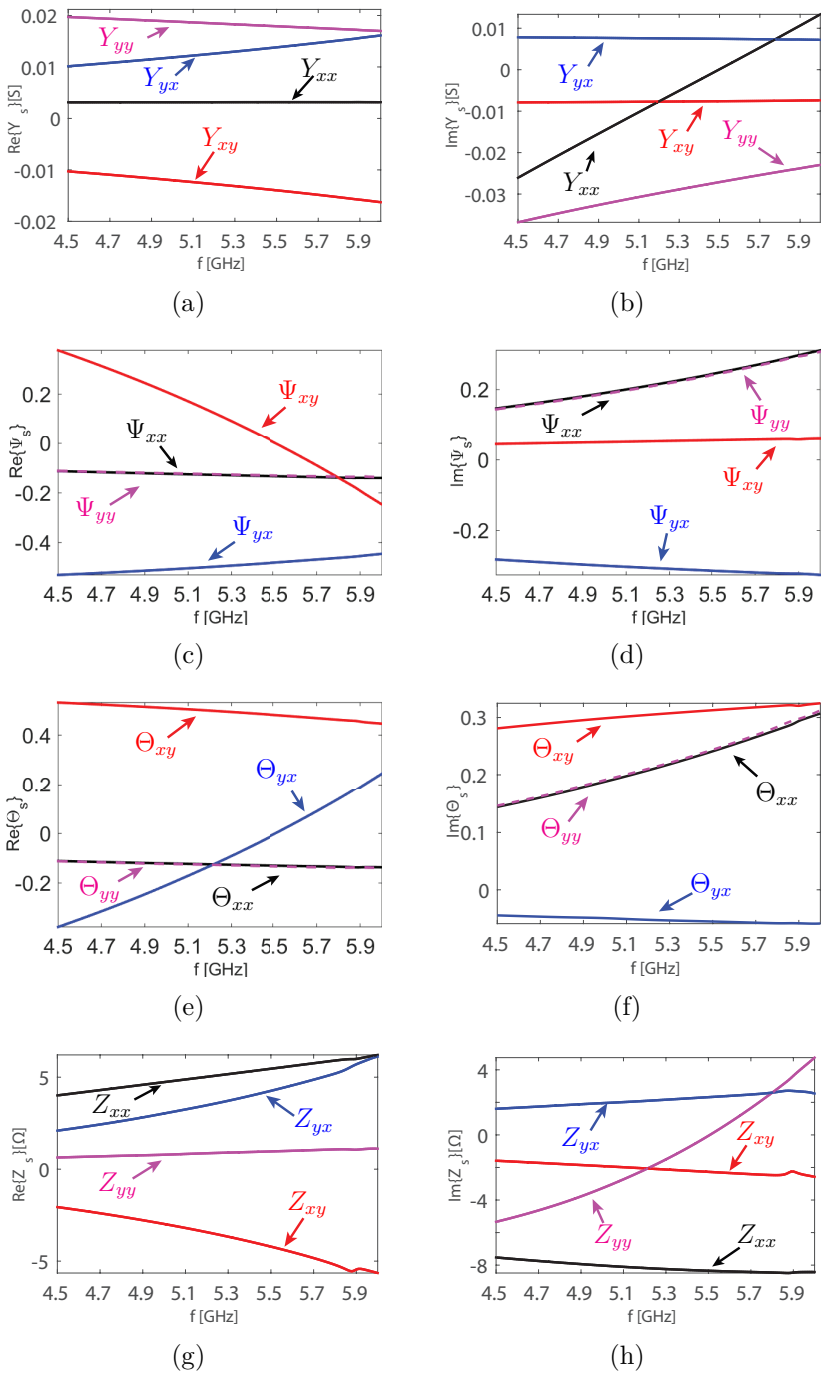

Figure 3.16 Surface parameters of the slot MNM resonant at 5.3 GHz. (a) Real part of the surface admittance. (b) Imaginary part of the surface admittance. (c) Real part of the electro-magnetic surface parameter. (d) Imaginary part of the electro-magnetic surface parameter. (e) Real part of the magneto-electric surface parameters. (f) Imaginary part of the magneto-electric surface parameters. (g) Real part of the surface impedance. (h) Imaginary part of the surface impedance.

3.3.2 Basic Transmission-Line Model for Transparent Slot MNMs

The surface parameters are derived by using the transmission line analogy in the previous section and the slot MNMs are characterized. The surface parameters is not only useful to understand physics of the structure, but they can also be used to analytically compute electromagnetic response of multi-layer slot MNMs. Thus, in this section, basic transmission model of the slot MNMs will be provided based on transmission line analogy of the slot MNMs under normally incident plane wave illumination.

Although slot MNMs are bi-anisotropic metasurfaces as can be seen from Fig. 3.16, amplitude of the surface impedance $\bar{\bar{\mathbf{Z}}}_s$ is much larger than the other surface parameter since the slot MNMs show rotating magnetic dipole response. Thus, it would be logical to neglect the contribution of the surface parameters except the surface impedance in order to characterize the slot MNMs. If such an assumption is made, the slot MNM can be replaced with its network model as a transmission-line element. Thus, the slot MNM is a 4-port impedance element that serially connects the region 1 and region 2 as seen in Fig. 3.17 where the TM^z and TE^z plane waves propagating in the normal direction are modelled as the voltage $\mathbf{V}$ and the current $\mathbf{I}$ vectors of the 4-port transmission-line. Since the only unknown parameter is the surface impedance with 4 quantity, 4 equation is needed to be derived for the unique solution. Therefore, the surface impedance of any surface embedded between mediums with characteristic impedances η_1 and η_2 can be derived starting from boundary conditions as done in previous section where $\bar{\bar{\mathbf{Y}}}_s = \bar{\bar{0}}$, $\bar{\bar{\mathbf{\Theta}}}_s = \bar{\bar{0}}$ and $\bar{\bar{\mathbf{\Psi}}}_s = \bar{\bar{0}}$ in (3.30) yields

$$\begin{bmatrix} \dfrac{\bar{\bar{T}}^{21}}{\eta_2} - \dfrac{\bar{\bar{I}} - \bar{\bar{R}}^{11}}{\eta_1} \\ \bar{\bar{I}} + \bar{\bar{R}}^{11} - \bar{\bar{T}}^{21} \end{bmatrix} = \frac{1}{2} \begin{bmatrix} \bar{\bar{0}} & \bar{\bar{0}} \\ \bar{\bar{\mathbf{0}}} & \mathbf{n} \times \bar{\bar{\mathbf{Z}}}_s \times \mathbf{n} \end{bmatrix} \begin{bmatrix} \bar{\bar{T}}^{21} + \bar{\bar{I}} + \bar{\bar{R}}^{11} \\ \dfrac{\bar{\bar{R}}^{11} - \bar{\bar{I}}}{\eta_1} - \dfrac{\bar{\bar{T}}^{21}}{\eta_2} \end{bmatrix}, \tag{3.33}$$

for plane waves excited from region 1. Thus, by using the first row of (3.33), the surface impedance can be found as

$$\mathbf{n} \times \bar{\bar{\mathbf{Z}}}_s \times \mathbf{n} = (\eta_1 + \eta_2)\bar{\bar{I}} - 2\eta_2(\bar{\bar{T}}^{21})^{-1}. \tag{3.34}$$

The same derivation can be done for any of $\bar{\bar{R}}^{11}$, $\bar{\bar{R}}^{22}$ and $\bar{\bar{T}}^{12}$ so that the surface impedance of a surface is same due to the uniqueness of the boundary conditions. Moreover the transfer

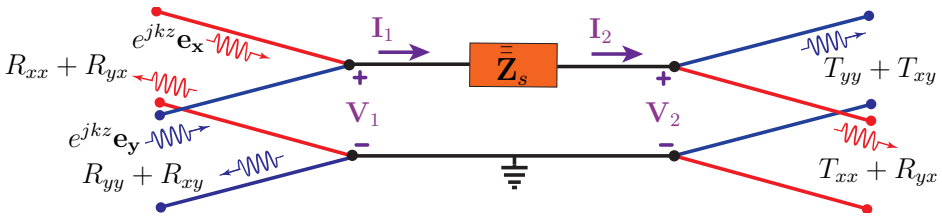

Figure 3.17 Network model for a Slot MNM.

matrix, namely the ABCD matrix, of the surface can be easily derived from (3.33) as

$$\begin{bmatrix} \mathbf{V_1} \\ \mathbf{I_1} \end{bmatrix} = \begin{bmatrix} \bar{\bar{I}} & \mathbf{n} \times \bar{\bar{\mathbf{Z}}}_s \times \mathbf{n} \\ \bar{\bar{0}} & \bar{\bar{I}} \end{bmatrix} \begin{bmatrix} \mathbf{V_2} \\ \mathbf{I_2} \end{bmatrix}, \tag{3.35}$$

by using the definitions (3.27). The transfer matrix of a surface is useful to model cascaded structures as will be seen in the next chapter.

Thus, transmission dyadic of the designed slot MNM with the parameters given in Table 3.1 is used to extract its surface impedance parameters as seen in Fig. 3.18(a) and 3.18(b) where the artificial ferrite response is evident since $Z_{xy} = -Z_{yx}$, and real part of the surface impedances implies the loss. In addition, in Fig. 3.18(c) and 3.18(d), the surface impedance of 45° rotated slot MNM with parameters given in Table 3.1 is plotted in order to see effect of the rotation on the surface impedance. As can be seen from Fig. 3.13, once the slot MNM is rotated 45° around $+\mathbf{e_z}$ axis, the co-polarized component of reflection and transmission dyadic are same since the structure is symmetric under x- and y-polarized plane wave incidence, the same observation can clearly be seen from Fig. 3.18(c) and 3.18(d) where the co-polarized components of the surface impedance are same. In addition as stated before rotation of the structure is destroying the pure artificial ferrite response since $Z_{xy} \neq -Z_{yx}$ as can be seen from Fig. 3.18(d) but the rotated slot MNM is still has non-reciprocity. Thus, the slot MNM can macroscopically be characterized with its surface impedance dyadic, and transmission-line model of the structure could be used for the modeling purposes.

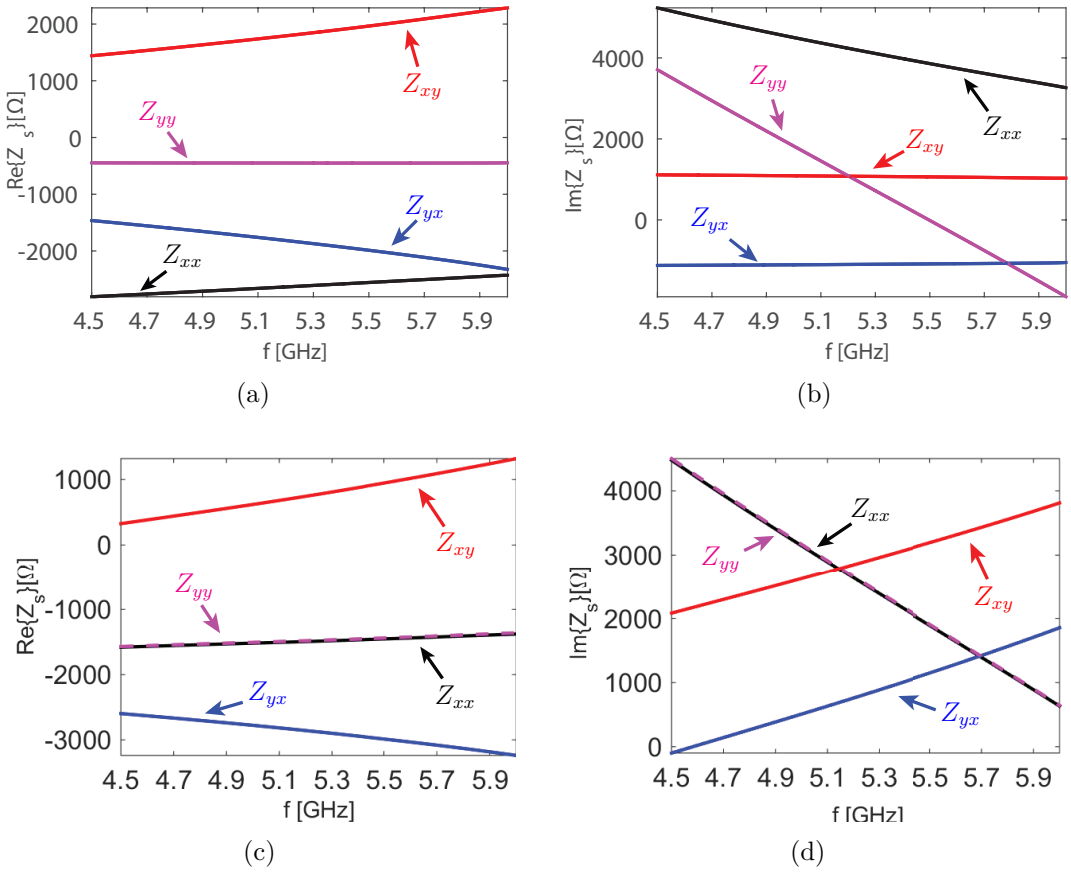

Figure 3.18 Extracted surface impedance parameters of the slot MNM resonant at 5.3 GHz (a) Real part. (b) Imaginary part. Extracted surface impedance parameters of the 45° rotated slot MNM (c) Real part. (d) Imaginary part.

CHAPTER 4 MULTI-LAYER SLOT MNMs STRUCTURE FOR MINIMAL REFLECTION

The goal of this chapter is to answer the question whether it is possible to design a transparent MNM with minimal reflection, and if it is possible, under which conditions it can be realized. In the first section, the existing methods that are used to cancel the reflection of non-reciprocal gyrotropic materials is reviewed. In next section, two fundamental reflection cancellation methods, namely exploiting the duality theorem and the Farby-Pérot resonances is discussed in detail. Then, multi-layer slot MNM design is suggested to achieve highly transparent MNMs, and analytical derivation of the condition that provides the minimized reflection is derived. Two design examples are provided to show how reflection of double-layer slot MNMs could be minimized. This section is concluded with the introduction of an optimization-based design method for the double-layer slot MNM design to control non-reciprocity and gyrotropy of the structure. Moreover, a design example is provided as a proof-of-concept.

4.1 Reflection Minimization for Non-reciprocal Gyrotropic materials

For many real life applications, reflected signal is an unwanted electromagnetic quantity since it is waste of the power and may be harmful for the devices. Thus, in microwave engineering it is always an important task to match circuit elements to ensure that all of the incident power is delivered to the load. In general, non-reciprocal gyrotropic materials such as magnetized ferrites and magneto-optical elements pose high characteristic impedances that cause the reflections. For the components that operate based on these non-reciprocal materials such as isolators and circulators, it is crucial to design fully transparent non-reciprocal components especially in high power applications.

Such a problem for the first time solved by Shul et al. [56] where they looked into the problem of propagation of normally incident plane waves through a gyromagnetic slab. The simple analysis provided that the reflection cancellation could be achieved at a certain slab thicknesses where the phase accumulation of the multiple reflections cancel each others. In addition, some magneto-optic materials have an inherent opaqueness due to the loss which limits the practical applications. To solve this issue, Dong et al. [57] designed a photonic crystal structure acting as a media with negative permeability so that the circularly polarized eigenstates can tunnel through it. Moreover, to solve the same issue, Moccia et. al [58] suggested a stacked layers of magneto-optic slabs and a dielectric slab to cancel the reflec-

tion by using the same method in [56]. Thus, it is possible to enhance the transmission and Faraday rotation angle of non-reciprocal gyrotropic materials.

The transparent slot MNMs introduced in Chapter 2 have great advantages compared to classical ferrite materials since it does not require permanent biasing magnets. However, it has inherent reflection due to its sub-wavelength thickness. This reflection level may reach approximately half of the incident power, as can be seen in Fig. 3.9. Thus, for practical applications, it is important to design a slot MNM which poses a minimal reflection.

4.2 Reflection Cancellation Methods

As discussed in the previous section, the tunneling of the RCP and the LCP plane waves are mainly used for the transparency and Faraday rotation angle enhancement based on multiple reflections. However, the fundamental duality theorem could also be used to provide reflection cancellation. In addition, Fano resonances where bright and dark states are coupled to induce transparency can be used to realize transparent MNMs. This thesis focuses on the duality theorem and multiple reflections for the reflection cancellation.

4.2.1 Exploiting the Duality Theorem

Duality is a concept where two quantity interchange with each other without causing any change in the system. Faraday law and Ampére law are inherently dual of each other except the non-existence of the magnetic currents so that the Maxwell equations poses the duality where $\mathbf{E}$ can interchange with $\mathbf{H}$, $\mathbf{H}$ with $-\mathbf{E}$, ε with μ etc.

For the first time Kerker et al. [59] used the duality theorem to cancel backscattering, namely reflection from a magnetoelectric spheres, where the electric and magnetic multipole coefficients of the Mie solution are dual. This observation can be applied to the electric and magnetic dipoles as

$$\mathbf{E}^p(\mathbf{r}) = \eta_0 \frac{ck^2}{4\pi}(\mathbf{n}\times\mathbf{p}\times\mathbf{n})\frac{e^{-jkr}}{r}, \tag{4.1}$$

$$\mathbf{E}^m(\mathbf{r}) = -\eta_0 \frac{k^2}{4\pi}(\mathbf{n}\times\mathbf{m})\frac{e^{-jkr}}{r}, \tag{4.2}$$

where $\mathbf{p}$ and $\mathbf{m}$ are electric and magnetic dipole moments, $\mathbf{E}^p$ and $\mathbf{E}^m$ are electric and magnetic fields radiated by the dipoles, c is the speed of light and $\mathbf{n}$ is the unit vector in the direction of the observation point $\mathbf{r}$. Thus, the summation of (4.1) and (4.2) can lead to the

cancellation of the radiated field into backward or forward direction under the condition

$$\mathbf{n} \times \mathbf{m} = -c \cdot \mathbf{n} \times \mathbf{p} \times \mathbf{n}, \tag{4.3}$$

known as the *Kerker condition*. The equation (4.3) is the exact duality condition between $\mathbf{m}$ and $\mathbf{p}$. This method of reflection cancellation is extensively used in metasurface design [60, 61, 62] since a metasurface can be characterized with its dipolar response due to the subwavelength nature of its $2D$ periodic scatterers.

Since the slot MNMs can be characterized with a rotating magnetic dipole moment, it should be possible to find a dual particle that can fully cancel the reflection of slot MNMs. It has been known form the field distribution in Fig. 3.10, the slot MNM can be replaced with either right-handed circularly rotating magnetic dipole moment or left-handed circularly rotating one, depending on the direction of the unidirectional component. If the direction of unidirectional component is assumed as in Fig. 3.2(a), the slot MNM can be replaced with $\mathbf{m} = m(\mathbf{e_x} + j\mathbf{e_y})$ where m is amplitude of the magnetic dipole moment. In order to cancel the reflected field from the slot MNM, based on (4.3), one needs to find a dual particle with the electric dipole moment

$$\mathbf{p} = -j\frac{m}{c}(\mathbf{e_x} + j\mathbf{e_y}), \tag{4.4}$$

where $\mathbf{n} = \mathbf{e_z}$ for the backward direction. Thus, in order to cancel the radiation of the slot MNM, it is required to have a right-handed circularly rotating electric dipole moment with

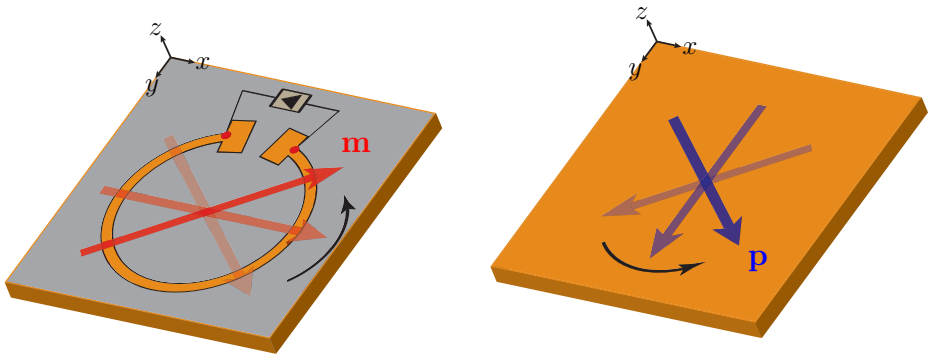

$\mathbf{m} = m(\mathbf{e_x} + j\mathbf{e_y})$ (a)

$\mathbf{p} = -j\frac{m}{c}(\mathbf{e_x} + j\mathbf{e_y})$ (b)

Figure 4.1 (a) Right-handed circularly rotating magnetic dipole moment model for slot MNMs. (b) Dual particle of a slot MNM, left-handed circularly rotating electric dipole moment, for the reflection cancellation.

the coefficient $-j\frac{m}{c}$ as shown in Fig. 4.1(b). Thus, there should be a $\pi/2$ phase difference between rotating magnetic and electric dipole moments. Such a structure that shows a rotating electric dipole moment response has not been realized so far due to the non-existence of magnetic charges and an unidirectional component for magnetic currents. Therefore, utilizing the Duality theorem to cancel the reflection of the slot MNM is not possible until the realization of a non-reciprocal gyrotropic material with rotating electric dipole moment response. In addition, even if such a structure exists the cancellation of the radiation via the dual particle is only valid when the two dual particle shares the same origin. Thus, it would be practically difficult to integrate two $2D$ periodic structure such that they preserves their rotating magnetic and electric dipole moment responses without any coupling. Note that the Kerker condition for slot MNM (4.4) is derived with the assumption of the circularly rotating magnetic dipole moment. Although, the designed slot MNM shows a elliptically rotating magnetic dipole moment response, the same analysis can be done for elliptically rotating magnetic dipole moments by using (4.3) so that for a elliptically rotating magnetic moment $\mathbf{m} = (m_x\mathbf{e_x} + jm_y\mathbf{e_y})$, the required electric dipole moment would be $\mathbf{p} = -\frac{j}{c}(m_y\mathbf{e_x} + jm_x\mathbf{e_y})$.

4.2.2 Exploiting Farby-Pérot Resonances

The other way of cancelling the reflections is to use deconstructive interferences of multiple reflections, namely Farby-Pérot resonances. The concept is based on resonances of a cavity that is formed by cascading two highly reflecting surfaces with a dielectric slab spacer such that at the resonance perfect transmission occurs. Thus, the quality factor of the resonance and the loss determine the performance of the Farby-Pérot cavity. The most important characteristic of the Farby-Pérot resonances is that the resonance repeat itself where the accumulated phase of the reflected fields are periodic with 2π. These characteristics are also known as Farby-Pérot artifacts since the slab acts as a Farby-Pérot cavity. Farby-Pérot resonators are widely used in interferometers to detect the wavelength of light, in lasers and optical filters due to its simplicity.

Thus, the fundamental idea behind the reflection cancellation from a layered anisotropic surfaces is summarized in Fig. 4.2 where the total reflection can be written as

$$\bar{\bar{R}} = \bar{\bar{R}}^{11} + \bar{\bar{T}}^{12} \cdot \bar{\bar{R}}^{11} \cdot \bar{\bar{T}}^{21} e^{-j2\theta} + \bar{\bar{T}}^{12} \cdot \bar{\bar{R}}^{11} \cdot \bar{\bar{R}}^{22} \cdot \bar{\bar{R}}^{11} \cdot \bar{\bar{T}}^{21} e^{-j4\theta} + \ldots, \tag{4.5}$$

where each layer partially reflect and transmit the incident plane waves with its dyadic coefficients. If the above infinite summation tends to be a zero dyadic due to deconstructive interference of the reflected terms, the reflection for the co- and the cross-polarized compo-

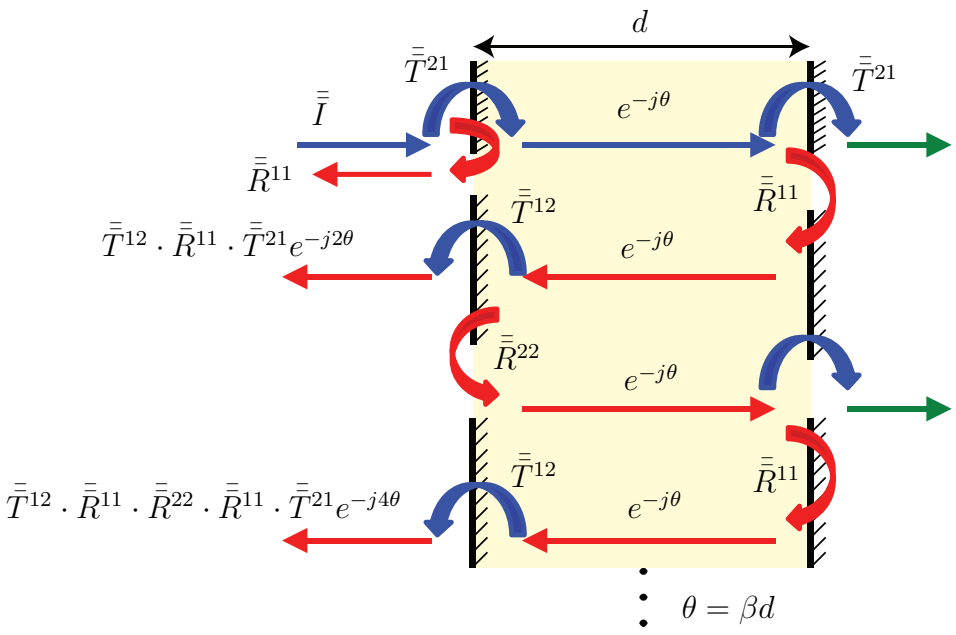

Figure 4.2 Schematic representation of the reflection from a multi-layered surface consisting of anisotropic single-layers.

nents cand be cancelled. The resonance frequency can be controlled by tuning the thickness d or the permittivity ε_d of the dielectric slab spacer.

As stated at the beginning of this chapter, the Farby-Pérot cavities has already been used to enhance the transparency and Faraday rotation angles of ferrite slabs. In addition, the slot MNM has a partial transparency that restrict its application areas. Therefore, due to the simplicity of implementing Farby-Pérot cavities, multiple resonances could be utilized to cancel the reflection of slot MNMs. However, due to the gyrotropy of the slot MNMs, co- and cross-polarized reflections occurs. In order to have a slot MNM with zero reflectance, all of the co-and cross-polarized reflections should be zero at the same time. Moreover, apart from the classical Farby-Pérot cavities, the asymmetry of the single-layer slot MNMs under x- and y-polarized plane wave incidence may cause further hurdles in the design.

4.3 Network Model for double-layer Slot MNM Structures

The easiest way to design highly transparent slot MNMs are forming a Farby-Pérot cavities by stacking slot MNMs with a dielectric slab spacer as seen in Fig. 4.3(a). The other way to cancel the reflections of slot MNMs is to exploit the Fano resonances where the near field interaction of bright and dark modes can create a transparency window as suggested in [63]. However, this method requires understanding and control of the near-field behaviour of slot

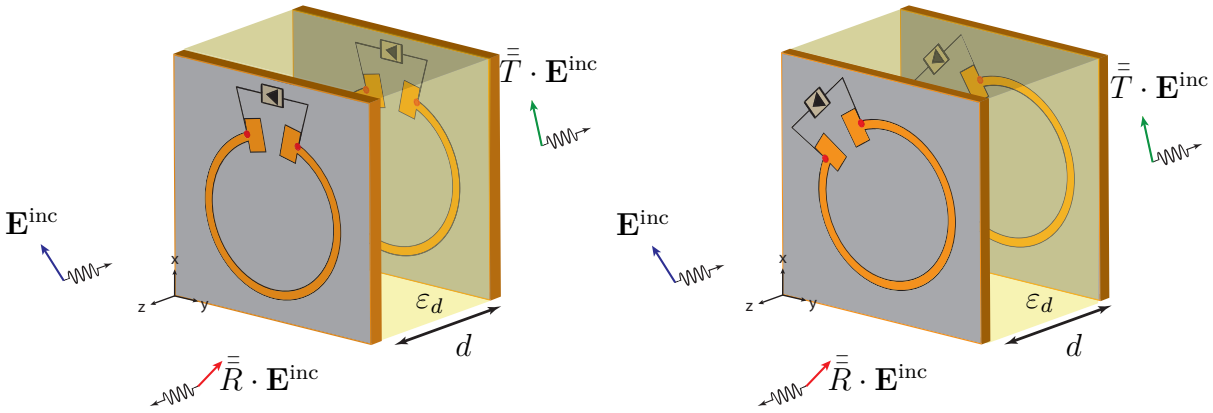

Figure 4.3 Double-layer slot MNM unit cell with a dielectric slab spacer whose permittivity ε_d and thickness d. The double-layer slot MNMs are made up from (a) Non-rotated single-layer slot MNMs. (b) 45° rotated single-layer slot MNMs.

MNMs. Due to the existence of longitudinal magnetic dipole moment as shown by (3.14), the problem would be very challenging and out of scope of this thesis.

In order to design a highly transparent MNMs with the Farby-Pérot resonances, the thickness d and the permittivity of the dielectric slab spacer ε_d should be determined in terms of the slot MNM parameters. Given the transverse rotating magnetic dipole moment response of the single-layer slot MNMs, the values of d and ε_d can analytically be derived in terms of the surface impedance parameters of the slot MNM by using the transmission-line model introduced in Section 3. Thus, the single-layer slot MNM can be characterized with a 4-port impedance element so that the double-layer transparent MNM structure seen in Fig. 4.3(a) can be modelled as three cascaded transmission lines. The $ABCD$ matrix of the double-layer slot MNM can be derived by cascading $ABCD$ matrix of the dielectric slab spacer for TE^z and TM^z waves, given as

$$\begin{bmatrix} \bar{\bar{A}}_d & \bar{\bar{B}}_d \\ \bar{\bar{C}}_d & \bar{\bar{D}}_d \end{bmatrix} = \begin{bmatrix} \cos\left(k_0 \bar{\bar{I}}\right) & j\eta_0^{-1} \bar{\bar{I}} \sin\left(k_0 \bar{\bar{I}}\right) \\ j\eta_0^{-1} \bar{\bar{I}} \sin\left(k_0 \bar{\bar{I}}\right) & \cos\left(k_0 \bar{\bar{I}}\right) \end{bmatrix}, \tag{4.6}$$

with $ABCD$ matrix of the single-layer slot MNM given in (3.35) as

$$\begin{bmatrix} \bar{\bar{A}} & \bar{\bar{B}} \\ \bar{\bar{C}} & \bar{\bar{D}} \end{bmatrix} = \begin{bmatrix} \bar{\bar{I}} & \mathbf{n} \times \bar{\bar{Z}}_s \times \mathbf{n} \\ \bar{\bar{0}} & \bar{\bar{I}} \end{bmatrix} \begin{bmatrix} \cos\left(k_d \bar{\bar{I}}\right) & j\eta^{-1} \bar{\bar{I}} \sin\left(k_d \bar{\bar{I}}_t\right) \\ j\eta^{-1} \bar{\bar{I}} \sin\left(k_d \bar{\bar{I}}_t\right) & \cos\left(k_d \bar{\bar{I}}_t\right) \end{bmatrix} \begin{bmatrix} \bar{\bar{I}} & \mathbf{n} \times \bar{\bar{Z}}_s \times \mathbf{n} \\ \bar{\bar{0}} & \bar{\bar{I}} \end{bmatrix}, \tag{4.7}$$

where $\bar{\bar{\eta}}_d$ is the characteristic impedance of the dielectric slab spacer for TM^z and TE^z polarized waves, and k_d is the wavelength inside the dielectric slab spacer. Therefore, the reflection and transmission coefficients of the structure can be found by employing the dyadic form of $ABCD$ matrix to S-parameter conversion formulas as

$$\begin{aligned}
\bar{\bar{R}}^{11} &= (\bar{\bar{A}} + \bar{\bar{B}} \cdot \bar{\bar{\eta}}_0^{-1} - \bar{\bar{\eta}}_0 \cdot \bar{\bar{C}} - \bar{\bar{D}}) \cdot (\bar{\bar{A}} + \bar{\bar{B}} \cdot \bar{\bar{\eta}}_0^{-1} + \bar{\bar{\eta}}_0 \cdot \bar{\bar{C}} + \bar{\bar{D}})^{-1}, \\
\bar{\bar{T}}^{21} &= 2 \cdot (\bar{\bar{A}} + \bar{\bar{B}} \cdot \bar{\bar{\eta}}_0^{-1} + \bar{\bar{\eta}}_0 \cdot \bar{\bar{C}} + \bar{\bar{D}})^{-1}, \\
\bar{\bar{R}}^{22} &= (-\bar{\bar{A}} + \bar{\bar{B}} \cdot \bar{\bar{\eta}}_0^{-1} - \bar{\bar{\eta}}_d \cdot \bar{\bar{C}} + \bar{\bar{D}}) \cdot (\bar{\bar{A}} + \bar{\bar{B}} \cdot \bar{\bar{\eta}}_0^{-1} + \bar{\bar{\eta}}_0 \cdot \bar{\bar{C}} + \bar{\bar{D}})^{-1}, \\
\bar{\bar{T}}^{12} &= 2 \cdot (\bar{\bar{A}} \cdot \bar{\bar{D}} - \bar{\bar{B}} \cdot \bar{\bar{C}}) \cdot (\bar{\bar{A}} + \bar{\bar{B}} \cdot \bar{\bar{\eta}}_0^{-1} + \bar{\bar{\eta}}_0 \cdot \bar{\bar{C}} + \bar{\bar{D}})^{-1}.
\end{aligned} \tag{4.8}$$

Thus, the reflection and transmission coefficients of the double-layer slot MNM structure can be calculated by using surface impedance parameters of the single-layer slot MNMs (here, it is extracted via HFSS simulations) and the same approach can easily be adopted to derive the reflection and transmission coefficients of a multi-layer slot MNM structures. It is important to note that the above $ABCD$ matrix derivation is only valid for normally propagating plane waves, since the transmission-line model of the single-layer slot MNM does not take into account the spatial dispersion effects. Therefore, the derived $ABCD$ matrix representation of the double-layer slot MNM is only valid where only the normally propagating plane waves, the zeroth order Floquet mode, interacts with the other layer. The thickness and the relative permittivity of the dielectric slab spacer directly affects the distance that evanescent higher order Floquet modes fade away. Thus, for a given relative permittivity ε_d, there is a minimum thickness $d_{\min}$ that dielectric slab spacer may have so that the $ABCD$ matrix formalism of the layered structure is valid. In addition, value of the dielectric permittivity ε_d cannot be selected randomly, since for larger values of the permittivity, the higher order Floquet modes will be propagating such that the transmission-line model cannot capture the physics. The choice of the ε_d should be tuned with the periodicity so that only the zeroth order Floquet mode is propagating.

The reflection dyadic elements of the double-layer slot MNM can be computed by inserting (4.7) into (4.8) as

$$R_{mn} = \frac{G_{mn}(\bar{\bar{Z}}) + jH_{mn}(\bar{\bar{Z}}) \tan(k_d d) + K_{mn}(\bar{\bar{Z}}) \tan^2(k_d d)}{D(\bar{\bar{Z}}) + jE(\bar{\bar{Z}}) \tan(k_d) + F(\bar{\bar{Z}}) \tan^2(k_d d)}, \tag{4.9}$$

where m and n is either x or y to represent the co- and cross-polarized coefficients, G_{mn}, H_{mn}, K_{mn}, D, E and F are coefficients as a function of the surface impedance parameters $\bar{\bar{Z}}_s$. The derived expressions for the coefficients in (4.9) is given in Appendix C. Thus, the

co- and cross-polarized reflection coefficients is represented as a ratio of two second order polynomial and simply roots of the numerator are the zeros of reflection coefficients if they are not overlap with the roots of the denominator. Thickness of the dielectric slab spacer that makes the reflection coefficients zero can be found by solving the second order polynomial equation in the numerator of (4.9) as

$$d_{mn} = \frac{1}{k_d}\left(\tan^{-1}\left(j\frac{H_{mn}(\bar{\bar{Z}}) \pm \sqrt{H_{mn}^2(\bar{\bar{Z}}) + 4G_{mn}(\bar{\bar{Z}})K_{mn}(\bar{\bar{Z}})}}{2C_{mn}(\bar{\bar{Z}})}\right) + q\pi\right), \tag{4.10}$$

where m and n denotes the polarization directions x or y, $q = 0, 1, 2, \ldots$. Therefore, for a general double-layer slot MNM design, there are 4 separate solution that make every element of the reflection dyadic zero. In the ideal case where the total reflection goes to zero, all thickness values found from (4.10) for co- and cross-polarized components should be same. Note that for the valid solution, the zeros and poles of (4.9) should not be the same [1]. Thus, for a given single-layer slot MNM design and the dielectric slab spacer, there is a theoretical solution that can suppress the reflection of double-layer slot MNM structure.

4.4 Design Example : Highly Transparent Non-reciprocity via double-layer Slot MNM

The first design of highly transparent MNMs by utilizing Farby-Pérot resonances is done by employing the single-layer slot MNMs resonant at 5.3 GHz with the parameters given in Table 3.1. This design is simply realized by cascading two single-layer slot MNM with an air gap. In addition, as mentioned in previous section the first step in the design process is to find the minimum spacer thickness, $d_{\min}$, where the network model given by (4.7) is valid. Thus, a parametric study is conducted in terms of different spacer thicknesses to determine $d_{\min}$. In Fig. 4.4(a) and 4.4(b), the cross-polarized transmission coefficient calculated with HFSS and the network model of the double-layer slot MNM given by (4.7) [2] is compared. It is clear that at $d = 3\,\text{mm}$, the cross-polarized transmission coefficient could not be accurately calculated both in amplitude and phase due to presence of non-negligible higher order evanescent Floquet modes. As the spacer thickness is increased, the matching between simulation and the analytical results are obvious due to the fading of the higher order Floquet modes. At $d = 9\,\text{mm}$, the simulation and the network model results are perfectly matched. Thus,

1. The root of denominator can be found by replacing G_{mn}, H_{mn} and K_{mn} with D, E and F in (4.10), respectively.

2. Network model result is calculated by employing the extracted surface impedance parameters of single-layer slot MNM.

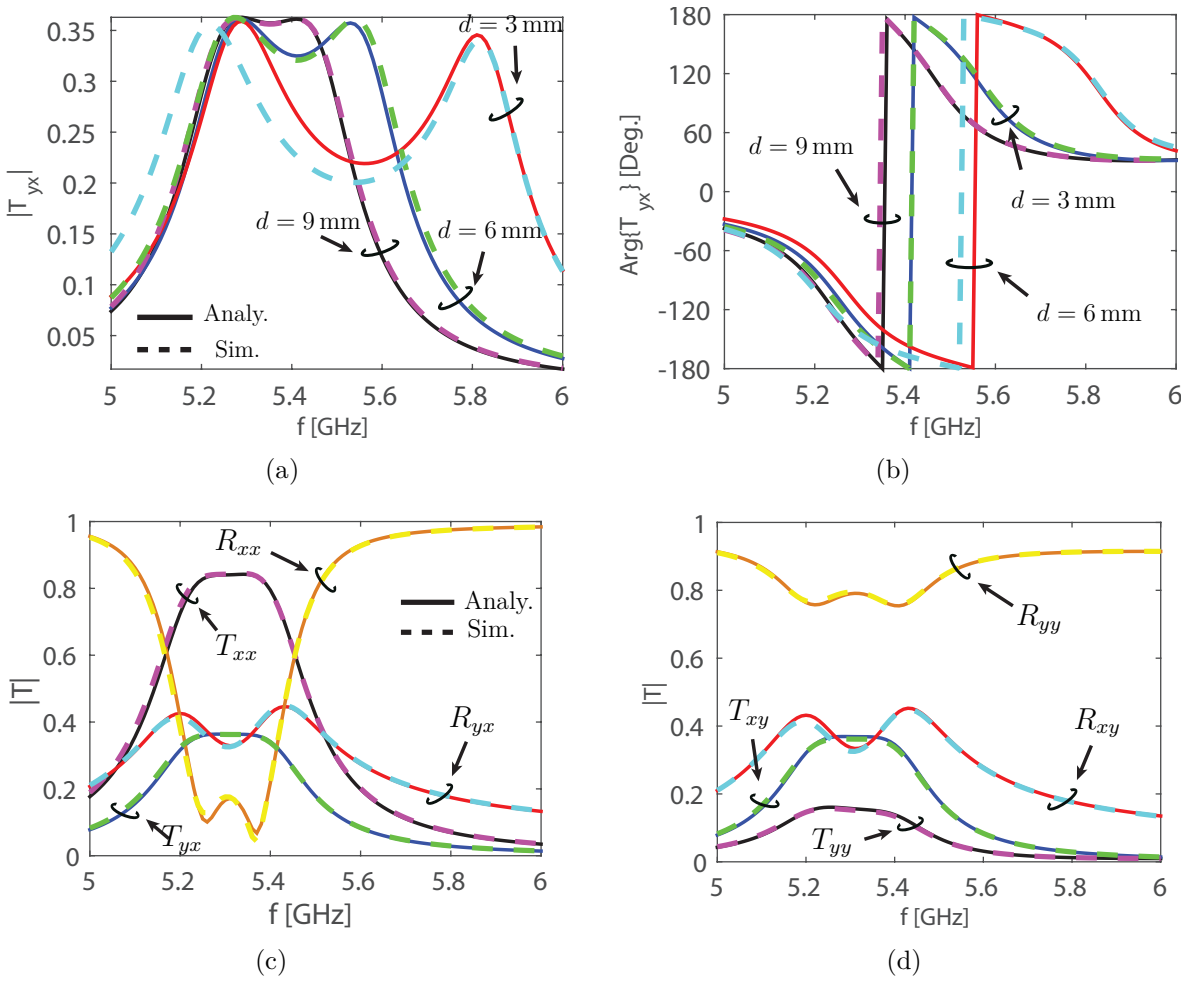

Figure 4.4 Comparison of the transmission coefficient T_{yx} obtained from numerical and analytical methods for different dielectric slab spacer thicknesses. (a) Amplitude (b) Phase. Reflection and transmission coefficients of the double-layer slot MNM for $d = 12\,\text{mm}$. (c) x-polarized plane wave incidence. (d)y-polarized plane wave incidence. Solid lines represents the simulation results obtained from HFSS, dashed lines refer to the results obtained from the analytical network model result (4.7). The single-layer slot MNM designed with parameters given in Table 3.1 and $\varphi_{is} = 127°$.

the minimum dielectric slab spacer thickness could be safely set as $d_{\text{min}} = 9\,\text{mm}$ where the network model (4.7) is valid. In order to elaborate this assertion, in Fig. 4.4(c) and 4.4(d), the amplitude of the reflection and transmission coefficients of the double-layer slot MNM is plotted when $d = 12\,\text{mm}$. The perfect overlapping between simulation and the network model results are evident thus, the network model (4.7) could be used to compute response of the cascaded slot MNMs with given surface impedance parameters of the single-layer slot MNM.

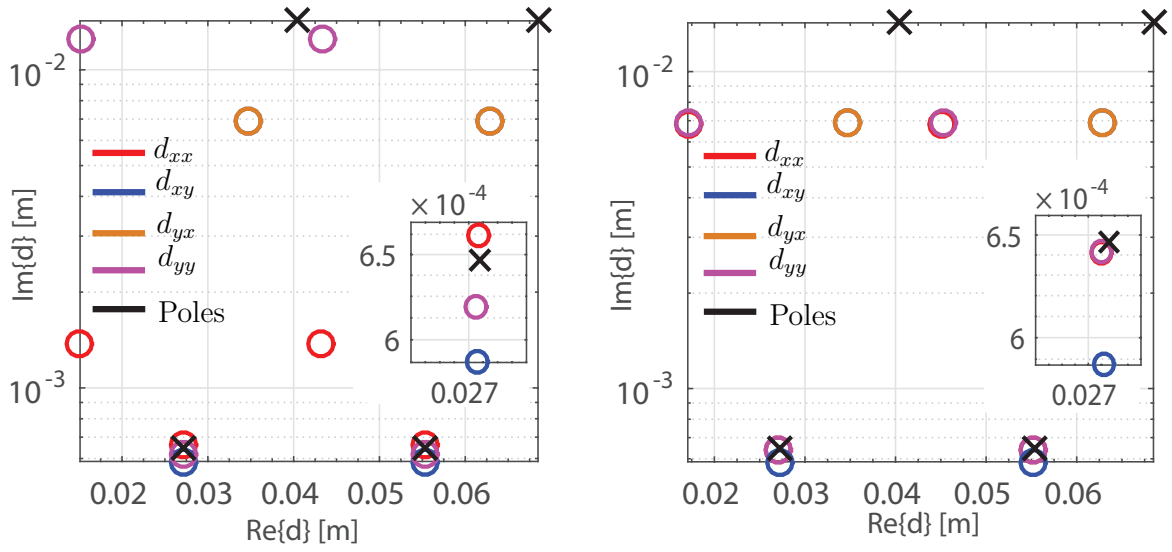

Figure 4.5 Zeros and poles of reflection coefficients of the double-layer slot MNM calculated from (4.9) for each co- and cross-polarized terms at 5.33 GHz. The double-layer slot MNM obtained from : (a) Non-rotated single-layer slot MNMs as in Fig. 4.3(a). (b) 45° counter-clockwise rotated single-layer slot MNMs as in Fig. 4.3(b). Circles represents the zeros and crosses refers to the poles of (4.9). Insets shows the zoomed version of the plots around $Re\{d\} = 27$ mm.

The solution of (4.10) for the given single-layer surface impedance parameters yields the spacer thicknesses that make the reflection coefficients of the multi-layer slot MNM zero. If the single-layer slot MNM design resonant at 5.3 GHz is employed to as a building block of double-layer slot MNM design, zeros and poles of the (4.9), i.e. the spacer thicknesses that provides zero reflection for double-layer slot MNM, could be found based on the formula (4.10) as in Fig. 4.5(a). Here, only first two solution set is plotted for demonstration. The first observation could be made from Fig. 4.5(a) is that the solutions are periodic with $\frac{q\pi}{k_d}$ due to the periodicity of the phase accumulation as expected from the Farby-Pérot resonances. Since there is no loss in the air, the periodicity will be only on the real axis. In addition, the poles of the (4.10) does not overlap with its zeros so that achieving the zero reflection coefficients seem feasible. However, there is no real solution for the spacer thickness even if the material losses are neglected because as pointed out in the previous chapter, the single-layer slot MNMs are inherently lossy due to the absorbance of the right- or left-handed eigenstate, evident from Fig. 3.16. Therefore, it is not possible to have a reflection-less non-reciprocity by exploiting the normally propagating plane wave interactions between single-layer slot MNMs. In addition, it is well known that the loss imposes major restrictions on using of the Farby-Pérot

cavities since even if the required phase is accumulated to cancel the reflection coefficient, amplitude of the multiple reflections are not constant. Thus, there is a trade-off between the achieved non-reciprocal gyrotropy and inherent loss of the structure since the time-reversal symmetry is broken by prohibiting the left-handed eigenstate propagation. Moreover, as seen from 4.5(a), the zeros of the (4.10) for each co-polarized reflection coefficients are different from each other due to the inherent asymmetry of the structure as can be seen from Fig. 3.7. Thus, co- and cross-polarized reflection coefficients cannot be made zero at the same time for a certain spacer thickness. In order to circumvent this issue the 45° rotated single-layer slot MNM could be used in the double-layer slot MNM design as seen in Fig. 4.3(b), since the single-layer structure has a symmetry under x- and y-polarized plane wave incidence as can be seen from Fig. 3.13. Therefore, the zeros of the co-polarized components occurs at the same the dielectric spacer thickness, d, as can be seen form Fig. 4.5(b), where the purple and red circles overlaps.

The slab thickness d is selected from the solutions of (4.10), where the imaginary part of the solutions are minimum. In addition, although resonance frequency of the single-layer structure is 5.3 GHz, the operation frequency is determined around 5.3 GHz where the zeros of (4.9) for co- and cross-polarized components are very close to each other. In Fig. 4.6(a), the reflection and transmission coefficients of the double-layer slot MNM made up from 45° rotated single-layer slot MNMs as seen from Fig.4.3(b) is plotted when $d = 0.027130$ mm. Due to the symmetry of the structure under x- and y-polarized plane wave incidence only the response under the x-polarized plane wave incidence is presented. It is obvious that the co- and cross-polarized reflection coefficients are far from being zero. Actually, if the results are compared with the response of the 45° rotated single-layer slot MNM given in Fig. 3.13(a), it is clearly seen that the reflection coefficient is decreased but it is less than 10%, hence the highly transparent slot MNMs could not be realized with this design. The fundamental reason behind this problem is clearly seen from Fig. 4.5(b), as the zeros of the reflection coefficients are complex rather than being real numbers due to the inherent loss of the single-layer slot MNM structure. As mentioned before, the loss is adversely affecting behaviour of resonators hence, the Farby-Pérot resonances in the double-layer slot MNM cavity is vanishing. The loss level of the structure [3] can be seen from Fig. 4.6(e) where the summation of absolute squares of the reflection and the transmission coefficient under RCP and LCP plane wave illumination is plotted. It is clear that under LCP plane wave incidence the total power scattered by the double-layer structure is resonant so that the unidirectional component absorb the left-handed eigenstate. Note that the loss level is different under the RCP and

3. For lossless electromagnetic structure, the summation of absolute squares of S-parameters should yield one. The loss level here is defined as how much the total power is far away from one.

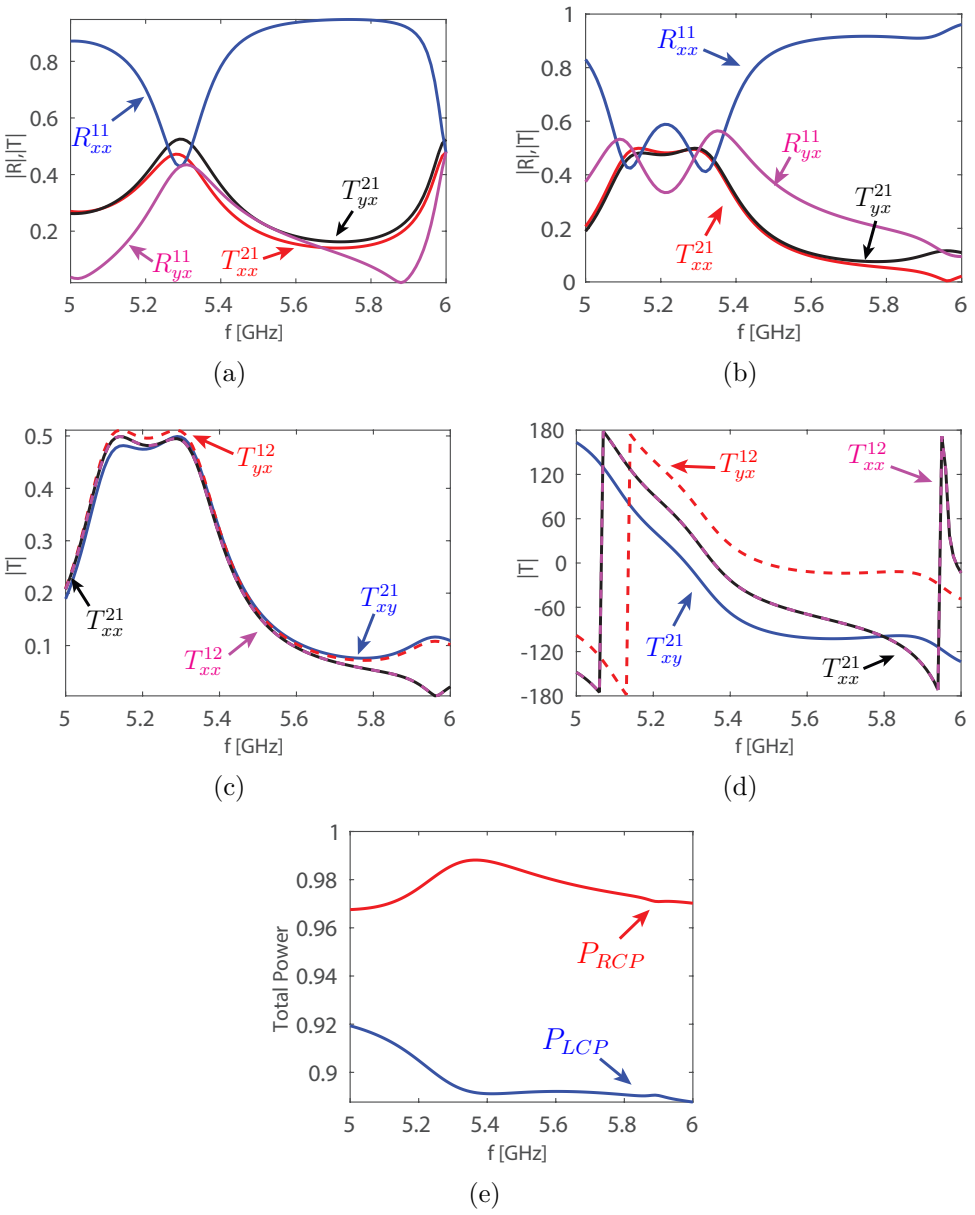

Figure 4.6 Reflection and transmission coefficients of the double-layered slot MNMs. Results obtained from : (a) The analytical solution (4.10) when $d = 0.027130\,\text{mm}$. (b) The optimization method when $d = 0.049430\,\text{mm}$. Non-reciprocity of the designed double-layer slot MNM : Comparison of the transmission coefficients when it is excited from $z > 0$ and $z < 0$ in time-reversal schema. (c) Magnitude. (d) Phase. (e) Total scattered powers of the single-layer slot MNM under normally propagating RCP and LCP plane waves incidence where $P_{RCP} = |R_{++}|^2 + |R_{-+}|^2 + |T_{++}|^2 + |T_{-+}|^2$ and $P_{LCP} = |R_{--}|^2 + |R_{+-}|^2 + |T_{--}|^2 + |T_{+-}|^2$.

the LCP plane wave illumination due to the removal of the degeneracy of the eigenstates by the unidirectional component. Moreover, even if the loss could be compensated in a way, due to the asymmetry of the RCP and the LCP transmission coefficients of the single-layer

slot MNM, Farby-Pérot resonances under the RCP and LCP plane wave illumination appear at different dielectric spacer thickness. Thus, the maximums of the RCP and the LCP transmission coefficient could not be achieved at a certain dielectric spacer thickness [4] so that the transmission coefficient under linearly polarized plane wave incidence cannot be one. In addition, the double-layer slot MNM made up from the non-rotated single-layer slot MNMs yields the same result where neither co-polarized nor the cross-polarized reflection coefficients could not be further decreased. In sum, due to the inherent loss of the structure and its RCP polarizer functionality, there is a trade off between the non-reciprocal gyrotropy and transmission level of the double-layer slot MNMs.

It should be questioned that since the zeros of the reflection coefficient (4.9) are complex, there may be a certain dielectric spacer thickness different from the real part of the (4.10) so that the reflection coefficients are minimized. In order to validate this assertion, *Global Optimization* toolbox of MATLAB is employed to find the global minimum of the reflectance where the cost function set as $f(d) = |R_{xx}|^2 + |R_{xy}|^2 + |R_{yx}|^2 + |R_{yy}|^2$. After feeding the optimization algorithm with several sets of random starting points, the global minimum of the cost function is achieved at $d = 0.049430\,\text{mm}$. In Fig. 4.6(b), the reflection and transmission coefficient of double-layer slot MNM made up from 45° rotated slot MNMs are plotted when $d = 0.049430\,\text{mm}$. The result yields a lower co-polarized reflection coefficient, but higher cross-polarized reflection coefficients when it is compared with the result of the network model given in Fig. 4.6(a). In addition, non-reciprocity of the optimized structure is shown in Fig. 4.6(c) and 4.6(d) where the structure shows non-reciprocal behaviour both in amplitude and phase as opposed to the magnetized ferrites. This behaviour is reasonable since the slot MNM unit cell is rotated 45° in order to achieve a symmetrical response under x- and y-polarized plane wave incidence so that the magnetized ferrite-like non-reciprocity is destroyed as seen from (3.5). Therefore, highly transparent slot MNMs could not be achieved with the current design of double-layer slot MNM cavities.

As mentioned before, magnetized ferrites are successfully used to form a Farby-Pérot

4. The interaction of the slot MNM with the RCP and the LCP plane wave incidence is non-degenerate

Table 4.1 Design parameters of the slot MNM resonating at 8.4 GHz.

Parameter	Value	Parameter	Value
ψ	15°	R	7.5 mm
ε_r	2.6	h	0.8 mm
W	0.2 mm	p	11 mm
L	2 mm	H	1.2 mm

cavity in order to enhance the transmittance and the Faraday rotation angle. In addition, it is crucial to pinpoint the differences between magnetized ferrite and the slot MNM Farby-Pérot cavities. The Farby-Pérot cavity formed by magnetized ferrites in [56, 58] yields real dielectric spacer thickness in the absence of the material loss thus, the zero reflection coefficients can be easily achieved for the RCP and the LCP plane wave incidence. However, the reflection coefficients under x- and y-polarized plane wave incidence cannot be made zero since the eigenstates of the magnetized ferrites, i.e. the RCP and the LCP plane waves, has different spacer thicknesses (non-degenerate) to make the reflection coefficients zero due to the different refraction index provided by the medium. In addition, as pointed out in [58], transmittance of the layered magnetized ferrite structure decrease from 0.8 to 0.3 in the presence of the material loss and the transmitted fields are elliptically polarized. As opposed to magnetized ferrites, the single-layer slot MNM does not pose same level of transmittance under the RCP and the LCP plane wave incidence since it does not transmit the one of the circularly polarized states due to the presence of the unidirectional component. In addition the single-layer structure shows a chirality due to the circular asymmetry of the structure. Since the degeneracy of the right- and left-handed eigenstates are removed by using a unidirectional component in single-layer slot MNM design, the inherent loss is inevitable. Such a lossy behaviour can not be seen in magnetized ferrites since the degeneracy is removed by a permanent magnets. Thus, although the single-layer slot MNM can show a magnetized ferrite-like non-reciprocal gyrotropy, its interaction with the RCP and the LCP plane waves are different from the magnetized ferrite case. Therefore, the response of the Farby-Pérot cavity formed by the single-layer slot MNMs is not the exact replica of the one formed by the magnetized ferrites.

The Farby-Pérot resonances in the double-layer slot MNM still could be used to achieve high transparency and large Faraday rotation angle by exploiting the trade-off between the non-reciprocity of the single-layer slot MNM and its inherent loss. Thus, the matching of the unidirectional component can be degraded by changing the dimensions of the big slot patch in Fig. 3.2(b) so that the left-handed eigenstate will not be absorbed totally in expense

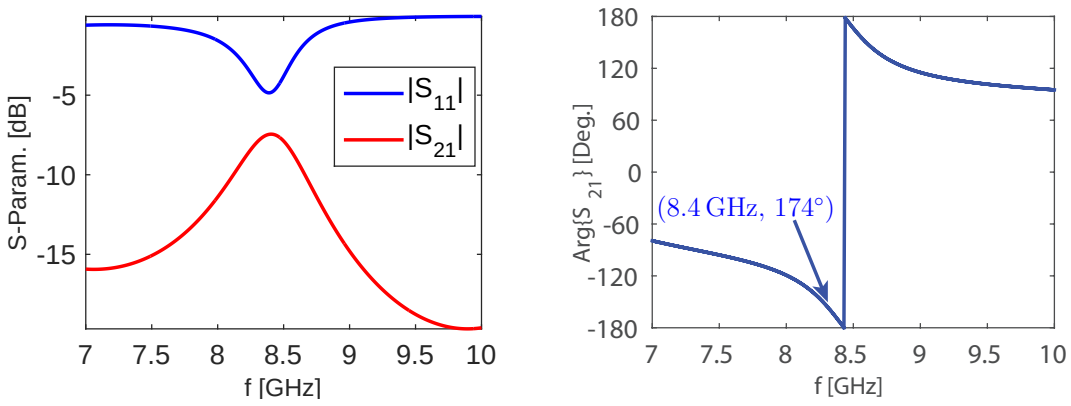

Figure 4.7 (a) S-parameters of the ports A and B, shown in Fig. 3.2(c). (a) Magnitude of S_{11} and S_{21} computed by HFSS. (d) Phase of S_{21} computed by HFSS.

of the less gyrotropy (non-reciprocity) hence, the loss level decreases as suggested in [64]. The designed double-layer slot MNM could be both non-reciprocal and highly transparent since the zeros of the reflection coefficients (4.10) is closer to the real axis. Therefore, a new single-layer slot MNM based on parameters given in Table 4.1 is designed to achieve a non-reciprocal gyrotropic response at 8.4 GHz. S-parameters of the unloaded annular slotted ring at points A and B of Fig. 3.2(a) is plotted in Fig. 4.7 where the port impedances at points A and B is 10 Ω. It is obvious that matching of the annular slotted ring and the unidirectional component is not perfect as desired where only %25 of the incident power is inserted into the unidirectional component. In addition, the annular slotted ring structure is designed to have 180° electrical length in order to have a non-reciprocal gyrotropic resonance at 8.4 GHz with $\varphi_{is} = 180°$ according to the design formula (3.1). The simulation results in Fig. 4.7(b) shows that the simulated unloaded structure has approximately half wavelength electrical length hence, a unidirectional component with phase shift of $\varphi_{is} = 180$ can be used. In order see the effect of imperfect matching of annular slotted ring and unidirectional component in the slot MNM design, the electromagnetic response of the structure should investigated in detail. The reflection and transmission coefficients of the designed slot MNM under x- and y-polarized plane wave incidence from $z > 0$ region is plotted in Fig. 4.8(a) and 4.8(b), respectively. It is obvious that due to the imperfect matching, the gyrotropy is decreased since the rotating magnetic dipole response is very weak, however there is still a resonance behaviour at 8.4 GHz. In addition, as in the previous single-layer slot MNM design, the asymmetry of the structure under x- and y-polarized plane wave incidence could be seen

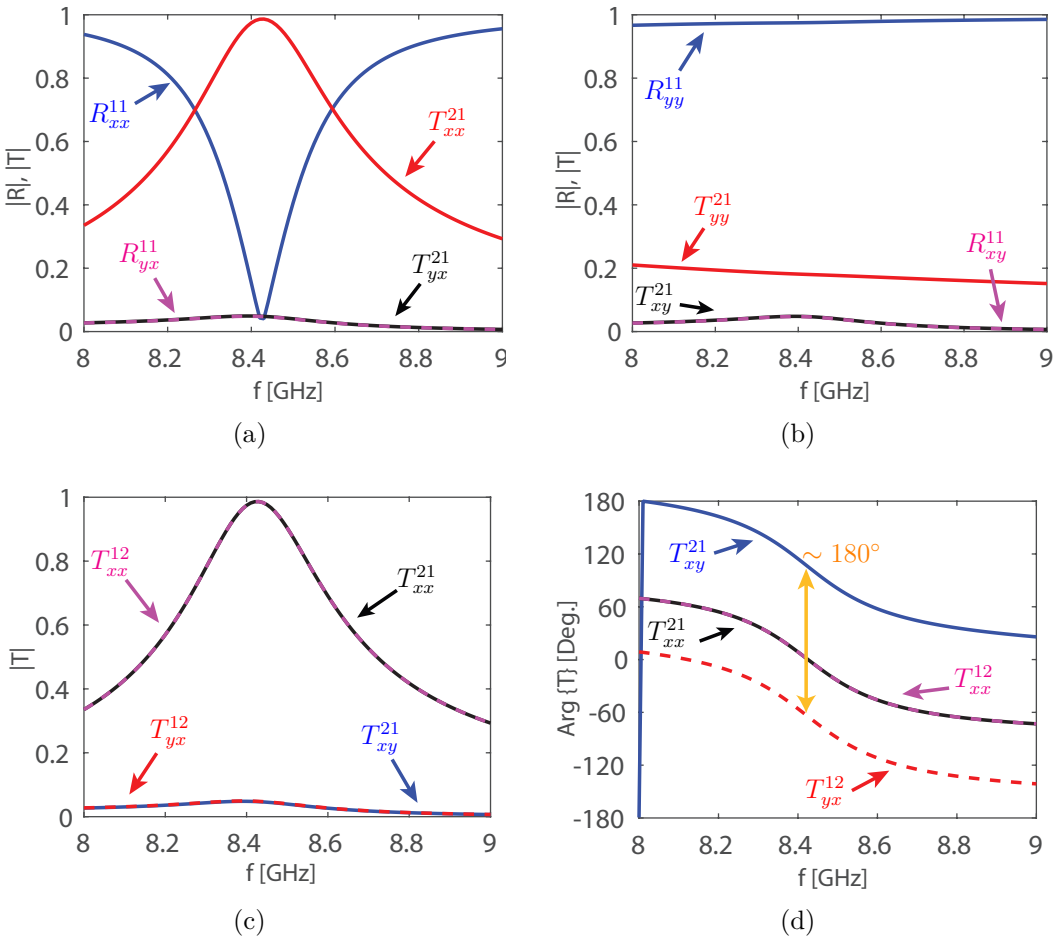

Figure 4.8 Reflection and transmission coefficients of the designed single-layer slot MNM based on parameters given in Table 4.1 under plane wave illumination from $z > 0$.(a) x-polarized plane wave incidence. (b) y-polarized plane wave incidence. Non-reciprocity of the designed single-layer slot MNM : Comparison of the transmission coefficients when it is excited from $z > 0$ and $z < 0$ in time-reversal schema. (c) Magnitude. (d) Phase.

clearly. Although the resonance is heavily damped due to the imperfect matching, as it can be seen form Fig. 4.8(c) and 4.8(d), the designed structure has a magnetized ferrite-like non-reciprocal gyrotropy where amplitude of the cross-polarized transmission coefficient are same and they have 180° phase difference when the time is reversed. Therefore, the design goal in imperfectly matched single-layer slot MNM is satisfied where inherent loss of the structure is diminished and non-reciprocity is preserved in the expense of less gyrotropy.

Since the designed slot MNM has also circular asymmetry, the reflection cancellation of co-polarized components occur at different spacer thicknesses thus, the minimal reflection cannot be achieved. To circumvent this issue, the slot MNM unit-cell is 45° rotated in order to have a symmetric transmission and reflection coefficients for co- and cross-polarized components,

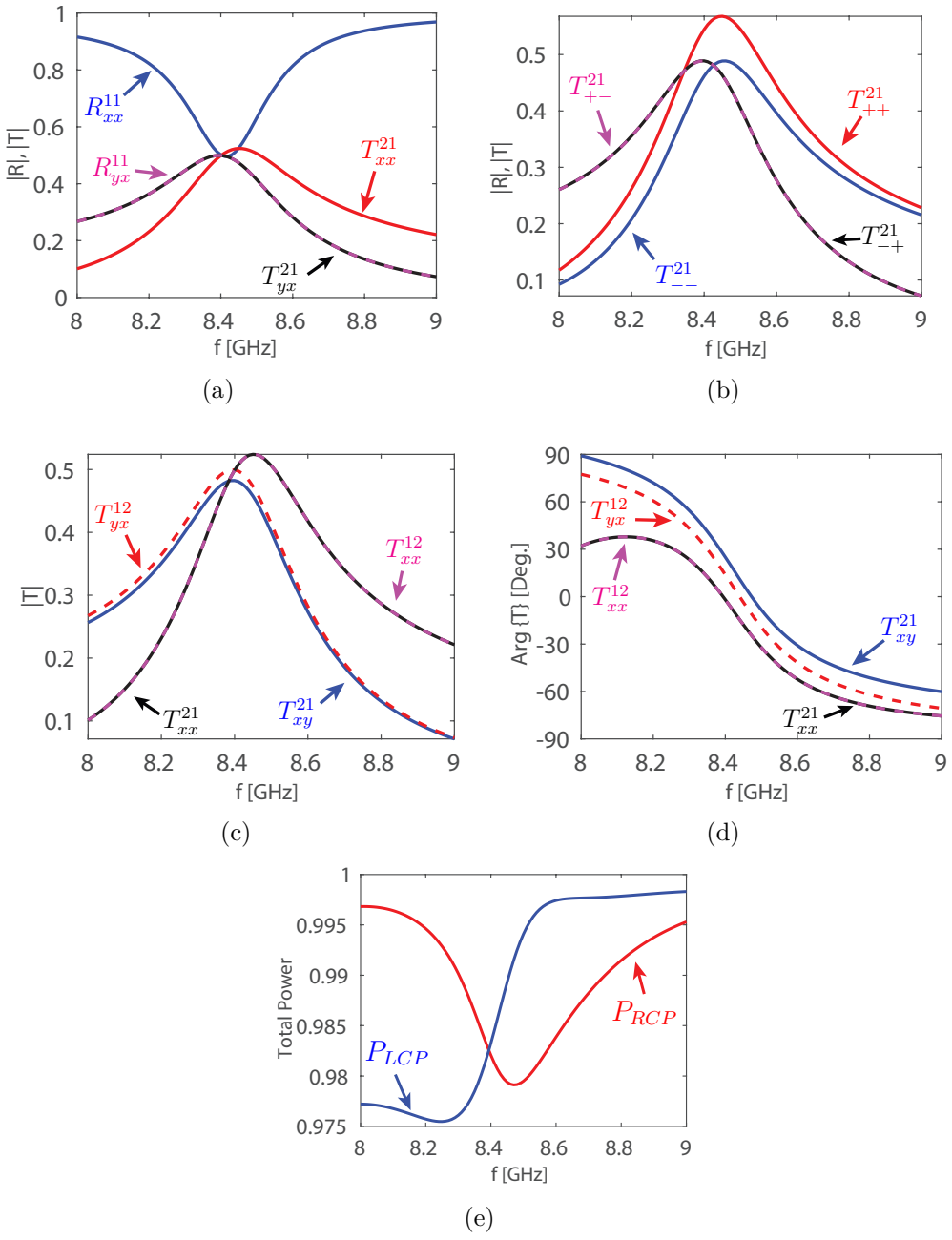

Figure 4.9 (a) Reflection and transmission coefficients of the 45° rotated single-layer slot MNM under x-polarized plane wave illumination from $z > 0$. (b) Transmission coefficients of the 45° rotated single-layer slot MNM under RCP and LCP plane wave illumination from $z > 0$. Non-reciprocity of the 45° rotated single-layer slot MNM : Comparison of the transmission coefficients when it is excited from $z > 0$ and $z < 0$ in time-reversal schema. (c) Magnitude. (d) Phase. (e) Total scattered powers of 45° rotated single-layer slot MNM under normally propagating RCP and LCP plane wave incidence where $P_{RCP} = |R_{++}|^2 + |R_{-+}|^2 + |T_{++}|^2 + |T_{-+}|^2$ and $P_{LCP} = |R_{--}|^2 + |R_{+-}|^2 + |T_{--}|^2 + |T_{+-}|^2$.

as done in the previous single-layer design. The reflection and transmission coefficients of 45° rotated single-layer slot MNM is presented in Fig. 4.9(a) where the electromagnetic response of the structure is similar to results of the previous design given in Fig. 3.13(a). It is clear that the non-reciprocity both occur in amplitude and phase of the transmission coefficients, although the difference between transmission coefficient and its time-reversed counterpart is small, ~ 0.01 in amplitude and $\sim 12°$ in phase. This behaviour could not be seen in the matched single-layer slot MNM design at 5.3 GHz, as seen from Fig. 3.13(c) and 3.13(d) since the non-reciprocal gyrotropy only appears at the phase.

In order to show whether using imperfectly matched single-layer slot MNMs is feasible

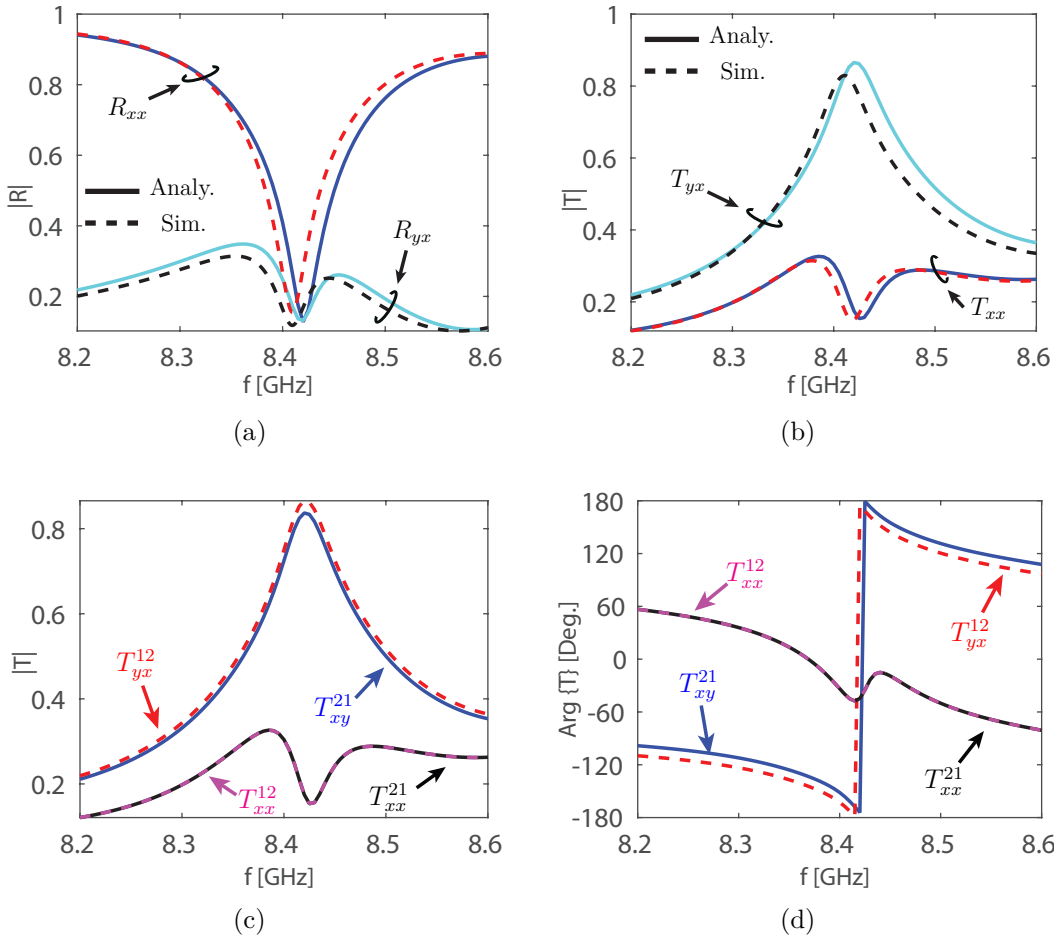

Figure 4.10 Reflection and transmission coefficients of the double-layered slot MNM made up from unmatched single-layer slot MNMs when $d = 36.66$ mm. (a) The reflection coefficients. (b) The transmission coefficients. Non-reciprocity of the double-layer slot MNM : Comparison of the transmission coefficients when it is excited from $z > 0$ and $z < 0$ in time-reversal schema.(c) Magnitude.(d) Phase.

or not to form a Farby-Pérot cavity, the summation of absolute squares of the each reflection and the transmission coefficients under the RCP and the LCP plane wave illumination is plotted in Fig. 4.9(e). It can be clearly seen that the single-layer slot MNM is lossy for both incident waves as expected from the effect of unidirectional component even if it is imperfectly matched. It is important that if the power conservation of the previous design given in Fig. 4.6(e), is compared with the current design, it is clear that the loss level is decreased when imperfect matching of unidirectional component is used as expected since the left-handed propagating state is not absorbed, well. In addition, transmission coefficients of the single-layer slot MNM under the RCP and the LCP plane wave incidence is plotted in Fig. 4.9(b) where as opposed to the perfectly matched single-layer slot MNM design, the structure does not behave like a RCP polarizer as seen in Fig.3.12(a). This behaviour is also well explained with the presence of low level loss, since the left-handed propagating wave is not perfectly absorbed so that the right- and left-handed propagating eigenstates closer to be degenerate. Thus, as in the case of magnetized ferrites, the RCP and LCP waves are transmitted through structure approximately at the same level and non-reciprocal gyrotropy is achieved so that the Farby-Pérot resonances of the multi-layer slot MNM structure can yield linearly polarized wave with high transmission levels. This response may not be achieved with the perfectly matched slot MNM design since the structure act as RCP polarizer. Therefore, the imperfectly matched single-layer slot MNM design is feasible to be used in the Farby-Pérot cavity design to achieve highly transparent MNMs due the low level inherent loss of the structure compared to the perfectly matched case.

In order to form a Farby-Pérot cavity based on the network model (4.7), first the minimum dielectric spacer thickness in the double-layer slot MNM design should be identified so that the evanescent wave coupling between layers are negligible. If a parametric study based on different thicknesses of an air slab is done as in the case of perfectly matched slot MNM design, the minimum dielectric spacer thickness can be found as $d_{\min} = 25\,\text{mm}$ for the frequency range 2 GHz - 10 GHz. Thus, the real part of the dielectric spacer thickness found from (4.10) can be used to form a Farby-Pérot cavity. If the surface impedance parameters of the 45° rotated and imperfectly matched single-layer slot MNM is extracted by using (3.34) from the HFSS simulation results in Fig. 4.9(a) and employed in (4.10), the first two air slab thicknesses that makes all the reflection coefficients zero at 8.42 GHz can be found as 36.66 mm and 54.46 mm. In Fig. 4.10(a) and 4.10(b) the reflection and transmission coefficients of the Farby-Pérot cavity, formed by using two 45° rotated imperfectly matched single-layer slot MNM and an air slab with thickness 36.66 mm, is plotted, respectively. The dashed lines corresponds to HFSS simulation results and the solid lines refers to the analytical network

model based on (4.7) The agreement between curves are very good as expected since $d > d_{\min}$. It can be clearly seen that at 8.42 GHz, all the co- and cross-polarized reflection coefficients close to be zero and the co-polarized transmission coefficient is also minimum. The fractional bandwidth of the structure is 0.35%. The bandwidth is defined as a region where the cross-polarized transmission coefficient is bigger than -3 dB and the co-polarized reflection coefficient is smaller than -10 dB. Thus, the designed double-layer slot MNM works as a highly transparent 90° polarization rotator which is an ideal response for a Faraday rotator if the device is non-reciprocal. Thus, in Fig. 4.10(c) and 4.10(d), the co- and cross-polarized transmission coefficients of the structure with its time-reversed counterparts are plotted. It is clear that the double-layer slot MNM is non-reciprocal, although the difference between the transmission coefficient and its time-reversed counterpart are small, ~ 0.03 in amplitude and $\sim 12°$ in phase. The low level of the non-reciprocal gyrotropy is evident since the matching of the single-layer structure is deliberately degraded. In addition, the ellipticity and the Faraday rotation angle of the double-layer structure is plotted in Fig. 4.11(a) and 4.11(b), respectively. It is clear that close to the Farby-Pérot resonance frequency, the transmitted wave becomes linearly polarized since the transmission levels of RCP and LCP plane waves are close as seen in Fig. 4.9(b). Moreover, as seen in Fig. 4.11(b), the Faraday rotation angle shows a resonant behaviour at 8.42 GHz and reach up to 86° so that for single-layer imperfectly matched slot MNM this was 43°, as shown in Fig. 4.9(a). These indicate that by employing a imperfectly matched double-layer slot MNM design, the transmittance and Faraday rotation angle can be enhanced. Note that the Faraday rotation angle under x- and y- polarized plane wave incidence is symmetric but not around 0°, because the 45° rotated annular slotted ring structure

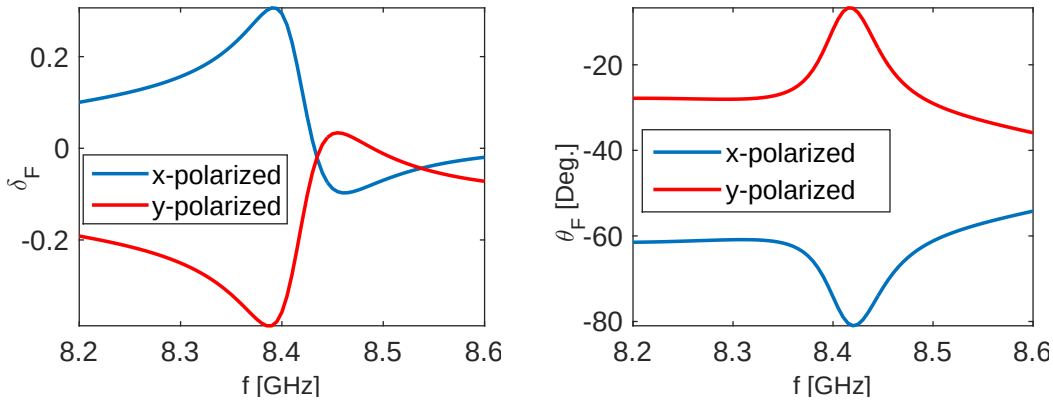

Figure 4.11 (a) Ellipticity of the double-layer slot MNM. (b) Faraday rotation angle of the double-layer slot MNM.

already shows a gyrotropic response where reciprocal the polarization rotation angles are $\sim -30°$ and $\sim -60°$ under x- and y-polarized plane wave incidence, respectively. By loading the annular ring structure with an unidirectional component, the rotating magnetic dipole moment introduce a non-reciprocal gyrotropy with the Faraday rotation angles $\pm 26°$ under x- and y-polarized plane wave incidence. Therefore, the Faraday rotation angles is plotted in Fig. 4.11(b) are the combination of the reciprocal and non-reciprocal polarization rotations. In sum, as asserted in previous paragraph, inherent loss of the single-layer slot MNM prohibits using of the Farby-Pérot resonances to minimize the reflectance, however if the loss level is decreased by simply destroying the rotating magnetic dipole resonance of the structure, the reflectance can be minimized by preserving the non-reciprocal gyrotropy as seen in Fig. 4.10. It should be noted that the non-reciprocal behaviour of the double-layer structure does not mimic the magnetized ferrite response due to the aforementioned asymmetrical reflection and transmission coefficients of the single-layer slot MNM structure.

4.5 Controlling Gyrotropy and Non-reciprocity by using Multi-layer Slot MNMs

The highly transparent slot MNMs are realized based on Farby-Pérot resonances in the previous section when the imperfectly matched single-layer slot MNMs are employed. It was well emphasized that if the perfectly matched single-layer slot MNMs are used, the reflection minimization cannot be achieved. However, the unperfect matching of annular slotted ring and the unidirectional components results in a weak non-reciprocal gyrotropic response. Thus, for the practical applications, it is important to achieve a high level of non-reciprocal gyrotropy with the minimized reflections.

So far the multi-layer slot MNMs consisting of identical layers are considered, however the

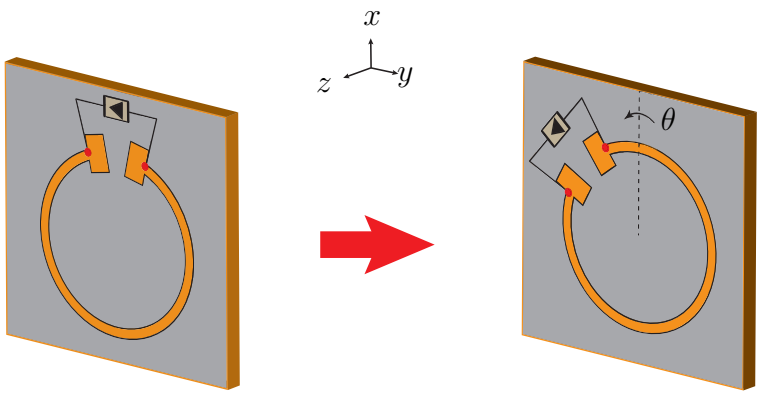

Figure 4.12 Rotation of a slot MNM around z axis

single-layer slot MNMs that pose different properties can be cascaded to exploit the added degrees of freedoms. Fundamentally, each single-layer slot MNM is characterized with its resonant frequency which can be controlled with the size of the annular slotted ring or the phase shift of the unidirectional component according to (3.1) as

$$f_m = \frac{c(2\pi m - \varphi_{is})}{2\pi\ell\sqrt{\varepsilon_{eff}}}, \tag{4.11}$$

where m is the order of the resonance and ε_{eff} is the effective permittivity of the substrate. In addition, since the designed slot MNM poses an asymmetric response under x- and y-polarized plane wave illumination, rotation of the single-layer slot MNM unit-cell, as seen in Fig. 4.12, is another property that characterize behaviour of the slot MNM. Thus, each slot MNM may have a certain non-reciprocal gyrotropic response for a certain phase shift of the unidirectional component [5] and a certain rotation angle which can be exploited to control the gyrotropy and the non-reciprocity of the structure. Moreover, the surface impedance of any single-layer slot MNM can be written as a function of the rotation angle θ and the phase shift of the isolator φ_{is}, i.e. $\bar{\bar{Z}}(\theta, \varphi_{is})$. The surface impedance parameters of a slot MNM can analytically be calculated for a certain phase shift of the unidirectional component from (3.2) and certain rotation angle by using the identity

$$\bar{\bar{Z}}(\theta) = \bar{\bar{R}}(\theta) \cdot \bar{\bar{Z}} \cdot \bar{\bar{R}}^{-1}(\theta), \tag{4.12}$$

where $\bar{\bar{R}}$ is the rotation matrix given by (3.7). It is important to note that (4.12) is less accurate when the periodicity of the structure is getting bigger since the lattice configuration of the 2D periodic array changes after the rotation with (4.12). Thus, if the interaction between elements of the 2D periodic array are negligible, any change in the effective lattice configuration has a big effect on the electromagnetic response of the structure.

In Fig. 4.13, the wide parameter space that a single-layer slot MNM poses is plotted at 8.4 GHz where the surface impedance tensor of a single-layer slot MNM is computed when the single-layer slot MNM unit cell is rotated as in Fig. 4.14 in the range of $0 \leq \theta \leq 180°$ and the phase shift of the unidirectional component varied in the range of $0 \leq \theta < 360°$. It is clear that for a certain rotation of the unit cell and a certain phase shift of the unidirectional component, the single-layer slot MNM has a distinct non-reciprocal gyrotropic response where (2.3) holds for each parameter pairs. Thus, a wide range of non-reciprocal gyrotropic surface impedance parameters can be utilized the control the non-reciprocity and the gyrotropy of

5. Due to the ease of use, in the rest of the thesis, the resonance frequency of the single-layer slot MNM is controlled with the phase shift of the isolator rather than the radius of the annular slotted ring.

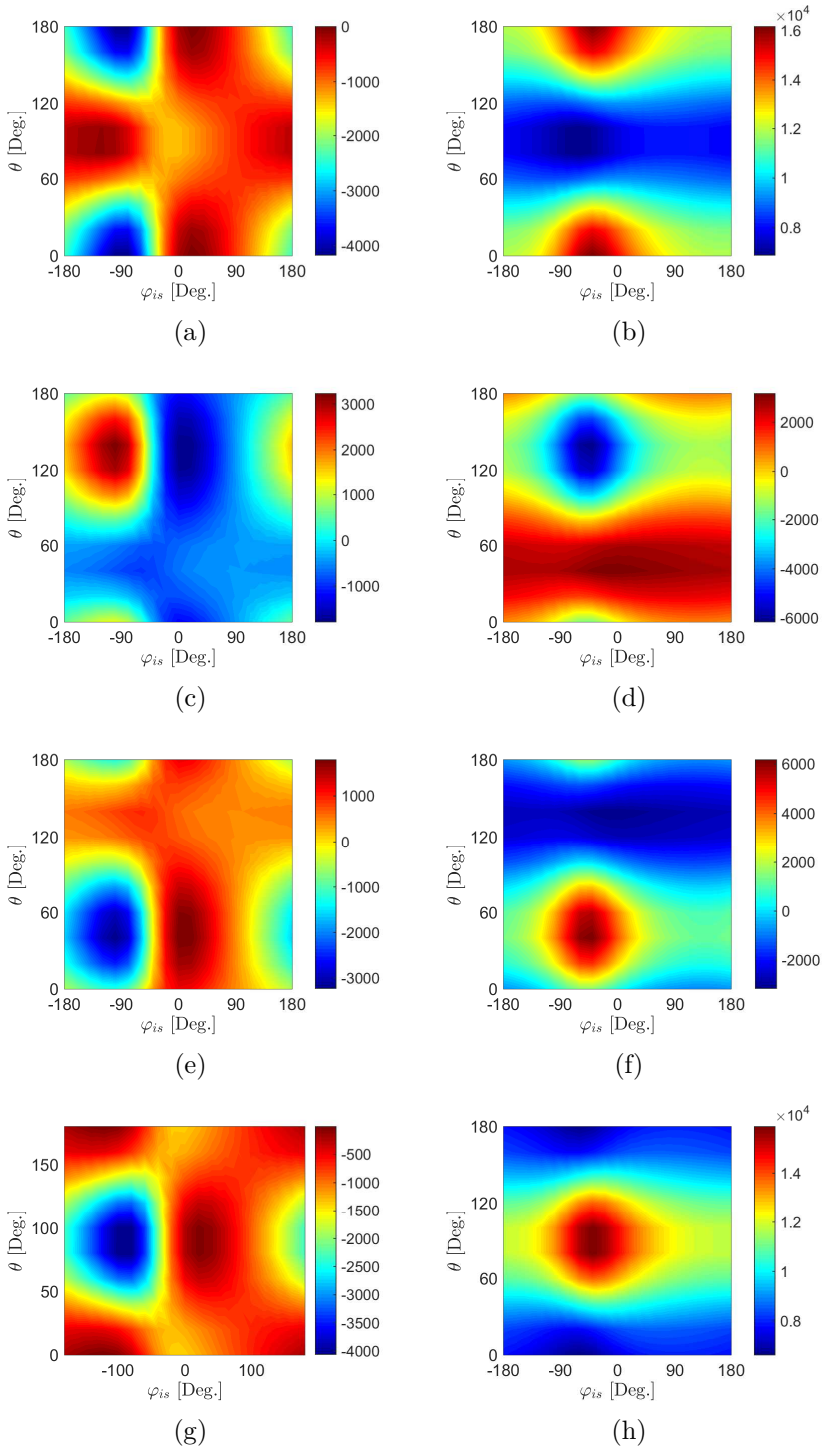

Figure 4.13 Surface impedance parameters of the imperfectly matched slot MNM for different phase shifts φ_{is} and rotation angles θ. (a) Real part of Z_{xx}. (b) Imaginary part of Z_{xx}. (c) Real part of Z_{xy}. (d) Imaginary part of Z_{xy}. (e) Real part of Z_{yx}. (f) Imaginary part of Z_{yx}. (g) Real part of Z_{yy}. (h) Imaginary part of Z_{yy}.

MNMs. Although the parameter space that is shown in Fig. 4.13 is restricted to a certain level of surface impedance values, the range of non-reciprocal surface impedance values could be expanded by using a different slotted structures such as slotted ellipsoid rings or slotted rectangle rings etc.

In order to control the non-reciprocal gyrotropic response of the slot MNM structure, the design given in Fig. 4.14, where the two slot MNMs with different rotation angles and different the unidirectional components are cascaded, is utilized. Each layer of the double-layer slot MNM differently interacts with the TM^z and TE^z polarized normally propagating plane waves so that the multiple reflections cancel each other on illumination region and create the desired non-reciprocal gyrotropic response in the transmission region. Although analytical solution for the dielectric spacer thickness between the layers that minimize the reflection could be found similar to (4.10), the transmission coefficients would be ambiguous. Therefore, it is required to use either a parametric study based on the change of the rotation angle θ and phase shift φ_{is} or an optimization algorithm to minimize the given cost function. Thus, a non-linear constraint optimization problem need to be defined and be solved to control the gyrotropy and non-reciprocity. A similar optimization problem is used to design bianisotropic metasurfaces for optimal polarization control in [36], however the research was restricted to the reciprocal metasurfaces.

The design method could be outlined as follows : In the first step, the desired transmission dyadics $\bar{\bar{T}}^{12}$ and $\bar{\bar{T}}^{21}$ should be defined where $\bar{\bar{R}}^{12}$, $\bar{\bar{R}}^{21}$ is set automatically based on power conservation. In the second step, the constraints should be defined such as the passivity condition, range of the surface impedance parameters, lower and upper bounds for the

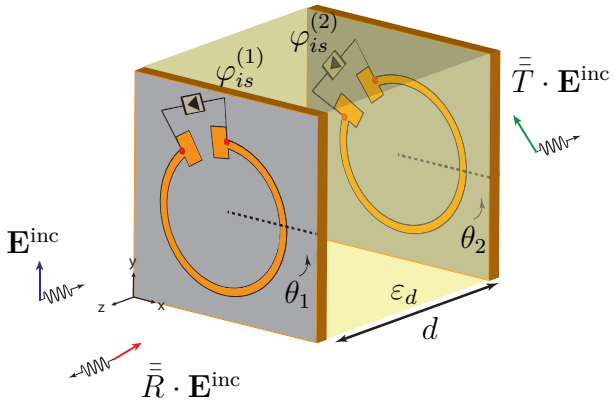

Figure 4.14 Double-layer slot MNM design formed by using different single-layer slot MNMs with rotation angles θ_1, θ_2 and phase shifts $\varphi_{is}^{(1)}$, $\varphi_{is}^{(2)}$ in order to control gyrotropy and non-reciprocity.

dielectric spacer thickness etc. In the third step, the cost function should be defined such as

$$\begin{aligned}\text{Cost Func.} = &|T^{21}_{xx} - T^{21}_{d_{xx}}|^2 + |T^{21}_{xy} - T^{21}_{d_{xy}}|^2 + |T^{21}_{yx} - T^{21}_{d_{yx}}|^2 + |T^{21}_{yy} - T^{21}_{d_{yy}}|^2 \\ &|T^{12}_{xx} - T^{12}_{d_{xx}}|^2 + |T^{12}_{xy} - T^{12}_{d_{xy}}|^2 + |T^{12}_{yx} - T^{12}_{d_{yx}}|^2 + |T^{12}_{yy} - T^{12}_{d_{yy}}|^2, \end{aligned} \tag{4.13}$$

where $\bar{\bar{T}}^{mn}$ represents the achieved transmission dyadic when the double-layered slot MNM is excited from region n and probed from region m and $\bar{\bar{T}}^{mn}_d$ represents the desired transmission dyadic when the double-layered slot MNM is excited from region n and probed from region m. In the fourth step, an optimization method is used to minimize (4.13) for surface impedances of each layer $\bar{\bar{Z}}_1$ and $\bar{\bar{Z}}_2$. Lastly, the optimum solution for the surface impedances $\bar{\bar{Z}}_1$ and $\bar{\bar{Z}}_2$ are synthesized by using parameter space of the single-layer slot MNMs given in Fig. 4.13. Thus, a rotation angle θ and a phase shift of the unidirectional component φ_{is} are determined for each layers of the double-layered slot MNM. This method could easily be generalized to cascading of N layer single slot MNMs.

4.5.1 Design Example : Controlling the Gyrotropy and Non-reciprocity by Using double-layer Slot MNM Structures

The potential and the possibility of controlling the gyrotropy and non-reciprocity by using multi-layer slot MNM structure is highlighted in the previous section. Here, the design example which transform the y-polarized normally propagating plane waves into the x-polarized one in the transmission direction and reflect the x-polarized normally propagating plane waves with large non-reciprocal response is given. Thus, the desired transmission dyadic of the system is given as

$$\bar{\bar{R}}^{21}_d = \begin{bmatrix} 1 & 0 \\ 0 & 0 \end{bmatrix} \quad \bar{\bar{T}}^{21}_d = \begin{bmatrix} 0 & 1 \\ 0 & 0 \end{bmatrix}. \tag{4.14}$$

The desired transmission and reflection dyadics $\bar{\bar{R}}^{12}_d$ and $\bar{\bar{T}}^{12}_d$ when the structure is illuminated from the second region is not set, since this example shows the proof of the concept. For this design, two imperfectly matched single-layer slot MNMs with the design parameters given in Table 4.1 are used where the unit cells are rotated with unknown angles θ_1, θ_2 and the annular slotted rings are loaded with unidirectional components which have unknown phase shifts $\varphi^{(1)}_{is}$, $\varphi^{(2)}_{is}$ as illustrated in Fig. 4.14. Moreover, the constraint $d > 25\,\text{mm}$ is employed in the design due to the validity of the network model[6] and the lower and upper bounds

6. Below this distance higher order Floquet modes are not negligible.

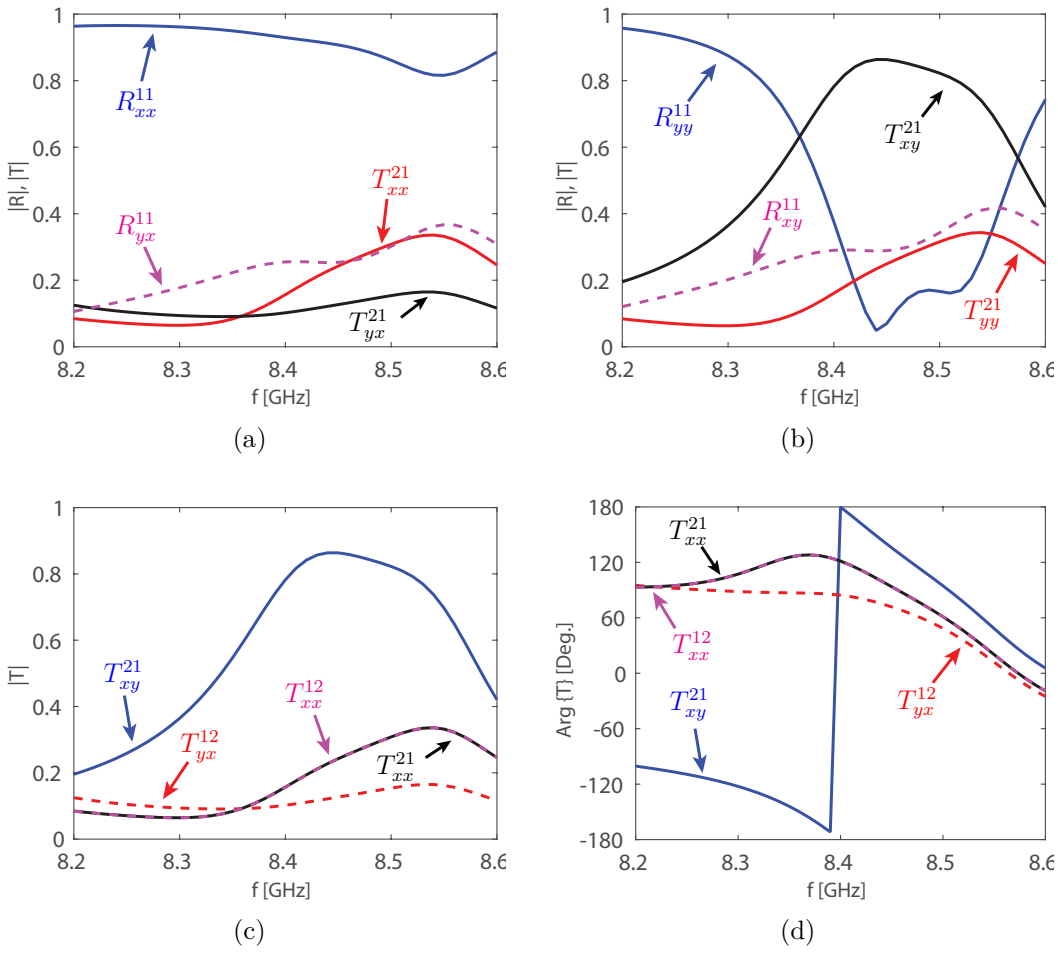

Figure 4.15 (a) Reflection and transmission coefficients of the designed double-layer slot MNM under plane wave incidence from $z > 0$: (a) x-polarized plane wave incidence. (b) y-polarized plane wave incidence. Non-reciprocity of the double-layer slot MNM : Comparison of the transmission coefficients when it is excited from $z > 0$ and $z < 0$ in time-reversal schema. (c) Magnitude. (d) Phase.

of the realizable surface impedances for imperfectly matched single-layer slot MNMs are defined from Fig. 4.13. In order to achieve a large non-reciprocal response, the constraints, $|T_{xy}^{21} - T_{yx}^{12}| > 0.5$ and $|R_{xy}^{21} - R_{yx}^{12}| > 0.5$ are defined. If these constraints are satisfied, the non-reciprocity in the amplitude of the transmission and reflection coefficients is achieved. Thus, the cost function is defined as

$$\text{Cost Func.} = |T_{xx}^{21} - T_{d_{xx}}^{21}|^2 + |T_{xy}^{21} - T_{d_{xy}}^{21}|^2 + |T_{yx}^{21} - T_{d_{yx}}^{21}|^2 + |T_{yy}^{21} - T_{d_{yy}}^{21}|^2. \tag{4.15}$$

The *Global Optimization Toolbox* of *MATLAB* is used to solve the constraint non-linear optimization problem. After feeding the optimization algorithm with three to five random

starting point sets, the solution converges to a global optimum point where the surface impedance of the single-layer slot MNMs are determined to achieve the design goals. Lastly, by using Fig. 4.13, the single-layer slot MNMs are synthesized from the required surface impedance values at 8.42 GHz as $\theta_1 = -110°$, $\varphi_{is}^{(1)} = 146°$ and $\theta_1 = -160°$, $\varphi_{is}^{(1)} = 146°$, and $d = 56.57$ mm. Reflection and transmission coefficient of the double-layer slot MNM with the synthesized parameters are calculated by using the network model (4.7) and plotted in Fig. 4.15(a) and 4.15(b). It is obvious that the design goal is achieved where the y-polarized normally incident plane waves are transformed into the x-polarized one and the x-polarized incident waves are reflected back. The residual values at the reflection and transmission coefficients of the structure could be attributed to the inherent loss of the single-layer slot MNM structure. Moreover, in Fig. 4.15(c) and 4.15(d), magnitude and phase of the co- and cross-polarized transmission coefficients are plotted to highlight the non-reciprocity of the structure. It can be clearly seen that there is a huge difference in amplitude of the cross-polarized transmission coefficients in a large frequency range. Moreover, there is a phase difference between the aforementioned cross-polarized transmission coefficients at 8.42 GHz. This result proves that the constraints defined to control the non-reciprocity are satisfied and large non-reciprocal response in amplitude of transmission coefficients is achieved. It is important to note that this design is realized by using single-layer slot MNMs which does not have a subtle non-reciprocal response in amplitude of the cross-polarized components. Thus, a 2D periodic device is designed to transform the y-polarized normally propagating incident waves to x-polarized ones when reflecting the x-polarized normally propagating waves with a huge non-reciprocal response.

In sum, a tentative analysis for transparency enhancement of slot MNMs is studied. Although the perfectly matched single-layer slot MNMs are transparent and have a ferrite-like non-reciprocal response, they are not suitable to be used in the Farby-Pérot cavity design for transparency enhancement of MNMs. The imperfectly matched single-layer slot MNMs could be employed to design a non-reciprocal gyrotropic Farby-Pérot cavities with minimal reflections due to less inherent loss of the structure. However, due to the trade-off between the non-reciprocal gyrotropic response and loss level of the structure, the double-layer slot MNMs made up from imperfectly matched single-layer slot MNMs have a weak non-reciprocal gyrotropic response. This issue could be solved by employing single-layer slot MNMs with different non-reciprocal gyrotropic responses so that the cascaded structure can be designed to achieve a certain non-reciprocal gyrotropic response. It is important to note that the structure introduced in this chapter for designing of highly transparent slot MNMs can only be used under normally propagating plane wave incidence. Moreover, thickness of the introduced double-layer structures are comparable to the wavelength of the operation because

the introduced network model is only valid for the zeroth order Floquet modes. Lastly, due to the limited bandwidth of the designed structure, experimental verification could not be employed.

CHAPTER 5 CONCLUSION

As a part of this research, a transparent slot MNM structure is presented. An annular slotted ring structure is employed to design a unit-cell of slot MNM. The big slot termination is introduced in the design process due to matching of the annular slotted transmission line and the unidirectional component. A slot MNM structure is realized by loading the annular slotted ring with a matched unidirectional component. Moreover, the gyrotropic resonance of the structure is shown from the reflection and the transmission dyadic of the structure. Magnetized ferrite-like non-reciprocal response of the structure is provided from the cross-polarized components of the transmission dyadic. Although the magnetized ferrite-like non-reciprocal response is realized, due to the longitudinal nature of the magnetic field lines over slot region, the neighboring unit-cells are destroying the travelling wave resonance of the structure. Thus, the effect of neighboring unit-cells results in a small quality factor. Moreover, it is shown that the slot MNM act as a either RCP or LCP wave polarizer depending on the isolation of the right- or left-handed eigenstates. This prevents the ellipticity of the structure from being zero so that the transmitted and reflected fields are elliptically polarized waves. As opposed to magnetized ferrites, the designed slot MNM has asymmetric response under x- and y-polarized normally propagating plane wave incidence so that the main diagonal of the susceptibility tensor of the slot MNM has different amplitudes. A symmetrical non-reciprocal response under x- and y-polarized normally propagating plane wave incidence is provided by rotating the unit-cell of the slot MNM by 45°. However, due to the reciprocal response of the co-polarized reflection and transmission coefficients, the magnetized ferrite-like non-reciprocity is desteroyed. In addition, it is clearly shown from the computed reflection dyadics of the slot MNM that the structure has a non-negligible reflectance which is unwanted for industrial applications.

It is shown that the non-reciprocity of slot MNMs is achieved by absorbing the one of counter-propagating eigenstates of the structure, namely right and left-handed states. The Sturm-Liouville theory is employed to explain the physical basis of the non-reciprocity. The coupling of the incident wave into the eigenstates is considered and magnetic dipole moment of the structure is calculated by setting one of the eigenstate coupling coefficient to zero based on the direction of the isolation. Thus, the susceptibility of the structure is derived based on the coupling coefficients where the gyrotropic response and magnetized ferrite-like non-reciprocal response is evident from the reciprocity theorem.

The characterization of slot MNMs based on its bianisotropic surface parameters is done for understanding electromagnetic response of the structure. The electromagnetic boundary

conditions are employed to derive analytical formulas for the bianisotropic surface parameters. Since the slot MNM has a strong surface impedance parameters, rest of the surface parameters are neglected and a transmission-line model of a slot MNM is proposed for the modeling purposes.

An important part of this research is to design reflection-less transparent slot MNMs. First, the duality theorem is used to cancel reflection of the slot MNMs since the structure is characterized with a rotating magnetic dipole moment. The requirement of rotating electric dipole moment makes the realization of such a dual particle very difficult due to the non-existence of a unidirectional components for magnetic currents. Thus, a well-known Farby-Pérot resonances are employed to cancel the reflection of transparent slot MNMs. A Farby-Pérot cavity is formed by stacking annular pair slots loaded with semiconductor-based unidirectional components sandwiching a dielectric slab spacer. The zeros of the reflection dyadics is solved for spacer thickness so that the reflection cancellation for each term of the reflection dyadic is theoretically achieved. An example which includes annular slotted rings loaded with perfectly matched unidirectional components is given. It is shown that the reflection cancellation could not be achieved for this design since the calculated spacer thickness is imaginary so that the loss in the design is evident. The inherent loss of the structure is explained from the annihilation of an eigenstate of the structure required for the non-reciprocity. Thus, the trade-off between the transparency of the structure and the non-reciprocal gyrotropic response is emphasized. In order to support this assertion, a double layer slot MNM design which includes annular slotted rings loaded with imperfectly matched unidirectional components is given. It is shown that the reflection minimization could be achieved with double-layer slot MNM in the expense of weak non-reciprocal gyrotropic response.

In order to circumvent the issue regarding the weak non-reciprocal response of highly transparent Farby-Pérot cavity, a design method for double-layer slot MNMs is introduced to control non-reciprocal and gyrotropic response of the structure by changing the phase shift of the unidirectional components and the rotation of the unit-cell.

An important contribution of this research is to design a transparent slot MNMs and identify the reason of its weak travelling wave resonance. In addition, determination of the trade-off between transparency and non-reciprocity levels of the multi-layer slot MNM structure constitutes another important contribution of this research. Lastly, a new design method is introduced to exploit the wide range of non-reciprocal responses provided by single-layer slot MNMs. Thus, a transparent slot MNM design is possible, however the effect of neighboring cells are destroying gyrotropic resonance of the structure. In addition, Farby-Pérot resonances could not be well utilized to achieve a highly transparent magnetized ferrite-like non-reciprocal response. However, apart from the magnetized ferrite-like non-reciprocal res-

ponse, a general non-reciprocal behaviour could be realized by using Farby-Pérot cavities formed by single-layer slot MNMs with different parameters.

In terms of future work several questions are still open regarding an effective design of a single-layer transparent MNM where the effect of the neighboring unit-cells is reduced. In addition, the analyzed reflection cancellation method in this thesis is based on the far-field interactions of the single-layer slot MNMs. However the near field interactions, namely Fano resonances, may result in a more effective and realizable reflection cancellation method for transparent slot MNMs. In addition, Fano resonances could overcome the trade-off between transparency and non-reciprocal response of the slot MNMs. Moreover, the design method given in this thesis is only valid under normally propagating plane wave incidence. Thus, the non-reciprocal response of single-layer slot MNMs under obliquely incident plane wave could be interesting for real-life industrial applications. Lastly, the newly introduced design method based on parameter manipulation of the single-layer slot MNMs could be utilized to achieve wide range of non-reciprocal responses by using different resonator shapes such as slotted ellipses or rectangles. These wide range of non-reciprocal responses could be used to design efficient and novel non-reciprocal components. Thus, a tentative analysis for the highly transparent slot MNMs are employed in this thesis and there are a lot of open questions in this area for the industrial applications of transparent MNMs.

REFERENCES

[1] C. Caloz and D. Sounas, "Field theory of electromagnetic metamaterials and beyond," in *IEEE MTT–S Int. Microw. Symp. (IMS)*, 2012, pp. 1–3.

[2] C. Caloz, T. Kodera, and D. Sounas, "Semiconductor-based non-reciprocal gyrotropic metamaterials requiring no external magnetic field," in *Advanced Electromagnetic Materials in Microwaves and Optics (METAMATERIALS), 2013 7th International Congress on*, Sept 2013, pp. 43–45.

[3] D. M. Pozar, *Microwave engineering.* John Wiley & Sons, 2009.

[4] Y. Zongfu and F. Shanhui, "Complete optical isolation created by indirect interband photonic transitions," *Nature Photon.*, vol. 3, pp. 91–94, Jan 2009.

[5] D. L. Sounas, T. Kodera, and C. Caloz, "Electromagnetic modeling of a magnetless nonreciprocal gyrotropic metasurface," *IEEE Trans. Antennas. Propag.*, vol. 61, pp. 221–231, 2013.

[6] D. L. Sounas, C. Caloz, and A. Alù, "Giant non-reciprocity at the subwavelength scale using angular momentum-biased metamaterials." *Nat. Commun.*, vol. 4, p. 2407, May 2013.

[7] D. L. Sounas, T. Kodera, and C. Caloz, "Electromagnetic modeling of a magnet-less non-reciprocal gyrotropic metasurface," *IEEE Trans. Antennas. Propag.*, vol. 61, no. 1, pp. 221–231, Jan. 2013.

[8] T. Kodera, D. L. Sounas, and C. Caloz, "Artificial faraday rotation using a ring metamaterial structure without static magnetic field," *Appl. Phys. Lett.*, vol. 99, pp. 031 114 :1–3, July 2011.

[9] T. Kodera, D. L. Sounas, and C. Caloz, "Magnet-less non-reciprocal metamaterials with magnetic or electric gyrotropy," *URSI Int. Symp. on Electromagnetic Theory (EMTS)*, pp. 397–400, May 2013.

[10] J. Teyssier, S. V. Saenko, D. Van Der Marel, and M. C. Milinkovitch, "Photonic crystals cause active colour change in chameleons," *Nat. Commun.*, vol. 6, 2015.

[11] J. C. Bose *et al.*, "Collected physical papers," 1927.

[12] W. E. Kock, "Metal-lens antennas," *Proceedings of the IRE*, vol. 34, no. 11, pp. 828–836, Nov 1946.

[13] R. E. Collin, *Field theory of guided waves.* Wiley-IEEE Press, 1991.

[14] D. R. Smith, , W. J. Padilla, W. J. Padilla, D. C. Vier, D. C. Vier, S. C. Nemat-Nasser, S. C. Nemat-Nasser, S. Schultz, and S. Schultz, "Composite Medium with Simultaneously Negative Permeability and Permittivity," *Phys. Rev. Lett.*, vol. 84, pp. 4184–4187, 2000.

[15] V. G. Veselago, "The electrodynamics of substances with simultaneously negative values of ε and μ," *Physics-Uspekhi*, vol. 10, no. 4, pp. 509–514, 1968.

[16] J. Pendry, A. Holden, D. Robbins, and W. Stewart, "Low frequency plasmons in thin-wire structures," *J. Phys. Condens. Matter*, vol. 10, no. 22, p. 4785, 1998.

[17] J. B. Pendry, A. J. Holden, D. J. Robbins, and W. J. Stewart, "Magnetism from conductors and enhanced nonlinear phenomena," *IEEE Trans. Microw. Theory Tech.*, vol. 47, no. 11, pp. 2075–2084, 1999.

[18] D. R. Smith and J. B. Pendry, "Homogenization of metamaterials by field averaging," *J. Opt. Soc. Am.*, vol. 23, no. 3, pp. 391–403, 2006.

[19] S. Tretyakov, *Analytical modeling in applied electromagnetics.* Norwood, MA : Artech House, Inc., 2003.

[20] C. Caloz and T. Itoh, *Electromagnetic metamaterials, Transmission line theory and microwave applications.* John Wiley & Sons, Inc., 2005.

[21] V. M. Shalaev, W. Cai, U. K. Chettiar, H.-K. Yuan, A. K. Sarychev, V. P. Drachev, and A. V. Kildishev, "Negative index of refraction in optical metamaterials," *Opt. Lett.*, vol. 30, no. 24, pp. 3356–3358, 2005.

[22] A. Alú and N. Engheta, "Pairing an epsilon-negative slab with a mu-negative slab : resonance, tunneling and transparency," *IEEE Trans. Antennas. Propag.*, vol. 51, no. 10, pp. 2558–2571, Oct 2003.

[23] L. Liu, C. Caloz, and T. Itoh, "Dominant mode leaky-wave antenna with backfire-to-endfire scanning capability," *Electron. Lett.*, vol. 38, no. 23, pp. 1414–1416, 2002.

[24] A. Alù and N. Engheta, "Achieving transparency with plasmonic and metamaterial coatings," *Phys Rev E Stat Nonlin Soft Matter Phys*, vol. 72, no. 1, pp. 1–9, 2005.

[25] D. Schurig, J. J. Mock, B. J. Justice, S. A. Cummer, J. B. Pendry, a. F. Starr, and D. R. Smith, "Metamaterial electromagnetic cloak at microwave frequencies." *Science*, vol. 314, no. 2006, pp. 977–980, 2006.

[26] B. Wang, J. Zhou, T. Koschny, M. Kafesaki, and C. M. Soukoulis, "Chiral metamaterials : simulations and experiments," *J. Opt.*, vol. 11, no. 11, p. 114003, 2009.

[27] A. Poddubny, I. Iorsh, P. Belov, and Y. Kivshar, "Hyperbolic metamaterials," *Nature Photon.*, vol. 7, no. 12, pp. 948–957, 2013.

[28] I. I. Smolyaninov, Y.-J. Hung, and C. C. Davis, "Magnifying superlens in the visible frequency range," *Science*, vol. 315, no. 5819, pp. 1699–1701, 2007.

[29] C. Holloway, M. Mohamed, E. F. Kuester, and A. Dienstfrey, "Reflection and transmission properties of a metafilm : with an application to a controllable surface composed of resonant particles," *IEEE Trans. Electromagn. Compat.*, vol. 47, no. 4, pp. 853–865, Nov 2005.

[30] S. Maci, G. Minatti, M. Casaletti, and M. Bosiljevac, "Metasurfing : Addressing waves on impenetrable metasurfaces," *IEEE Antenn. Wireless Propag. Lett.*, vol. 10, pp. 1499–1502, 2011.

[31] C. Holloway, E. F. Kuester, J. Gordon, J. O'Hara, J. Booth, and D. Smith, "An overview of the theory and applications of metasurfaces : The two-dimensional equivalents of metamaterials," *IEEE Trans. Antennas. Propag.*, vol. 54, no. 2, pp. 10–35, April 2012.

[32] N. Yu, P. Genevet, M. a. Kats, F. Aieta, J.-P. Tetienne, F. Capasso, and Z. Gaburro, "Light Propagation with Phase Discontinuities : Generalized Laws of Reflection and Refraction," *Science*, vol. 334, no. 2011, pp. 333–337, 2011.

[33] Y. Zhao, M. Belkin, and A. Alù, "Twisted optical metamaterials for planarized ultrathin broadband circular polarizers," *Nat. Commun.*, vol. 3, p. 870, 2012.

[34] A. P. Raman, M. A. Anoma, L. Zhu, E. Rephaeli, and S. Fan, "Passive radiative cooling below ambient air temperature under direct sunlight," *Nature*, vol. 515, no. 7528, pp. 540–544, 2014.

[35] J. Lee, M. Tymchenko, C. Argyropoulos, P.-Y. Chen, F. Lu, F. Demmerle, G. Boehm, M.-C. Amann, A. Alù, and M. A. Belkin, "Giant nonlinear response from plasmonic metasurfaces coupled to intersubband transitions," *Nature*, vol. 511, no. 7507, pp. 65–69, 2014.

[36] C. Pfeiffer and A. Grbic, "Bianisotropic Metasurfaces for Optimal Polarization Control : Analysis and Synthesis," *Phys. Rev. Appl.*, vol. 044011, pp. 1–11, 2014.

[37] Z. Yu and S. Fan, "Optical isolation based on nonreciprocal phase shift induced by interband photonic transitions," *Appl. Phys. Lett.*, vol. 94, no. 17, 2009.

[38] T. Kodera, D. L. Sounas, and C. Caloz, "Magnetless nonreciprocal metamaterial (MNM) technology : Application to microwave components," *IEEE Trans. Microw. Theory Tech.*, vol. 61, pp. 1030–1042, 2013.

[39] D. L. Sounas and A. Alù, "Angular-momentum-biased nanorings to realize magnetic-free integrated optical isolation," *ACS Photonics*, vol. 1, no. 3, pp. 198–204, 2014.

[40] N. A. Estep, D. L. Sounas, J. Soric, and A. Alù, "Magnetic-free non-reciprocity and isolation based on parametrically modulated coupled-resonator loops," *Nature Phys.*, vol. 10, no. December, pp. 923–927, 2014.

[41] R. Fleury, D. L. Sounas, C. F. Sieck, M. R. Haberman, and A. Alù, "Sound isolation and giant linear nonreciprocity in a compact acoustic circulator." *Science*, vol. 343, pp. 516–9, 2014.

[42] L. D. Landau and E. M. Lifshitz, *Electrodyamics of Continuous Media.* Pergamon Press, 1984.

[43] W. S. Weiglhofer and A. Lakhtakia, *Introduction to complex mediums for optics and electromagnetics.* SPIE press, 2003, vol. 123.

[44] D. L. Sounas and C. Caloz, "Gyrotropy and nonreciprocity of graphene for microwave applications," *IEEE Trans. Microw. Theory Tech.*, vol. 60, no. 4, pp. 901–914, 2012.

[45] J. A. Stratton, *Electromagnetic theory.* John Wiley & Sons, 2007, vol. 33.

[46] J. A. Kong, "Theorems of bianisotropic media," *Proc. IEEE*, vol. 60, no. 9, pp. 1036–1046, 1972.

[47] H. B. G. Casimir, "On onsager's principle of microscopic reversibility," *Rev. Mod. Phys.*, vol. 17, no. 2-3, p. 343, 1945.

[48] J. D. Jackson, *Classical Electrodynamics.* John Wiley & Sons, 1999.

[49] H. Lira, Z. Yu, S. Fan, and M. Lipson, "Electrically driven nonreciprocity induced by interband photonic transition on a silicon chip," *Phys. Rev. Lett.*, vol. 109, p. 033901, Jul 2012.

[50] T. Kodera, D. Sounas, H. V. Nguyen, H. Razavipour, and C. Caloz, "Field displacement in a traveling-wave ring resonator meta-structure," in *General Assembly and Scientific Symposium, 2011 XXXth URSI*, Aug 2011, pp. 1–4.

[51] T. Kodera, D. L. Sounas, and C. Caloz, "Nonreciprocal magnetless CRLH leaky-wave antenna based on a ring metamaterial structure," *IEEE Antenn. Wireless Propag. Lett.*, vol. 10, pp. 1551–1554, 2011.

[52] C. Caloz, A. Shahvarpour, D. Sounas, T. Kodera, B. Gurlek, and N. Chamanara, "Practical realization of perfect electromagnetic conductor (pemc) boundaries using ferrites, magnet-less non-reciprocal metamaterials (mnms) and graphene," in *URSI Int. Symp. on Electromagnetic Theory (EMTS)*, May 2013, pp. 652–655.

[53] I. Bahl and P. Bhartia, *Microwave Solid State Circuit Design*, 2nd ed. Wiley-Interscience, 2003.

[54] B. Lax and K. J. Button, *Microwave Ferrites and Ferrimagnetics*. New York : McGraw-Hill, 1962.

[55] A. Alù, "First-principles homogenization theory for periodic metamaterials," *Phys. Rev. B*, vol. 84, pp. 1–18, 2011.

[56] H. Suhl and L. R. Walker, "Topics in guided wave propagation through gyromagnetic media," *Bell Syst. Tech. J.*, vol. 33, no. 5, pp. 1133–1194, 1954.

[57] L. Dong, H. Jiang, H. Chen, and Y. Shi, "Tunnelling-based faraday rotation effect enhancement," *J. Phys. D : Appl. Phys.*, vol. 44, no. 14, p. 145402, 2011.

[58] M. Moccia, G. Castaldi, V. Galdi, A. Alu', and N. Engheta, "Enhanced Faraday Rotation via Resonant Tunnelling in Tri-Layers Containing Magneto-Optical Metals," *J. Phys. D : Appl. Phys.*, vol. 025002, p. 18, 2013.

[59] M. Kerker, D.-S. Wang, and C. L. Giles, "Electromagnetic scattering by magnetic spheres," *J. Opt. Soc. Am.*, vol. 73, no. 6, p. 765, 1983.

[60] C. Pfeiffer and A. Grbic, "Metamaterial Huygens' surfaces : Tailoring wave fronts with reflectionless sheets," *Phys. Rev. Lett.*, vol. 110, no. May, pp. 1–5, 2013.

[61] M. Kim, A. M. H. Wong, and G. V. Eleftheriades, "Optical huygens' metasurfaces with independent control of the magnitude and phase of the local reflection coefficients," *Phys. Rev. X*, vol. 4, p. 041042, Dec 2014.

[62] V. Asadchy, Y. Ra'di, J. Vehmas, and S. Tretyakov, "Functional Metamirrors Using Bianisotropic Elements," *Phys. Rev. Lett.*, vol. 114, no. 9, pp. 1–5, 2015.

[63] B. Gurlek, D. Sounas, and C. Caloz, "Enhancing the transparency of gyrotropic magnet-less non-reciprocal metamaterials (mnms) using slot pair particles," in *Electromagnetics in Advanced Applications (ICEAA), 2013 International Conference on*, Sept 2013, pp. 1481–1484.

[64] B. Gurlek and C. Caloz, "Towards reflection-less or total reflection magnet-less non-reciprocal metasurface," in *Antennas and Propagation (EuCAP), 2015 9th European Conference on*, April 2015.

APPENDIX A CALCULATION OF ELECTROMAGNETIC RESPONSE OF A UNIDIRECTIONAL COMPONENT LOADED ANNULAR SLOTTED RING BASED ON SIGNAL FLOW GRAPH TECHNIQUE

Electromagnetic response of a slot MNM cannot be computed by only using a full-wave numerical software due to the presence of unidirectional component. The unidirectional component is a circuit element that unilaterally transmits the current wave. Thus, a circuit simulation is required for the full-wave simulation of a slot MNM.

In this thesis, full-wave simulation results of the annular slotted ring structure is calculated by using HFSS and this results is fed to a MATLAB based in-house circuit simulator to calculate reflection and transmission coefficients of the slot MNM. Full-wave simulation result of the annular slotted ring structure can be represented with a 6×6 S matrix where 4 ports characterizes TM^z and TE^z plane wave propagation and the remaining 2 ports characterize lumped ports. The lumped ports are used to connect the unidirectional component. The circuit simulator is implemented by using the circuit representation of the Slot MNM where 6×6 S matrix of the annular slotted ring structure under normally incident TM^z and TE^z plane waves is loaded with 2×2 S matrix of the isolator as shown in Fig. A.1. The

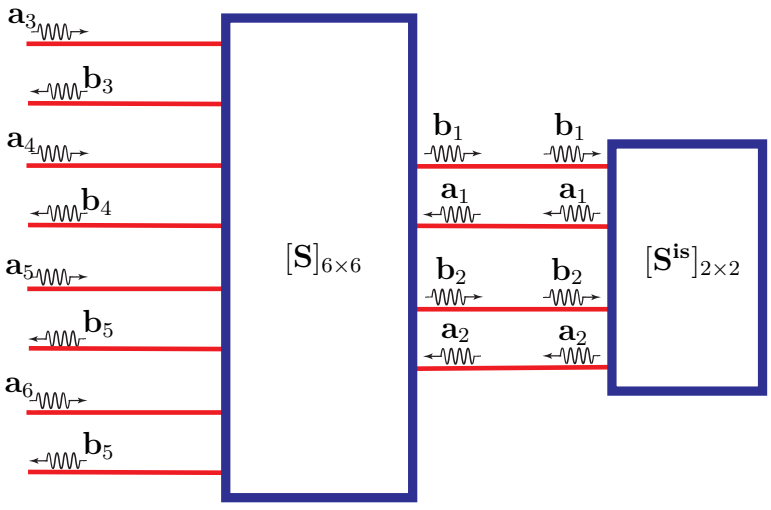

Figure A.1 Circuit representation of the slot MNM where full-wave solution of the annular slotted ring structure is loaded with an unidirectional component through S-parameters. $\mathbf{a}$ and $\mathbf{b}$ are incident and reflected power waves from the structure under TM^z and TE^z illuminations. $[\mathbf{S}]_{6\times6}$ is the S matrix of the annular slotted ring and $[\mathbf{S^{is}}]_{2\times2}$ S matrix of the isolator.

loading of the annular slotted ring structure with an isolator could be done by using network flow graph technique as outline in [3] as

$$\begin{bmatrix} b_3 \\ b_4 \\ b_5 \\ b_6 \end{bmatrix} = \begin{bmatrix} S_{31} & S_{32} \\ S_{41} & S_{42} \\ S_{51} & S_{52} \\ S_{61} & S_{62} \end{bmatrix} [S_{is}]_{2\times 2} \left(\bar{\bar{I}} - \begin{bmatrix} S_{11} & S_{12} \\ S_{21} & S_{22} \end{bmatrix} [S_{is}]_{2\times 2} \right)^{-1} \begin{bmatrix} S_{13} & S_{14} & S_{15} & S_{16} \\ S_{23} & S_{24} & S_{25} & S_{26} \end{bmatrix} \begin{bmatrix} a_3 \\ a_4 \\ a_5 \\ a_6 \end{bmatrix}, \quad \text{(A.1)}$$

where $\bar{\bar{I}}$ is the unit tensor, $[\mathbf{S_{is}}]$ is the S-parameters of the unidirectional component, **a** and **b** are incident and reflected power waves from the structure for TM^z and TE^z polarizations, respectively. **a** and **b** are 2×1 vector which includes x- and y-polarized incoming and outgoing power waves. Thus, reflection and transmission coefficients of the slot MNM, b_3 , b_4 , b_5 and b_6 , could be computed by using full-wave simulation results of the annular slotted ring structure and the circuit simulator. Note that reflection and transmission dyadic of the slot MNM can also be calculated by using a commercial circuit simulator such as ADS or Ansoft Designer.

APPENDIX B IMPLEMENTATION OF A COMMON-SOURCE FET AS A UNIDIRECTIONAL COMPONENT IN SLOT MNM DESIGN

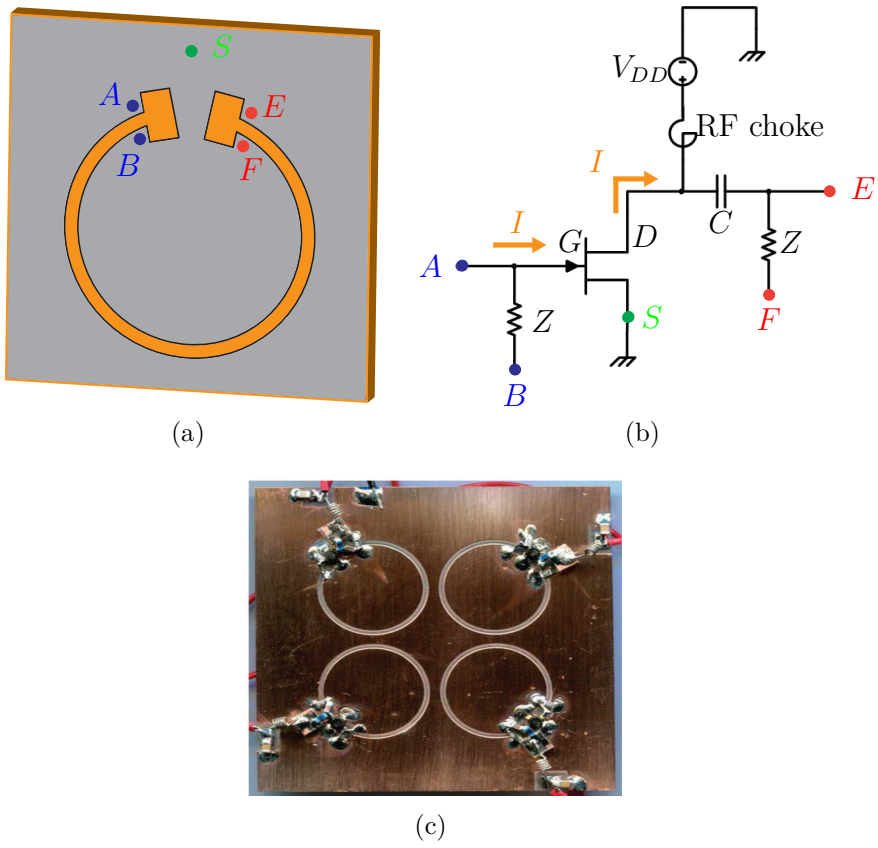

Figure B.1 (a) Slot MNM design with FET connection points.(b) Common-source FET implementation as an unidirectional component of a slot MNM. (c) Fabricated structure by Toshiro et al. [9]

Implementation of slot MNMs could be done by loading the annular slotted ring structure with a common-source FET since common-source FET could be used as a unidirectional component so that the current flowing is blocked form drain to gate. A slot MNM is fabricated and experimented by Toshiro et al. [9] as shown in Fig. B.1(c). The implementation is schematically shown in Fig. B.1(a) and B.1(b). In Fig. B.1(a), the points A and E represents the parts of transmission-line where the current flows and the points B and F represents the grounds for the points A and E, respectively. The points S represents the global ground for the whole structure. Thus, FET is biased with a DC voltage source and excited by the voltage

difference between points A and B, and E and F. In addition, Z represents impedances of the lumped ports in Fig. 3.2(c) and determined for matching of the annular slotted ring and the FET. In general, The matching impedances in Fig. B.1(b) are different since the input and output impedances of FET are not same. Moreover, The RF choke is used to prevent RF current leaking in to DC voltage source and the bypass capacitor are used to prevent DC current leakage to the annular slotted ring.

APPENDIX C REFLECTION DYADIC OF THE DOUBLE-LAYER SLOT MNMs

Reflection dyadic of the double-layer slot MNM in terms of surface impedance dyadic $\bar{\bar{Z}}$ of a single-layer slot MNM given in (4.9) can be derived by using the $ABCD$ matrix of the structure (4.7) with $ABCD$ matrix to S matrix conversation formulas (4.8). $ABCD$ matrix of the double layer slot MNM (4.7) is analytically derived and it is converted to corresponding S-parameters by using Mathematica. The co-polarized coefficients under x-polarized plane wave incidence are derived as

$$\begin{aligned}
G_{xx} = &-Z^a_{xx}Z^a_{yy}\eta_d^2 + Z^a_{yx}Z^a_{xy}\eta_d^2 - Z^a_{xx}Z^b_{yy}\eta_d^2 + Z^a_{xy}Z^b_{yx}\eta_d^2 + Z^a_{yx}Z^b_{xy}\eta_d^2 \\
&- Z^a_{yy}Z^b_{xx}\eta_d^2 - Z^b_{xx}Z^b_{yy}\eta_d^2 + Z^b_{xy}Z^b_{yx}\eta_d^2 - 2Z^a_{xx}\eta_d^2\eta_0 - 2Z^b_{xx}\eta_d^2\eta_0 \qquad \text{(C.1)} \\
H_{xx} = &-Z^a_{xx}\eta_d^3 - Z^a_{yy}\eta_d^3 - Z^b_{xx}\eta_d^3 - Z^b_{yy}\eta^3 - 3Z^a_{xx}\eta_d\eta_0^2 - Z^a_{xx}Z^a_{yy}Z^b_{xx}\eta_d \\
&+ Z^a_{xy}Z^a_{yx}Z^b_{xx}\eta_d - Z^a_{xx}Z^a_{yy}Z^b_{yy}\eta_d + Z^a_{xy}Z^a_{yx}Z^b_{yy}\eta_d - Z^a_{xx}Z^b_{xx}Z^b_{yy}\eta_d \\
&+ Z^a_{xx}Z^b_{xy}Z^b_{yx}\eta_d - Z^a_{yy}Z^b_{xx}Z^b_{yy}\eta_d + Z^a_{yy}Z^b_{xy}Z^b_{yx}\eta_d - 2Z^a_{xx}Z^a_{yy}\eta_d\eta_0 \\
&+ 2Z^a_{xy}Z^a_{yx}\eta_d\eta_0 - 2Z^a_{xx}Z^b_{xx}\eta_d\eta_0 - 2Z^a_{xx}Z^b_{yy}\eta_d\eta_0 + 2\eta_d\eta_0^3 - 2\eta_d^3\eta_0 \\
&+ Z^a_{yy}\eta_d\eta_0^2 + Z^b_{xx}\eta_d\eta_0^2 + Z^b_{yy}\eta_d\eta_0^2, \qquad \text{(C.2)} \\
K_{xx} = &\,\eta_d^4 - \eta_0^4 + Z^a_{xx}\eta_0^3 - Z^a_{yy}\eta_0^3 - Z^b_{xx}\eta_0^3 - Z^b_{yy}\eta_0^3 + Z^a_{xx}Z^a_{yy}\eta_0^2 \\
&- Z^a_{xy}Z^a_{yx}\eta_0^2 + Z^a_{xx}Z^b_{xx}\eta_d^2 + Z^a_{xy}Z^b_{yx}\eta_d^2 + Z^a_{yx}Z^b_{xy}\eta_d^2 + Z^a_{yy}Z^b_{yy}\eta_d^2 \\
&+ Z^a_{xx}Z^b_{xx}\eta_0^2 + Z^a_{xx}Z^b_{yy}\eta_0^2 - Z^a_{yy}Z^b_{yy}\eta_0^2 - Z^a_{yy}Z^b_{yy}\eta_0^2 - Z^b_{xx}Z^b_{yy}\eta_0^2 \\
&+ Z^b_{xy}Z^a_{yx}\eta_0^2 + Z^a_{xx}\eta_d^2\eta_0 + Z^a_{yy}\eta_d^2\eta_0 - Z^b_{xx}\eta_d^2\eta_0 + Z^b_{yy}\eta_d^2\eta_0 \\
&+ Z^a_{xx}Z^a_{yy}Z^b_{xx}Z^b_{yy} - Z^a_{xx}Z^a_{yy}Z^b_{xy}Z^b_{yx} - Z^a_{xy}Z^a_{yx}Z^b_{xx}Z^b_{yy} + Z^a_{xy}Z^a_{yx}Z^b_{xy}Z^b_{yx} \\
&+ Z^a_{xx}Z^a_{yy}Z^b_{xx}\eta_0 - Z^a_{xy}Z^a_{yx}Z^b_{xx}\eta_0 + Z^a_{xx}Z^a_{yy}Z^b_{yy}\eta_0 - Z^a_{xy}Z^a_{yx}Z^b_{yy}\eta_0 \\
&+ Z^a_{xx}Z^b_{xx}Z^b_{yy}\eta_0 - Z^a_{xx}Z^b_{xy}Z^b_{yx}\eta_0 - Z^a_{yy}Z^b_{xx}Z^a_{yy}\eta_0 + Z^a_{yy}Z^b_{xy}Z^b_{yx}\eta_0, \qquad \text{(C.3)}
\end{aligned}$$

where $\bar{\bar{Z}}^a$ and $\bar{\bar{Z}}^b$ are surface impedance dyadic of the first and second single-layer slot MNMs, η_d is the characteristic impedance of dielectric spacer and η_0 is the characteristic impedance of air. In addition, the cross-polarized coefficients under x-polarized plane wave incidence are

derived as

$$G_{xy} = -2Z^a_{xy}\eta_d^2\eta_0 - 2 * Z^b_{xy}\eta_d^2\eta_0 \tag{C.4}$$
$$H_{xy} = -4Z^a_{xy}\eta_d\eta_0^2 - 2Z^a_{xy}Z^b_{xx}\eta_d\eta_0 - 2Z^a_{xy}Z^b_{yy}\eta_d\eta_0, \tag{C.5}$$
$$K_{xy} = 2Z^a_{xy}\eta_0^3 + 2Z^a_{xy}Z^b_{xx}\eta_0^2 + 2Z^a_{xy}Z^b_{yy}\eta_0^2 - 2Z^b_{xy}\eta_d^2\eta_0 \tag{C.6}$$
$$+ 2Z^a_{xy}Z^b_{xx}Z^b_{22}\eta_0 - 2Z^a_{xy}Z^b_{xy}Z^b_{yx}\eta_0. \tag{C.7}$$

The cross-polarized coefficients under y-polarized plane wave incidence are derived as

$$G_{yx} = -2Z^a_{yx}\eta_d^2\eta_0 - 2 * Z^b_{yx}\eta_d^2\eta_0 \tag{C.8}$$
$$H_{yx} = -4Z^a_{yx}\eta_d\eta_0^2 - 2Z^a_{yx}Z^b_{xx}\eta_d\eta_0 - 2Z^a_{yx}Z^b_{yy}\eta_d\eta_0, \tag{C.9}$$
$$K_{yx} = 2Z^a_{yx}\eta_0^3 + 2Z^a_{yx}Z^b_{xx}\eta_0^2 + 2Z^a_{yx}Z^b_{yy}\eta_0^2 - 2Z^b_{yx}\eta_d^2\eta_0$$
$$+ 2Z^a_{yx}Z^b_{xx}Z^b_{22}\eta_0 - 2Z^a_{yx}Z^b_{xy}Z^b_{yx}\eta_0. \tag{C.10}$$

Lastly, The co-polarized coefficients under y-polarized plane wave incidence are derived as

$$\begin{aligned} G_{yy} = &-Z^a_{xx}Zg^a_{yy}\eta_d^2 + Z^a_{yx}Z^a_{xy}\eta_d^2 - Z^a_{xx}Z^b_{yy}\eta_d^2 + Z^a_{xy}Z^b_{yx}\eta_d^2 \\ &+ Z^a_{yx}Z^b_{xy}\eta_d^2 - Z^a_{yy}Z^b_{xx}\eta_d^2 - Z^b_{xx}Z^b_{yy}\eta_d^2 + Z^b_{xy}Z^b_{yx}\eta_d^2 \\ &- 2Z^a_{xx}\eta_d^2\eta_0 - 2Z^b_{yy}\eta_d^2\eta_0, \end{aligned} \tag{C.11}$$

$$\begin{aligned} H_{yy} = &-Z^a_{xx}\eta_d^3 - Z^a_{yy}\eta_d^3 - Z^b_{xx}\eta_d^3 - Z^b_{yy}\eta^3 - 3Z^a_{xx}\eta_d\eta_0^2 \\ &- Z^a_{xx}Z^a_{yy}Z^b_{xx}\eta_d + Z^a_{xy}Z^a_{yx}Z^b_{xx}\eta_d - Z^a_{xx}Z^a_{yy}Z^b_{yy}\eta_d + Z^a_{xy}Z^a_{yx} \\ &Z^b_{yy}\eta_d - Z^a_{xx}Z^b_{xx}Z^b_{yy}\eta_d + Z^a_{xx}Z^b_{xy}Z^b_{yx}\eta_d - Z^a_{yy}Z^b_{xx}Z^b_{yy}\eta_d \\ &+ Z^a_{yy}Z^b_{xy}Z^b_{yx}\eta_d - 2Z^a_{xx}Z^a_{yy}\eta_d\eta_0 + 2Z^a_{xy}Z^a_{yx}\eta_d\eta_0 - 2Z^a_{yy}Z^b_{xx}\eta_d\eta_0 \\ &- 2Z^a_{yy}Z^b_{yy}\eta_d\eta_0 + 2\eta_d\eta_0^3 - 2\eta_d^3\eta_0 + Z^a_{xx}\eta_d\eta_0^2 + Z^b_{xx}\eta_d\eta_0^2 + Z^b_{yy}\eta_d\eta_0^2), \end{aligned} \tag{C.12}$$

$$\begin{aligned} K_{yy} = &\eta_d^4 - \eta_0^4 + Z^a_{xx}\eta_0^3 - Z^a_{yy}\eta_0^3 - Z^b_{xx}\eta_0^3 - Z^b_{yy}\eta_0^3 + Z^a_{xx}Z^a_{yy}\eta_0^2 - Z^a_{xy}Z^a_{yx}\eta_0^2 \\ &+ Z^a_{xx}Z^b_{xx}\eta_d^2 + Z^a_{xy}Z^b_{yx}\eta_d^2 + Z^a_{yx}Z^b_{xy}\eta_d^2 + Z^a_{yy}Z^b_{yy}\eta_d^2 + Z^a_{xx}Z^b_{xx}\eta_0^2 + Z^a_{xx}Z^b_{yy}\eta_0^2 \\ &+ Z^a_{yy}Z^b_{xx}\eta_0^2 + Z^a_{yy}Z^b_{yy}\eta_0^2 - Z^b_{xx}Z^b_{yy}\eta_0^2 + Z^b_{xy}Z^b_{yx}\eta_0^2 + Z^a_{xx}\eta_d^2\eta_0 + Z^a_{yy}\eta_d^2\eta_0 \\ &+ Z^b_{xx}\eta_d^2\eta_0 - Z^b_{yy}\eta_d^2\eta_0 + Z^a_{xx}Z^a_{yy}Z^b_{xx}Z^b_{yy} - Z^a_{xx}Z^a_{yy}Z^b_{xy}Z^b_{yx} - Z^a_{xy}Z^a_{yx}Z^b_{xx}Z^b_{yy} \\ &+ Z^a_{xy}Z^a_{yx}Z^b_{xy}Z^b_{yx} + Z^a_{xx}Z^a_{xx}Z^b_{yy}\eta_0 - Z^a_{xy}Z^a_{yx}Z^b_{xx}\eta_0 + Z^a_{xx}Z^a_{yy}Z^b_{yy}\eta_0 \\ &- Z^a_{xy}Z^a_{yx}Z^b_{yy}\eta_0 + Z^a_{xx}Z^b_{xx}Z^b_{yy}\eta_0 - Z^a_{xx}Z^b_{xy}Z^b_{yx}\eta_0 - Z^a_{yy}Z^b_{xx}Z^b_{yy}\eta_0 \\ &- Z^a_{yy}Z^b_{xy}Z^b_{yx}\eta_0. \end{aligned} \tag{C.13}$$

The coefficients found in the denominator of (4.9) are derived as

$$\begin{aligned}
D = &-4\eta_d^2\eta_0^2 - Z_{xx}^a Z_{yy}^a \eta_d^2 + Z_{xy}^a Z_{yx}^a \eta_d^2 - Z_{xx}^a Z_{yy}^b \eta_d^2 + Z_{xy}^a Z_{yx}^b \eta_d^2 \\
&+ Z_{yx}^a Z_{xy}^b \eta_d^2 - Z_{yy}^a Z_{xx}^b \eta_d^2 - Z_{xx}^b Z_{yy}^b \eta_d^2 + Z_{xy}^b Z_{yx}^b \eta^2 - 2Z_{xx}^a \eta_d^2 \eta_0 \\
&- 2Z_{xx}^b \eta_d^2 \eta_0 - 2Z_{yy}^a \eta_d^2 \eta_0 - 2Z_{yy}^b \eta_d^2 \eta_0, \qquad \text{(C.14)} \\
E = &-Z_{xx}^a \eta_d^3 - Z_{yy}^a \eta_d^3 - Z_{xx}^b \eta_d^3 - Z_{yy}^b \eta_d^3 - 4\eta_d \eta_0^3 - 4\eta_d^3 \eta_0 - 3Z_{xx}^a \eta_d \eta_0^2 \\
&- 3Z_{yy}^a \eta_d \eta_0^2 - 3Z_{xx}^b \eta_d \eta_0^2 - 3Z_{yy}^b \eta_d \eta_0^2 - Z_{xx}^a Z_{yy}^a Z_{xx}^b \eta_d + Z_{xy}^a Z_{yx}^a Z_{xx}^b \eta_d \\
&- Z_{xx}^a Z_{yy}^a Z_{yy}^a \eta_d + Z_{xy}^a Z_{yx}^a Z_{yy}^b \eta_d - Z_{xx}^a Z_{xx}^b Z_{yy}^b \eta_d + Z_{xx}^a Z_{xy}^b Z_{yx}^b \eta_d - Z_{yy}^a Z_{xx}^b Z_{yy}^b \eta_d \\
&+ Z_{yy}^a Z_{xy}^b Z_{yx}^b \eta_d - 2Z_{xx}^a Z_{yy}^a \eta_d \eta_0 + 2Z_{xy}^a Z_{yx}^a \eta_d \eta_0 - 2Z_{xx}^a Z_{xx}^b \eta_d \eta_0 \\
&- 2Z_{xx}^a Z_{yy}^b \eta_d \eta_0 - 2Z_{yy}^a Z_{xx}^b \eta_d \eta_0 - 2Z_{yy}^a Z_{yy}^b \eta_d \eta_0 - 2Z_{xx}^b Z_{yy}^b \eta_d \eta_0 + 2Z_{xy}^a Z_{yx}^b \eta_d \eta_0, \qquad \text{(C.15)} \\
F = &\eta_d^4 + \eta_0^4 + Z_{xx}^a \eta_0^3 + Z_{yy}^a \eta_0^3 + Z_{xx}^b \eta_0^3 + Z_{yy}^a \eta_0^3 + 2eta_d^2 \eta_0^2 + Z_{xx}^a Z_{yy}^a \eta_0^2 - Z_{xy}^a Z_{yx}^a \eta_0^2 \\
&+ Z_{xx}^a Z_{xx}^b \eta_d^2 + Z_{xy}^a Z_{yx}^b \eta_d^2 + Z_{yx}^a Z_{xy}^b \eta_d^2 + Z_{yy}^a Z_{yy}^b \eta_d^2 + Z_{xx}^a Z_{xx}^b \eta_0^2 + Z_{xx}^a Z_{yy}^b \eta_0^2 \\
&+ Z_{yy}^a Z_{xx}^b \eta_0^2 + Z_{yy}^a Z_{yy}^b \eta_0^2 + Z_{xx}^b Z_{yy}^b \eta_0^2 - Z_{xy}^b Z_{yx}^b \eta_0^2 + Z_{xx}^a \eta_d^2 \eta_0 + Z_{yy}^a \eta_d^2 \eta_0 \\
&+ Z_{xx}^b \eta^2 \eta_0 + Z_{yy}^b \eta_d^2 \eta_0 + Z_{xx}^a Z_{yy}^a Z_{xx}^b Z_{yy}^b - Z_{xx}^a Z_{yy}^a Z_{xy}^b Z_{yx}^b - Z_{xy}^a Z_{yx}^a Z_{xx}^b Z_{yy}^b \\
&+ Z_{xy}^a Z_{yx}^a Z_{xy}^b Z_{yx}^b + Z_{xx}^a Z_{yy}^a Z_{xx}^b \eta_0 - Z_{xy}^a Z_{yx}^a Z_{xx}^b \eta_0 + Z_{xx}^a Z_{yy}^a Z_{yy}^b \eta_0 \\
&- Z_{xy}^a Z_{yx}^a Z_{yy}^b \eta_0 + Z_{xx}^a Z_{xx}^b Z_{yy}^b \eta_0 - Z_{xx}^a Z_{xy}^b Z_{yx}^b \eta_0 + Z_{yy}^a Z_{xx}^b Z_{yy}^b \eta_0 \\
&- Z_{yy}^a Z_{xy}^b Z_{yx}^b \eta_0. \qquad \text{(C.16)}
\end{aligned}$$